Title
Chip-Scale Architectures for Precise Optical Frequency Synthesis

Author
Yang, Jinghui

Publication Date
2017

UNIVERSITY OF CALIFORNIA

Los Angeles

Chip-Scale Architectures for Precise Optical Frequency Synthesis

A dissertation submitted in partial satisfaction of the
requirements for the degree Doctor of Philosophy
in Electrical and Computer Engineering

by

Jinghui Yang

2018

ABSTRACT OF THE DISSERTATION

Chip-Scale Architectures for Precise Optical Frequency Synthesis

by

Jinghui Yang

Doctor of Philosophy in Electrical and Computer Engineering

University of California, Los Angeles, 2018

Professor Chee Wei Wong, Chair

Scientists and engineers have investigated various types of stable and accurate optical synthesizers, where mode-locked laser based optical frequency comb synthesizers have been widely investigated. These frequency combs bridge the frequencies from optical domain to microwave domain with orders of magnitude difference, providing a metrological tool for various platforms. The demand for highly robust, scalable, compact and cost-effective femtosecond-laser synthesizers, however, are of great importance for applications in air- or space-borne platforms, where low cost and rugged packaging are particularly required. This has been afforded in the past several years due to breakthroughs in chip-scale nanofabrication, bringing advances in optical frequency combs down to semiconductor chips. These platforms, with significantly enhanced light-matter interaction, provide a fertile sandbox for research rich in nonlinear dynamics, and offer a reliable route towards low-phase noise photonic oscillators, broadband optical frequency synthesizers, miniaturized optical clockwork, and coherent terabit communications.

The dissertation explores various types of optical frequency comb synthesizers based on nonlinear microresonators. Firstly, the fundamental mechanism of mode-locking in a high-quality factor microresonator is examined, supported by ultrafast optical characterizations, analytical closed-form solutions and numerical modeling. In the evolution of these frequency microcombs, the key nonlinear dynamical effect governing the comb state coherence is rigorously analyzed. Secondly, a prototype of chip-scale optical frequency synthesizer is demonstrated, with the laser frequency comb stabilized down to instrument-limited 50-mHz RF frequency inaccuracies and 10^{-16} fractional frequency inaccuracies, near the fundamental limits. Thirdly, a globally stable Turing pattern is achieved and characterized in these nonlinear resonators with high-efficiency conversion, subsequently generating coherent high-power terahertz radiation via plasmonic photomixers. Finally, a new universal modality of frequency combs is discussed, including satellite states, dynamical tunability, and high efficiency conversion towards direct chip-scale optical frequency synthesis at the precision metrology frontiers.

The dissertation of Jinghui Yang is approved.

Tatsuo Itoh

Mona Jarrahi

Chandra J. Joshi

Károly Holczer

Chee Wei Wong, Committee Chair

University of California, Los Angeles

2018

Table of Contents

List of Figures

List of Tables

Acknowledgements

During years of my doctoral work, I have been fortunate to meet many talented individuals to guide, inspire and encourage me along the journey. I heartily appreciate the tremendous support, without which this work would not be possible. Thank you to all my mentors, colleagues and friends.

First and foremost, I would like to express my immense gratitude to my advisor Professor Chee Wei Wong, for his vision, leadership, guidance and support along the way. I deeply thank him for providing me the precious opportunities to join these enriching and intriguing topics, take challenges, along with his continuous encouragement since our first meeting at the lobby of the Mechanical Engineering Department at Columbia, and his convincing me to transfer to UCLA to embrace a different research environment (which I had never envisaged before but turned to be memorable too). I also thank him for creating an energetic and dynamic environment where I resonated intensively with all the other talented members in the Mesoscopic Optics and Quantum Electronics Laboratory. His enthusiasm and passion for research and education will be a life-long inspiration for me. My sincere appreciation also goes to Professor Tatsuo Itoh, Professor Mona Jarrahi, Professor Chandra J. Joshi and Professor Károly Holczer for their stimulating discussions, invaluable motivation and their efforts while serving on my committee.

I would like to thank all my past and present group members who I have been fortunate to interact with. Firstly, I would like to thank Dr. Shu-Wei Huang, now a professor at Boulder, who has been my source of knowledge and helped me on several projects on frequency combs. He tackled many problems with his brilliant ideas and comprehensive backgrounds. He has always been inspiring with his continuous pursuit for scientific breakthrough and his collaborative working ethic. I thank Dr. Jiangjun Zheng, who showed me fiber-to-chip coupling system in my first experiment at Columbia, as well as helped my initial training on a series of software. His rich experience in engineering and prudent attitude towards work influenced me a lot. I also thank Dr. Tingyi Gu, now a professor at Delaware, who once stayed late night with me in the lab to help on the measurements of photonic crystal nanocavities and shared with me the excitement in conducting research. Her extreme enthusiasm and perseverance on research is unforgettable. Dr. Zhenda Xie, now a professor at Nanjing

University, helped build temperature stabilization system, which served for many of my experiments. His talents as both a creative physicist and rigorous engineer are always great sources to learn from. My thanks also go to James McMillan, for his kind sharing of his knowledge on equipment and precision metrology and for his initial effort on microresonator frequency combs. The projects on frequency combs would certainly be less comprehensive without the fruitful discussions with all the great scientists in the field, especially Dr. Jinkang Lim, Dr. Wenting Wang, Dr. Heng Zhou, Abhinav Kumar Vinod and Hao Liu. I also thank all other current and former members for sharing their thoughts with me, Yoo-Seung, Jaime, Yi-Ping, Eli, Jiahui, Susu, Jin Ho, Yongnan, Jiagui, Yongjun, Bowen, Baicheng, Lingzhi, Ziqiang, Vito, Serdar, Pin-Chun, Felice, Xiujian, XinAn, Norman, Yong-Chun, Hao Zhou, Matthew, Ali and Francesco. I appreciate the interaction with these talented and motivated colleagues.

I am grateful to have chance to collaborate with many excellent groups. Firstly, I would like to thank Prof. Tanya Zelevinsky's group at Columbia University, who generously shared their Menlo frequency comb and lab space at Columbia University for our initial studies on frequency combs. Her critical insights, along with her dedication to science and education, has taught me a lot. I also thank her group members especially Dr. Bart H. McGuyer and Dr. Mickey P. McDonald for their help and patience on setting up the Menlo comb. I thank Professor Karen Bergman's group from Columbia too for their supportive loan of their equipment in the comb studies. The key application of frequency combs in the terahertz field was realized together with Professor Jarrahi's group. I appreciate the interaction with the energetic environment from her group along with her encouragement and help throughout the work. I had the pleasure to work closely with her group member Dr. Shang-Hua Yang, now a professor at Taiwan, who was always excited at new findings and problem solving. I thank them for sharing their expertise in the areas and motivations in pushing the frontiers.

The work would not have been realized without the device nano-fabrications from Institute of Microelectronics, Singapore. We thank our collaborators Prof. Mingbin Yu and Prof. Dim-Lee Kwong there.

I would also like to thank the staff members in Electrical Engineering, especially Deeona Columbia and Ryo Arreola, for helping with paperwork and arrangements including in urgent cases. I thank the supportive environment from the university in daily campus life.

The highly academic and innovative environments at Columbia and Tsinghua University equipped me with essential backgrounds and skills in engineering. For the coursework that helped on my doctoral research, I thank Professor Dirk Englund, Professor Richard Osgood, Professor Irving Herman, Professor Nanfang Yu and Professor Shalom Wind. I specially thank Professor Changxi Yang and Professor Xiaosheng Xiao, for their introduction of optics research areas to me and their training during my undergraduate studies. My thanks also go to Professor Dahai Ren, who introduced me to researches in precision metrology and micro-scale devices when I was a junior.

My warm appreciation goes to my friends for sharing many memorable moments with me, exploring the cities, enjoying arts and playing sports. Their friendships created multi-dimensional space for my life and kept me enlightened and healthy. They are great treasure for me.

Last but not least, I thank my parents for their everlasting love and unwavering support. I would not reach this far without their support in advanced educations and in every moment of my life. Given their own expertise in Chinese medicine and Chinese literature, they encourage me to explore my own path and develop my own perspective and solutions since my childhood. I love them and am forever indebted to them.

Biography

Jinghui Yang is a Ph.D. candidate in the Electrical Engineering at University of California, Los Angeles, where she conducted the research of chip-scale optical frequency combs, ultra-stable clockwork, and nonlinear dynamics in micro-devices in Prof. Chee Wei Wong's research group. Throughout her doctoral work, she has contributed to more than 10 journal papers and 15 conference presentations. She has received awards including Maiman Outstanding Paper Competition Finalist with Honorable Mention, SPIE Optics and Photonics Education Scholarship, Chinese-American Engineers and Scientists Association of Southern California Scholarship, and Samueli Foundation Fellowship. Her current research interests include ultrafast optics, precision metrology and light sources in the chip-scale devices and systems. Jinghui received the M. Phil. and M.S. in Mechanical Engineering from Columbia University in 2015 and 2013 respectively, and B.S. in Precision Instrument from Tsinghua University in 2011.

Chapter 1.

Introduction

1.1. Microresonator-Based Frequency Combs

Optical frequency combs, since their inception more than a decade ago [1], has brought widespread impacts on sciences and technologies and been awarded the Nobel Prize in Physics in 2005 [2,3]. Researches on optical frequency combs have led to tremendous breakthroughs in precision spectroscopy [4–6], frequency metrology [7,8], and astrophysical spectrography [9,10]. They are also promising platforms for optical communication [11,12], stable microwave signal generation [13], and arbitrary optical waveform generation [14]. The current benchmark laser systems for optical frequency combs are self-referenced femtosecond mode-locked lasers [15].

However, continuous-wave (cw) pumped microresonators emerge as promising alternative platforms for optical frequency comb generation in the last decade leveraging on breakthroughs in semiconductor nanofabrications [11,16–20]. Microresonator-based frequency combs are generated by modulation instability and four wave mixing, facilitated by the high quality factors and small mode volumes of these microresonators. Microresonator-based optical frequency combs, or Kerr frequency combs, are unique in their compact footprints and offer the potential for monolithic electronic and feedback integration, thereby expanding the already remarkable applications of frequency combs. To this end, microresonator-based optical frequency combs, have recently been examined in whispering gallery mode (WGM) structures [19,21–26] and planar ring geometries [12,27]. Planar ring cavities are particularly attractive since: 1) the resonator and the coupling waveguide can be monolithically integrated, reducing the sensitivity to the environmental perturbation; 2) the resonator only supports a few discrete transverse modes, increasing the robustness of coupling into the designed resonator mode family; and 3) the cavity dispersion and the comb spacing can be engineered separately, offering the flexibility to tailor the cavity dispersion for efficient and broadband comb generation.

1.2. Dissertation Overview

This dissertation is dedicated to several key findings in precise optical frequency synthesis in the silicon photonics platform.

Chapter 2, as a comparatively independent chapter, examines the first self-sustained radio frequency oscillators in silicon heterostructured photonic crystal nanocavities with high quality factor to mode volume ratios (*Q/V*) [28]. The pulsation is a cooperative temporal response from thermal and free carrier dispersions in an optical resonator, generating radio frequency (RF) tones with continuous wave (cw) input. Effective tuning of the RF tones is enabled by laser input parameters, verified by nonlinear coupled mode theory tracking the dynamics of photons, free carrier populations and temperature variations.

Chapter 3 to Chapter 8 are thorough discussions on frequency combs in silicon nitride microresonators towards precise optical frequency synthesis:

Chapter 3 provides an overview on the experimental setups and methods, and discusses globally-normal dispersion mode-locked frequency combs and one of the shortest pulse (74 fs) formation on chip and analyzes the mode-locking mechanism in microresonator combs [20]. The observation is supported by ultrafast optical characterizations and numerical modeling [24,25]. With the continuous-wave driven nonlinearity, the pulses sit on a pedestal, akin to a cavity soliton. The importance of pump detuning and wavelength-dependent quality factors as well as modal interactions in shaping the pulse formation and pulse structure are identified. The importance of bandpass filtering effect in stabilizing and shaping the pulses in this dispersion regimes is demonstrated experimentally and numerically. Closed-form solution of the master equation with appropriate approximations is derived by variational method, facilitating the design of low-noise mode-locked microresonator Kerr combs.

Chapter 4 discusses the observation and analysis of self-injection locking, one of the key nonlinear processes governing the comb coherence by a bichromatic pump [31]. By introducing a low-power on-resonance seeding laser which is phase locked to the major pump, we detail the observation of comb transitions into coherent states and the dynamics of self-injection locking between different comb families. Within the locking range of 40 MHz in the 430 GHz carrier, deterministic control of comb repetition rates can be enabled by a microwave synthesizer used in the phase locked loop.

Chapter 5 demonstrates a Kerr frequency comb oscillator with electronic-detectable spacing, with its low phase-noise feature characterized [32]. The comb spans nearly half an octave with more than 3,600 coherent comb modes. Single-sideband (SSB) phase noise analysis reveals low phase noise floor in free-running Kerr frequency combs, -130 dBc/Hz at 1 MHz offset for the 18 GHz carrier. The frequency stability is characterized, and the measured free-running Allan deviation is 2×10^{-8} in 1 s, consistent with the frequency fluctuations caused by the pump wavelength drift. Feedback stabilization further improves the frequency stability to 7×10^{-11} in 1 s.

Chapter 6, as continuous effort based on Chapter 5, achieves the first fully stabilized CMOS-compatible broadband optical frequency synthesizer with a frequency relative uncertainty of 2.7×10^{-16}, down to fundamental limits [26]. The comb's two degrees of freedom, one of the comb line frequencies and the comb spacing, are phase locked to a known optical reference and a microwave synthesizer respectively. Active stabilization on the comb spacing improves the RF stability by six orders of magnitude, reaching residual instrument-limited close-to-carrier (10 Hz) phase noise of -70 dBc/Hz and Allan deviation of 3.6 $\mathrm{mHz}/\sqrt{\tau}$. The demonstrated system provides a promising compact and reproducible platform for coherent spectroscopy, sensing, optical clockwork, and astronomical observations.

Chapter 7 discusses on one of the key applications of microresonator frequency combs in the coherent terahertz radiation with high optical-to-THz conversion efficiencies [33]. Expanded stability zone of Turing rolls of Kerr frequency combs is strategically achieved by incorporating the local mode hybridization effect, leading to globally stable Turing pattern formation with enhanced pump-to-comb conversion efficiency of 45% and an elevated peak-to-valley contrast of 100. The stationary Turing pattern is discretely tunable across 430 GHz on a THz carrier, with a fractional frequency sideband non-uniformity measured at 7.3×10^{-14}. The free-running Turing roll coherence, 9 kHz in 200 ms and 160 kHz in 20 minutes, is transferred onto a plasmonic photomixer for one of the highest power THz coherent generation at room-temperature, with 1.1% optical-to-THz power conversion. Its long-term stability can be further improved by more than two orders of magnitude, reaching an Allan deviation of 6×10^{-10} at 100 s, with a simple computer-aided slow feedback control. The demonstrated on-chip coherent high-power Turing-THz system is promising to find applications in astrophysics, medical imaging, and wireless communications.

Chapter 8 discusses a universal modality of frequency comb, featuring the satellite comb formation exceeding conventional phase matching bandwidth. This is enabled by multiple phase matching in parametric oscillation process in the nonlinear Kerr medium through cavity dispersion control. The concept can lead to spectrally-wide optical frequency combs with high conversion efficiency in silicon nitride microresonators driven with a continuous-wave pump. Particularly two satellite comb clusters at ≈ 1.3 μm and 2.0 μm regimes are symmetrically generated simultaneously with the central comb. The intensities of the satellite combs are comparable with the first generated parametric sideband near the pump, with a demonstrated record high external conversion efficiency reaching up to -30 dB. The spectral positions, RF amplitude noise, and evolution dynamics of the satellite combs are detailed under different pumping conditions. The demonstrated satellite comb structures and their formation with multiple phase matching serve as a unique platform for carrier envelope phase stabilization as well as coherent light sources covering extended spectral regimes.

Chapter 9 provides concluding remarks and future work plans.

Chapter 2.

Radio Frequency Self-Pulsations in Monolithic High-*Q/V* Heterostructured Photonic Crystal Cavities

2.1. Introduction

Among the various building blocks on photonic chips, photonic crystal (PhC) waveguides and cavities are an indispensable family that have realized tremendous functionalities and applications since their invention of two decades [34,35]. Known as semiconductors of light [36], these PhC structures hold and control the photons by the artificially introduced detect in the periodic structures [37]. PhC cavities feature with their ultra-small modal volumes and long photon lifetimes, leading to their functional integrated devices and systems such as all-optical switch and logic gates, optical buffers [38], low-threshold Raman lasers [39,40], cavity quantum electrodynamics [41] and sensing.

This chapter particularly discusses the phenomena of regenerative oscillation, also called self-induced oscillation or self-pulsation, in the silicon photonic crystal nanocavities. It is a cooperative temporal response due to thermal and free carrier dispersions in an optical resonator, generating radio frequency (RF) tones with continuous wave (CW) input. Observations of regenerative oscillation in one dimensional (1D), 2D [42–48], 2.5D and 3D photonic resonators [49–54] are reported in various material structures. As silicon photonic crystals provides a CMOS compatible platform, considerable studies on low energy switching and passive tuning are addressed in silicon-based devices [42,55–57], with potential in chip-scale tunable RF oscillators towards all-optical communication systems [58]. Optical thermal and free carrier bistability were demonstrated in the monolithic photonic crystal cavities with high *Q/V* ratio, enabled by strong light-matter interaction at sub-milliwatt power levels [39,55] including pulsed carrier switching [59]. Here we show our first observations of regenerative oscillation in a heterostructured cavity with quality factor (*Q*) ~ 500,000 and mode volume (*V*) ~ 0.11 μm^3 (*Q/V* ratio of ~ 10^7 μm^{-3}), with threshold of 79 μW continuous wave input. Temporal and spectral domain observation of regenerative oscillation in monolithic silicon heterostructured photonic crystals cavities with high quality factor to mode volume ratios (*Q/V*). The results are interpreted by nonlinear coupled mode theory (CMT) tracking the dynamics of photons, free carrier populations and temperature variations. We experimentally demonstrate effective tuning of the radio frequency (RF) tones by laser-cavity detunings and laser power levels, confirmed by the CMT simulations with sensitive input parameters.

2.2. Observations of Self-pulsations in High-Q/V Heterostructured Photonic Crystal Cavities

The examined double-/multi- heterostructured photonic crystal cavities are fabricated via 248 nm deep-UV photolithography and reactive ion etching on 250 nm-thickness silicon-on-insulator wafers. A scanning electron microscope (SEM) image in Figure 2-1a shows a typical double-heterostructure with a lattice constant (a_1) of 410 nm, air hole radii 0.276a1, and increasing lattice constants of 415 nm and 420 nm (a_2) in the cavity region; the waveguides with length of 112a_1, width 1.0a_1 and 9 layers of air-holes separated from the cavity. 2 μm oxide underneath the photonic crystal cavity is removed by buffered oxide wet etching. To achieve optimized fiber-chip-fiber coupling, inverse tapered couplers with an oxide over-cladding are integrated with the waveguide. Inset of Figure 2-1a shows the 3D finite-difference time-domain (FDTD) simulations of the electric-field distribution, with the cavity modeled to have an intrinsic quality factor in excess of ~10^6 and modal volume V_m of ~$1.2(\lambda_0/n)^3 = 0.11$ μm^3. To sustain oscillation in silicon photonic crystals, the threshold power of self-pulsation steadily increases as Q/V ratio decreases. For devices with Q factor smaller than 100,000, regenerative oscillation is hardly observed even at 1 mW power levels.

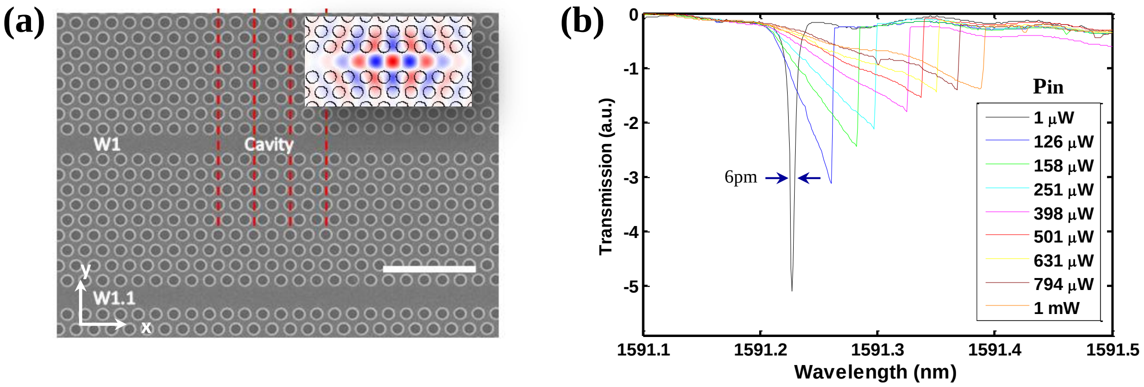

Figure 2-1. Ultrahigh-Q/V platform for self-induced regenerative oscillations.
(a) Scanning electron micrograph of a double-heterostructured high-Q photonic crystal cavity (scale bar: 2 μm); (inset) 3D finite-difference time-domain calculated electric field profile (E_y) of the high-Q mode supported by a double-heterostructured cavity (Q_{in} = 480,000, mode volume = 0.11 μm^3). (b) Measured transmission spectra (wavelength scanned from low to high) with normalized input power from 1 μW to 1 mW. The linear transmission is measured at 1 μW (black symmetric lineshape).

The high-Q photonic crystal cavity is characterized through spectral transmission, by sending the CW coherent transverse-electric light from a tunable laser onto chip through polarization controllers and piezoelectric-feedback-controlled lensed fibers. The average power level and temporal response of output light are monitored by power meter and fast photodetector (New Focus 1554B, 12 GHz bandwidth) respectively. The fast photodetector is connected to an electronic spectrum analyzer (Agilent 5052B) and a high-speed oscilloscope (Tektronix, 4 GHz bandwidth) to obtain the time-domain response of the high-*Q* cavity. The environmental thermal fluctuation of the chip is minimized by a thermoelectric cooling module driven by a benchtop temperature controller (Thorlabs TED200C).

The measured optical transmission spectra with different input powers are shown in Figure 2-1b Cavity resonance shifts from 1591.23 nm to 1591.39 nm as input power (all referred to the powers or estimated powers inside the cavity, same below) increases from 1 μW to 1 mW. By curve-fitting the transmission spectrum of cold cavity, we obtain the cavity linewidth of ~ 6 pm and 5 dB extinction ratio, corresponding to loaded and intrinsic *Q* factors of 266,000 and 480,000 respectively. The *Q* factors are slightly lowered by the imperfections in nanofabrication [60]. At higher input powers the cavity transmissions become asymmetric due to thermal hysteresis effects, indicated by the sharp transition resulting from the bistable states [55,58].

With the input power well beyond the threshold of bistability, temporal self-pulsation can be observed at a range of laser-cavity detunings. For an input CW laser power of 800μW, the output self-pulsation waveform is shown in Figure 2-2a, at laser-cavity detunings of 120 pm, 190 pm and 267 pm respectively. The dependence of oscillation periods, dip widths (corresponding to the pulse width of cavity mode) and duty cycles (ratio between the dip width and the period) on laser-cavity detunings are systematically measured and summarized in Figure 2-2b. The period of time domain pulsation is around tens of ns to 100 ns, with duty cycle varying from 20% to 60%. The upper and lower bounds of detuning in the oscillation region are illustrated in Figure 2-2c. Only within the bounded laser-cavity detuning ranges can the stable oscillation be observed, which displays decreased standard deviation of the time period of temporal pulses, along with much lower phase noise and amplitude noise compared to the oscillatory output in other ranges (e.g. chaotic states) [61]. Higher input power linearly increases the bound of detunings regions for the regenerative oscillations. For laser-cavity detunings smaller than 70 pm or larger than 220 pm, the oscillation is unstable and hard to measure.

Frequency domain response of the self-sustained regenerative oscillations is simultaneously monitored by the RF spectrum analyzer. The RF spectrum of the oscillation at the detuning of 160 pm is shown in Figure 2-2d; the experimental relation between the fundamental RF tone and laser-cavity detuning is plotted in the inset of Figure 2-2d, which are the Fourier transforms of the time-domain measurements such as in Figure 2-2a. As detuning increases, initially chaotic excitation of the oscillation stabilizes, and more coherent oscillatory signals are generated, until the detuning increases to the upper bound of the detuning. We also measured the single sideband phase noise and amplitude noise of the fundamental mode for regenerative oscillation. When stable temporal oscillation is generated, the amplitude noise level decreases by ~ 40 dBc/Hz.

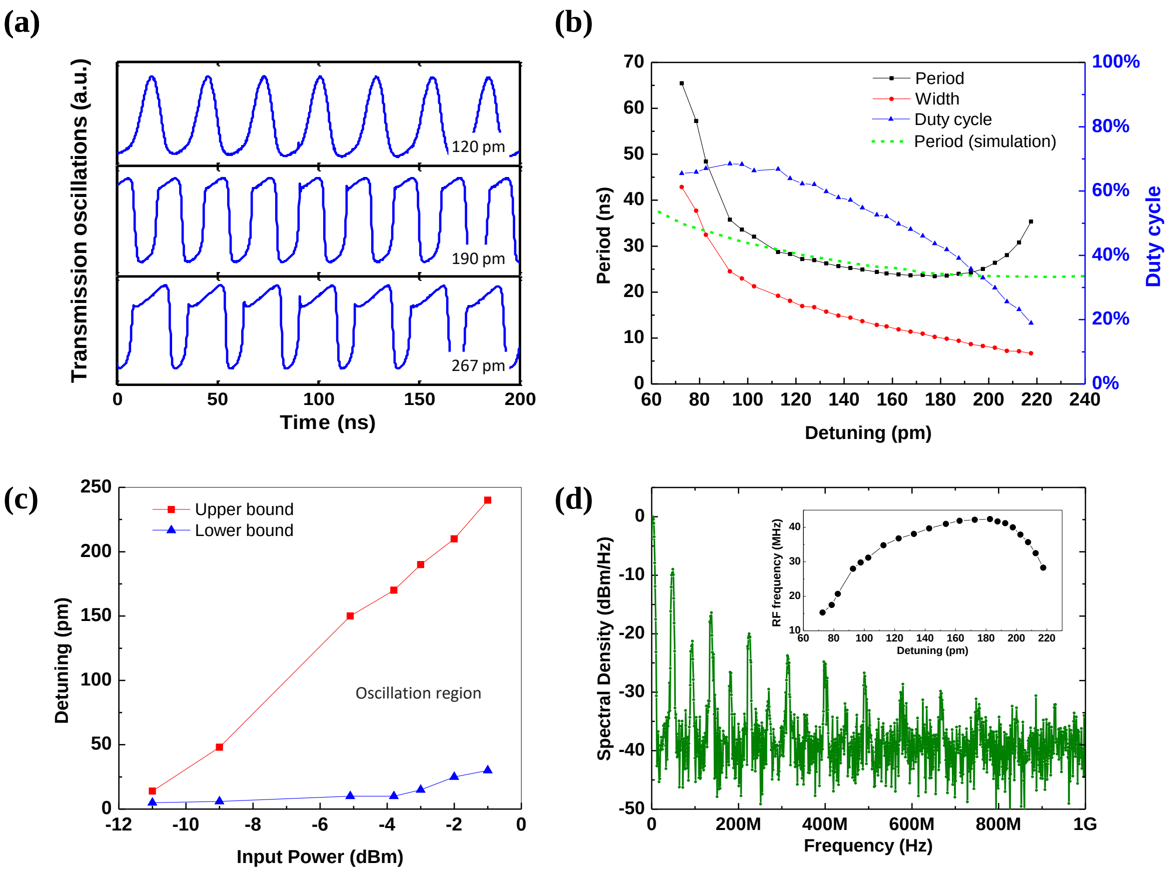

Figure 2-2. Experimental observation of regenerative oscillations in a high-Q double-heterostructured photonic crystal cavity, controlled by input laser power and laser-cavity detuning.

(a) Observed time domain periodic pulsation with laser-cavity detunings of 120 pm, 190 pm and 267 pm at 800 μW input power. (b) Period, dip width, and duty cycle versus detuning, summarized from a set of temporal observations as in panel (a). (c) Measured upper and lower bound of detuning range for oscillations with $Q = 480{,}000$. (d) RF spectrum at the wavelength detuning of 163 pm; (inset) measured fundamental RF frequency versus detuning at 800 μW input power.

2.3. Analysis on Cavity Mode Dynamics by Nonlinear Coupled Mode Theory

The temporal dynamics, phase-space diagram and frequency domain spectrum under different input conditions are simulated as shown in Figure 2-3. In the self-pulsation process, the dynamics of the cavity mode is modified by several nonlinear effects [45,56,62], i.e., thermo-optic effect, free-carriers dispersion and Kerr nonlinearity. The dispersion induced by Kerr effect is orders of magnitude weaker than the other two effects in silicon material devices. Competing resonance shifts therefore occurs – red shift caused by thermo-optic effect and blue shift by free-carriers dispersion, resulting in a modification of resonance wavelength temporally and periodically. We model the transmissions with time-domain nonlinear coupled mode theory [63,64], where the dynamics of mode amplitude *a* (square root of mode energy), the free carrier density *N* and the cavity temperature shift ΔT are given by:

$$\frac{da}{dt} = (i(\omega_L - \omega_0 + \Delta\omega) - \frac{1}{2\tau_t})a + \kappa\sqrt{P_{in}} \tag{2-1}$$

$$\frac{dN}{dt} = \frac{1}{2\hbar\omega_0\tau_{TPA}}\frac{V_{TPA}}{V_{FCA}^2}|a|^4 - \frac{N}{\tau_{fc}} \tag{2-2}$$

$$\frac{d\Delta T}{dt} = \frac{R_{th}}{\tau_{th}\tau_{FCA}}|a|^2 - \frac{\Delta T}{\tau_{th}} \tag{2-3}$$

where the total loss rate is $1/\tau_t = 1/\tau_{coup} + 1/\tau_{in} + 1/\tau_{TPA} + 1/\tau_{FCA}$. $1/\tau_{coup}$ and $1/\tau_{in}$ are the loss rates coupled into waveguide and into free-space respectively. The free carrier absorption rate $1/\tau_{FCA} = c\sigma N(t)/n$, and the two-photon absorption rate is defined as $1/\tau_{TPA} = \beta_2 c^2/n^2/V_{TPA}|a|^2$, where β_2 is the effective two-photon absorption coefficient of silicon. V_{TPA} and V_{FCA} are mode volumes of two-photon absorption and free carrier absorption respectively. The parameters used in the numerical simulation are listed in Table 2-1. Based on the model, the cavity stored energy *U(fJ)*, free-carrier density *N(m^{-3})* and temperature variation *ΔT(K)* are simulated on the left panels of Figure 2-3; the phase diagrams of mode amplitude are shown on the middle panels; and the fast Fourier transform (FFT) spectrum in the frequency domain on the right. The selected input conditions are: (a) input power 800 μW, detuning 160 pm; (b) input power 800 μW, detuning 30 pm; (c) input power 100 μW, detuning 30 pm, where (a) matches with our experimental measurements.

Table 2-1. Parameters for coupled mode theory simulations.

Parameter	Symbol	Value
Refractive index of Si	n_i	3.475
Effective index of Si	n_{eff}	2.77
TPA coefficient	β_2 (m/W)	$8\text{x}10^{-18}$
Kerr coefficient	n_2 (m^2/W)	$4.4\text{x}10^{-18}$
Free-carrier lifetime	τ_{fc} (ns)	0.5
Constant-pressure specific heat capacity	$c_{p,Si}$ (J/Kg K)	$0.7\text{x}10^3$
Density of Silicon	ρ_{Si} (kg/m^3)	$2.33\text{x}10^3$
Thermal resistance	R (K/mW)	50
Temperature dependence on refractive index	dn/dT (K^{-1})	$1.86\text{x}10^{-4}$
Loaded Q	Q_{in}	266,000
Intrinsic Q	Q_v	480,000

To match the experimental RF fundamental mode and parameter space of detuning (detailed in Figure 2-5a and Figure 2-5b), we adjust the initial conditions (I. C.) of internal cavity energy, free carrier density and temperature variation to be non-zero for larger detunings (e.g. larger than 50 pm at 800 μW input power). Physically the concept is analogous to the initial photons inside the microcavity before the pulsation is ignited. The non-zero I. C.

in the model is derived iteratively in the range of temporal dynamics, e.g. in Fig. 3a, we set the initial condition of the mode energy to be 4 fJ, the free carrier density N to be 4×10^{21} m^{-3} and the cavity temperature shift ΔT at 2.2 K; it matches well with the observed pulsation as shown in the RF spectrum in the inset of the right panel (the same as Figure 2-2d). As a comparison, zero I. C. can sufficiently initiate the self-pulsation for detunings less than 50 pm from simulation; the relation between duty cycle and detuning matches experiment qualitatively. Figure 2-3b shows the simulated self-pulsation at detuning of 30pm, with zero I. C., i.e. $U_0 = 1\times10^{-15}$ fJ, $N_0 = 1\times10^{19}$ m^{-3} (an estimated quiescent value for silicon), $\Delta T_0 = 0.1$ nK. Our experimental result, however, shows unstable or chaotic oscillation with detunings less than 60 pm as mentioned above, even though the self-pulsation in smaller or negative detunings are observed or predicted in other types of devices [48,65,66]. In the frequency domain, condition (b) shows a higher harmonic level indicating a lower purity of signal, which suggests weaker device performance. The phase diagrams of (a) and (b) are similar, both with complex limit cycles. At a lower input power such as in the condition (c), a purer signal is more likely to be excited, with only one limit cycle and lower harmonics as shown in Figure 2-3c; however, it is not observed experimentally possibly due to the low intensity or signal-to-noise ratios compared to condition (a).

Note that, the cavity dynamics is also in accompany with cavity resonance shift. An example with non I. C. condition in condition (b) is shown in Figure 2-4. The cavity stored energy begins to fluctuate with respect to the cavity resonance shift mediated by the initial photons in the cavity (blue curve). After a certain time, the cavity is driven to the periodic pulsation state (red curve), where a stable cycle of the relationship forms and recurs.

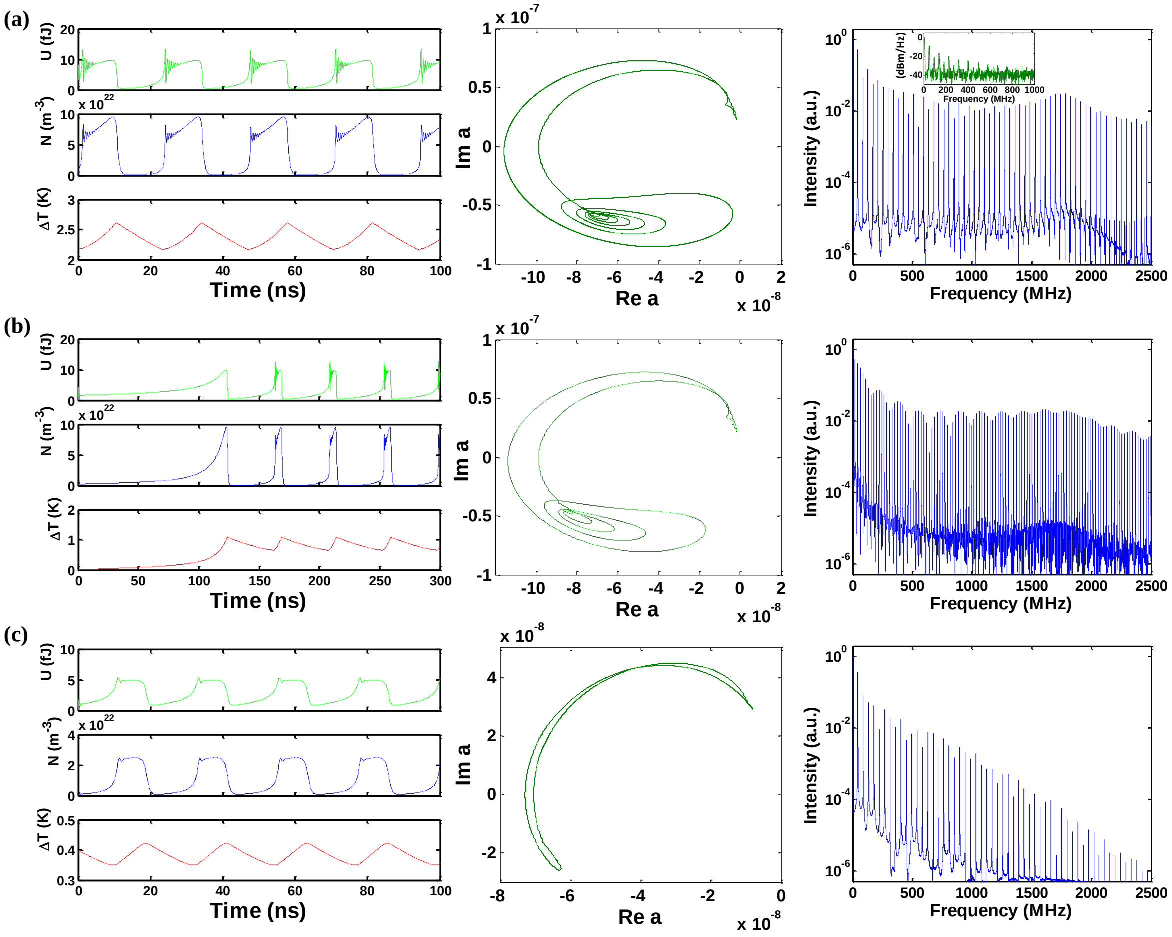

Figure 2-3. Coupled mode theory simulations of the temporal dynamics (cavity stored energy U(fJ), free-carrier density N(m^{-3}), and temperature variation ΔT(K)), phase-space reconstruction of normalized mode amplitude, and frequency domain spectrum respectively under selected input conditions.

(a) input power 800 μW, detuning 160 pm, non-zero initial conditions (I. C.) ($U_0 = 4$ fJ, $N_0 = 4\times10^{21}$ m^{-3}, $\Delta T_0 = 2.2$ K); (b) input power 800 μW, detuning 30 pm, zero I. C. ($U_0 = 1\times10^{-15}$ fJ, $N_0 = 1\times10^{19}$ m^{-3}, $\Delta T_0 = 0.1$ nK); (c) input power 100 μW, detuning 30 pm, non-zero I. C. ($U_0 = 1$ fJ, $N_0 = 5\times10^{20}$ m^{-3}, $\Delta T_0 = 0.4$ K). (a) corresponds to our experimental conditions; (inset of right panel of (a)) the measured RF spectrum, with the unit of dBm/Hz for y-axis.

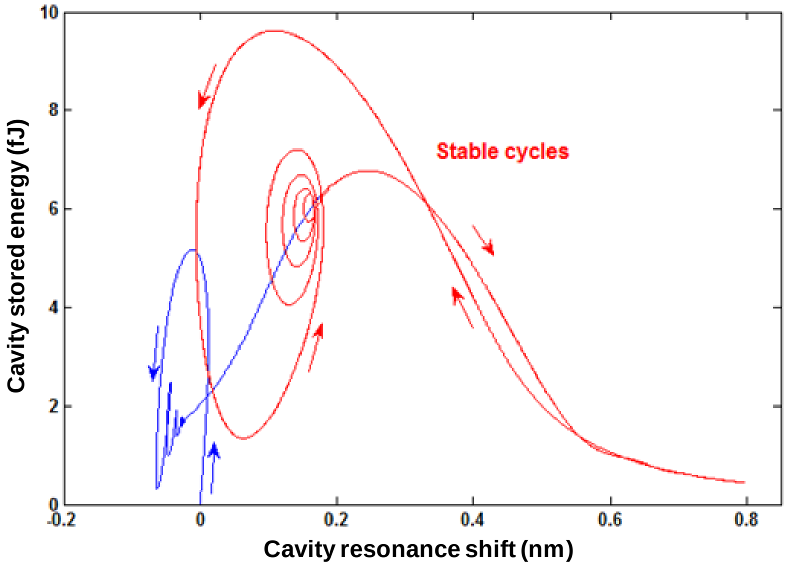

Figure 2-4. Relative cavity resonance shift in accompany with cavity stored energy with non-zero I. C. in condition Figure 2-3b. Temporal resolution in the simulation is 1 ps. The cavity stored energy begins to fluctuate with respect to the cavity resonance shift mediated by the initial photons in the cavity (blue curve). After a certain time, the cavity is driven to the periodic pulsation state (red curve), where a stable cycle of the relationship forms and recurs.

We point out that, high frequency oscillations up to ~ 2 GHz can occur as shown in the simulation of the temporal dynamics and FFT spectrum of Figure 2-3a, with decreased damping through improved thermal conductivity and cavity stored energy (as shown). Experimentally this is not observed due to either comparatively lower thermal conductivity in the device cavities or the limited data acquisition bandwidth. Similar phenomena are observed and explained in microdisk resonators [43], and silicon photonic crystal cavities [66] where non-damped and sinusoidal GHz oscillations is obtained with material surface treatment for the devices introduced.

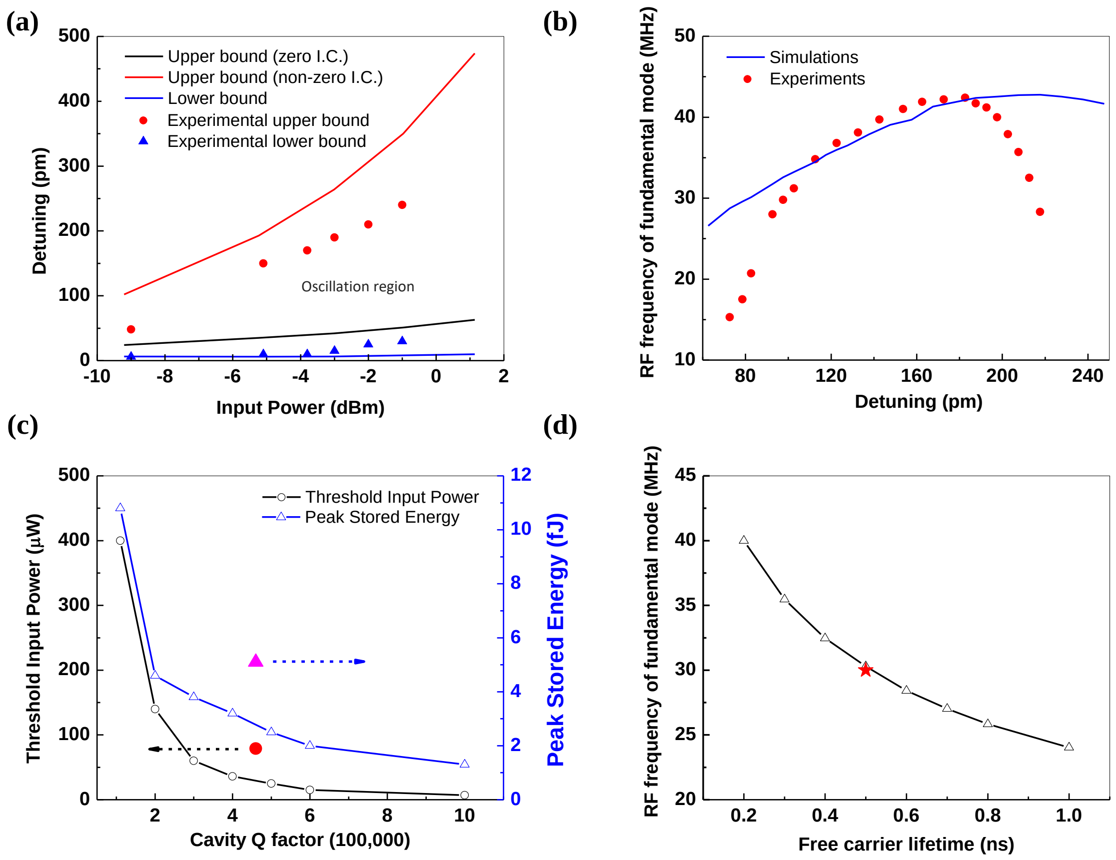

Figure 2-5. Comparison between simulations and experiments of self-pulsations.

(a) Simulated up and low bound of detuning range for oscillations for Q = 480,000. Red solid and dashed lines show the upper bound with non-zero (U = 4 fJ, $N = 4\times10^{21}$ m^{-3}, ΔT = 2.2 K) and zero ($U = 1\times10^{-22}$ fJ, $N = 1\times10^{-10}$ m^{-3}, ΔT = 0.1 nK) initial condition (I.C.) respectively, corresponding to the cases for the cavity with or without initial photons before the nonlinear behavior occurs. Experimental results (red and blue dots) are shown as a comparison with simulation. (b) Simulated (line) and measured (dots) RF frequency of fundamental mode of self-pulsation versus detuning. (c) Threshold input power (black) and peak intracavity energy (blue) as functions of cavity Q factor. Experimental results marked as a solid dot/triangle. The threshold power for oscillation is beyond 1 mW in the cavity with Q < 100,000. (d) Free carrier lifetime dependent oscillation features characterized by the generated fundamental RF frequencies with laser-cavity detuning at 10 pm. At given conditions, the measured RF frequency (red star) indicates the free carrier lifetime in the high Q cavity to be 500 ps.

Following the initial condition treatment as mentioned above, the parameter space (input power and detuning) and RF frequency of the fundamental mode are obtained through simulation by finely adjusting parameters in the model, e.g. free carrier lifetimes and mode volumes. The results are shown in Figure 2-5a and Figure 2-5b with experimental data as comparisons respectively. Figure 2-5c depicts the simulated threshold power and cavity stored energy with different *Q* factors, which illustrates that regenerative oscillation will only occur in high-*Q* devices, with the threshold enhanced by the wavelength-scale photonic crystal modal volumes. The threshold *Q* factor for observing the oscillation in silicon based photonic crystals is about 110,000, at 400 μW power level. Experimental data is highlighted, where the internally stored cavity energy is estimated to be 5 fJ [67].

In order to accurately estimate the free carrier lifetime, which is a function of free carrier density [43,45], we plot the dependence of the RF fundamental mode versus carrier lifetime, and map the experimental measurement in Figure 2-5d, where we find 0.5 ns as the best fit for experiments. The free carrier lifetime can be electro-optically controlled by placing lateral bias on the high *Q* cavity, for a potential voltage controlled local oscillator towards on-chip signal processing.

Note that this work discusses the case with cw excitation, whereas in cases with pulsed excitation, where the heat generated from thermal-optic effect can have time to dissipate, the duty cycle and repetition rate of the input can vary accordingly [68]. For instance, very low duty cycle excitation allows the cavity to cool down before the arrival of the next pulse, resulting no heating effect to the cavity; a repetition rate faster than the thermal relaxation time of the cavity will prohibit sufficient heat dissipation after each excitation cycle, leading to accumulated heat inside the cavity and a redshift of the cavity resonance. This will offer another set of degree of freedom to engineer the self-induced pulsations.

2.4. Summary

In this chapter, we discuss the first observations of self-sustained regenerative pulsation in photonic crystal heterostructured cavities with Q/V ratio of 107 μm^{-3}, with detailed measurements and numerical interpretations. As the input power into the cavity increases up to ~ 80 μW (internal stored energy up to ~ 5 fJ), the transmission intensity self-excites into an oscillatory behavior in the time-domain. The period of time domain pulsation is around 100 ns, with duty cycle varying from 20% to 60%, controllable by the input powers and detunings. The oscillation region is mapped onto various laser-cavity detunings versus coupled powers. The complete nonlinear coupled mode theory simulation illustrates the parameter space, and specifies the effective free carrier lifetime in the cavity. The comparison between experiments and simulations under different input conditions is described and discussed. The phenomena and studies allow lower power operation for all-optical signal processing and yield an alternative approach towards tunable frequency oscillators by controlling the incident drive signal.

Chapter 3.

Mode-Locking and Ultrashort Pulse Generation from On-Chip Normal Dispersion Microresonators

3.1. Introduction

Kerr frequency comb, or termed as microresonator frequency comb or microcomb, has a different fundamental mechanism from the mode-locked laser based OFC. These frequency combs emerge as promising platforms for compact optical frequency comb generation [11,16,18,19,69–75] through broadband four-wave mixing (FWM). With anomalous group-velocity-dispersion (GVD) and self-phase modulation (SPM), optical solitons can be generated [76,77], and remarkably broad bandwidths [71] and RF-optical stability [69] have been demonstrated. Obtaining anomalous GVD broadly across arbitrary center frequencies, however, is challenging for microresonators [78]. Dispersion engineering by conformal coating [79–81] and waveguide shaping [82] are possible, but often lead to lower cavity optical quality factors (*Q*s). Alternatively, frequency comb and ultrashort pulse generation from normal GVD microresonators has been theoretically predicted [83–85] and comb-like spectra from normal GVD crystalline resonators were recently measured [86,87]. Further investigation into this normal GVD architecture, especially in the time-domain and that of coherent mode-locking, will open up new fields in chip-scale oscillators, waveform generation, and ultrafast spectroscopy.

This chapter discusses our study on globally-normal GVD mode-locked frequency combs on-chip. The observation is supported by phase noise characterization, direct frequency-resolved optical gating (FROG) pulse measurement, and numerical modeling [29,30]. Local dispersion disruption due to modal interactions initiates the comb, prior to support from the globally-normal dispersion. With the continuous-wave driven nonlinearity, the pulses sit on a pedestal, akin to a cavity soliton. We identify the importance of pump detuning and wavelength-dependent quality factors in stabilizing and shaping the pulse structure, to achieve a single pulse inside the cavity. All comb spectral lines are collected in our FROG pulse measurement and the phase-retrieved pulses demonstrate mode-locking down to 74 fs, one of the shortest frequency comb pulse on-chip to date. Numerical modeling of the comb growth and dynamics, capturing the full spectra, the measured GVD and *Q*s, confirms the feasibility of mode-locked frequency comb generation and agrees with our measurements. Furthermore, we demonstrate, both experimentally and numerically, the importance of effective spectral bandpass filtering in stabilizing and shaping the pulses generated in the globally-normal GVD microresonators. We obtain the closed-form solution of the master equation with appropriate approximations, facilitating the design of low-noise mode-locked microresonator Kerr combs.

3.1.1. Si_3N_4 Ring Resonator, Refractive Index and Quality Factor Characterization

An example scanning electron micrograph of the ring resonator and the refractive index of the low pressure chemical vapor deposition (LPCVD) Si_3N_4 is shown in Figure 3-1a. Due to the large refractive index of the Si_3N_4 waveguide, a 600 μm long adiabatic mode converter (the Si_3N_4 waveguide, embedded in the 5×5 μm^2 SiO_2 waveguide, has gradually changing widths from 0.2 μm to 1 μm) is implemented to improve the coupling efficiency from the free space to the bus waveguide. The input-output insertion loss for the waveguide does not exceed 6 dB. The refractive index is measured with an ellipsometric spectroscopy (Woollam M-2000 ellipsometer) and the red curve is the fitted Sellmeier equation assuming a single absorption resonance in the ultraviolet (Figure 3-1b). The fitted Sellmeier equation, $n(\lambda) = \sqrt{1 + \frac{(2.90665 \pm 0.00192)\lambda^2}{\lambda^2 - (145.05007 \pm 1.03964)^2}}$, is then imported into the COMSOL Multiphysics for the waveguide dispersion simulation, which includes both the material dispersion and the geometric dispersion.

The fabrication procedure of our microresonator: First a 3 μm thick SiO_2 layer was deposited via plasma-enhanced chemical vapor deposition on p-type 8” silicon wafers to serve as the under-cladding oxide. Then LPCVD was used to deposit a 725 nm silicon nitride for the ring resonators, with a gas mixture of SiH_2Cl_2 and NH_3. The resulting Si_3N_4 layer was patterned by optimized 248 nm deep-ultraviolet lithography and etched down to the buried SiO_2 via optimized reactive ion dry etching. The sidewalls were observed under SEM for an etch verticality of 88 degrees. The nitride rings were then over-cladded with a 3 μm thick SiO_2 layer, deposited initially with LPCVD (500 nm) and then with plasma-enhanced chemical vapor deposition (2500 nm). The device used in this study has a ring radius of 200 μm, a ring width of 2 μm, and a ring height of 0.725 μm.

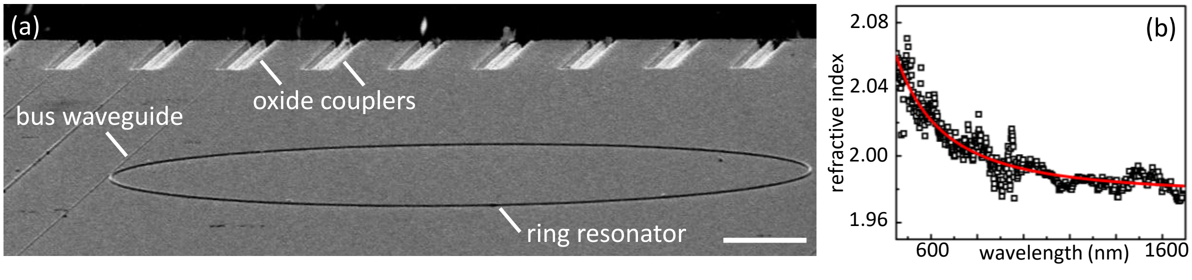

Figure 3-1. Scanning electron micrograph of the chip-scale ring resonator and refractive index measurement.

(a) Layout of the ring resonator with input/output mode converters with less than 3 dB coupling loss on each facet. Scale bar: 50 µm. **(b)** Spectroscopic ellipsometer measurements of the refractive index of the LPCVD Si_3N_4 for the numerical dispersion modeling.

Figure 3-2 shows the wavelength-dependent *Q*-factors of the ring resonator, determined by Lorentzian fitting of cavity resonances. The loaded *Q* reaches its maximum (~1.4M) at 1625 nm and gradually decreases on both ends due to the residual N-H absorption at the short wavelengths and the increasing coupling loss at the long wavelengths. This effective bandpass filter plays an important role in pulse generation from our normal GVD microresonator.

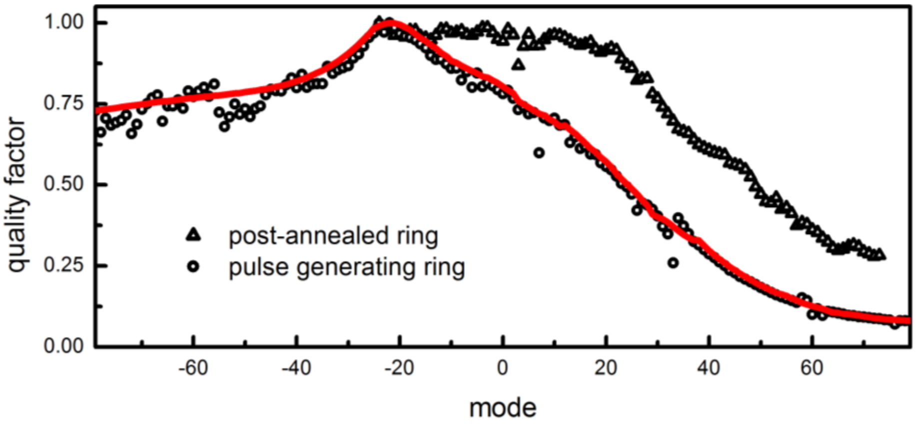

Figure 3-2. ***Q*** **quantification of the resonant modes.**

The intrinsic absorption from the residual N-H bonds results in the loaded *Q*s' roll-off at the short wavelengths (circles). Post-annealing of the Si_3N_4 ring resonator lowers the concentration of the residual N-H and reduces the roll-off (triangles). At the long wavelengths, the increasing coupling loss is responsible for the *Q* roll-off. The red curve is the fit of the loaded *Q*s, used in the numerical simulations.

3.1.2. Dispersion Engineering and Characterization

Figure 3-3 shows the dispersions of the ring resonator calculated with a commercial full-vector finite-element-mode solver (COMSOL Multiphysics), taking into account both the waveguide dimensions and the material dispersion. Modeling is performed on 50 nm triangular spatial grid with perfectly-matched layer absorbing boundaries and 5 pm spectral resolution. Since the ring radius is large, the bending loss and the bending dispersion of the resonator waveguide are negligible in our ring resonators [79]. The fundamental mode (TE_{11}) features small normal group velocity dispersion (GVD) and small third-order dispersion (TOD) across the whole telecommunication wavelength range while the first higher order mode (TE_{21}) possesses large anomalous GVD and large TOD. We define GVD and TOD in accordance with formulas $GVD \equiv \frac{\partial^2\varphi}{\partial\omega^2} = \frac{\lambda^3}{2\pi c_0^2}\frac{d^2n}{d\lambda^2}$ and $TOD \equiv \frac{\partial^3\varphi}{\partial\omega^3} = -\frac{\lambda^4}{4\pi^2 c_0^3}\left(\lambda\frac{d^3n}{d\lambda^3} + 3\frac{d^2n}{d\lambda^2}\right)$. The dispersion profile of a microresonator can be tailored by the cross-sections of the waveguide. Some examples with a zoom-in wavelength range are summarized in Figure 3-4.

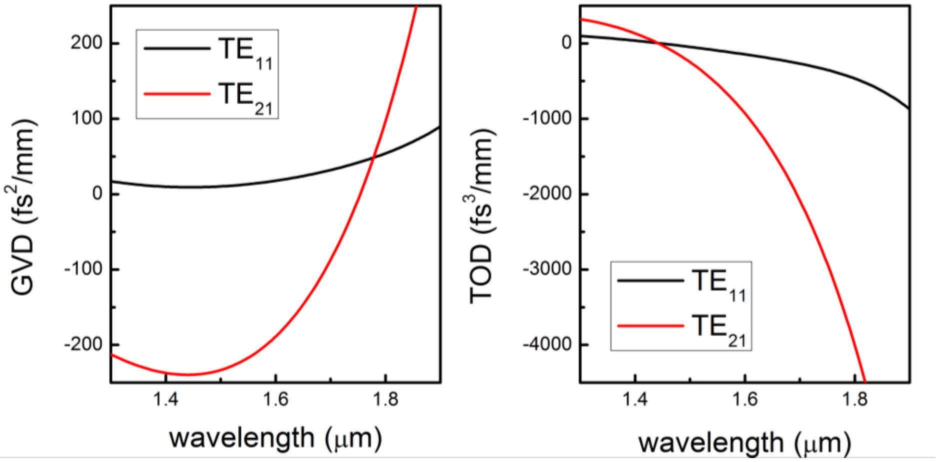

Figure 3-3. Simulated GVD and TOD of the ring resonator.

The fundamental mode features normal GVD across the whole telecommunication wavelength range while the first higher order mode possesses anomalous GVD. The fundamental mode also features small TOD at the telecommunication wavelength range, beneficial for broad comb generation.

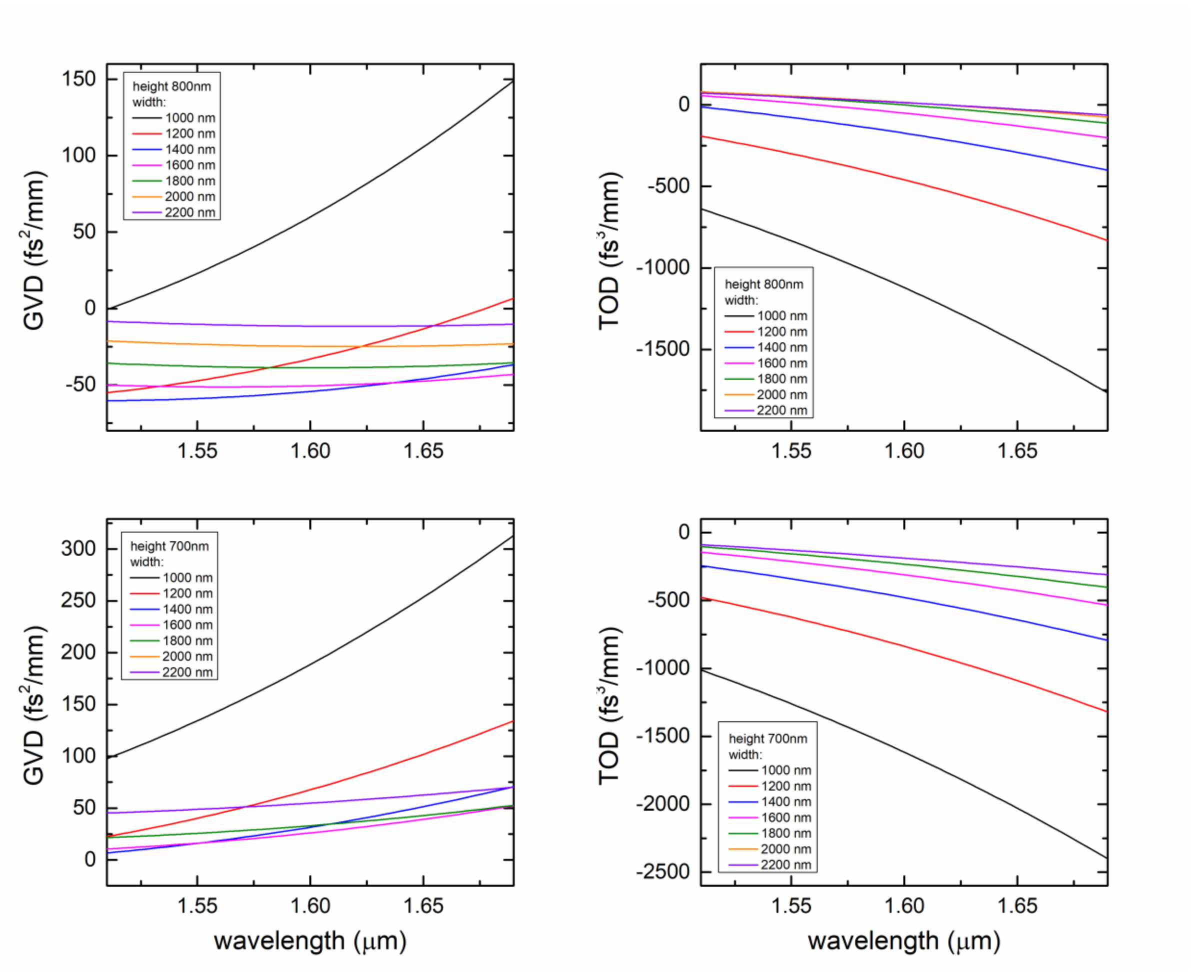

Figure 3-4. Engineering dispersion by waveguide cross-sections.

Simulated GVD and TOD with different waveguide heights (800 nm and 700 nm) and different waveguide widths (1000 nm to 2200 nm) respectively.

The schematic diagram of the dispersion measurement setup is shown in Figure A1. The microresonator transmission, from which quality factor and FSR values are determined, was measured using a tunable laser swept through its full wavelength tuning range at a tuning rate of 40 nm/s. For absolute wavelength calibration, 1% of the laser output was directed into a fiber coupled hydrogen cyanide gas cell (HCN-13-100, Wavelength References Inc.) and then into a photodetector ($PD_{Gascell}$). The microresonator and gas cell transmission were recorded during the laser sweep by a data acquisition system whose sample clock was derived from a photodetector (PD_{MZI}) monitoring the laser transmission through an unbalanced fiber Mach-Zehnder Interferometer (MZI). The MZI has a path length difference of approximately 40 m, making the measurement optical frequency sampling resolution 5 MHz. The absolute wavelength of each sweep was determined by fitting 51 absorption features present in the gas cell transmission to determine their subsample position, assigning them known traceable wavelengths [88] and calculating a linear fit in order to determine the full sweep wavelength information. Each resonance was fitted with a Lorentzian lineshape unless a cluster of resonances were deemed too close to achieve a conclusive fit with a single Lorentzian. Then, an N-Lorentzian fit was utilized where N is the number of resonances being fitted. The dispersion of the ring resonator was then determined by analyzing the wavelength dependence of the FSR.

To compare the dispersion measurements with the COMSOL calculations, we performed two other measurements beside the one shown in the comb measurement in Figure 3-7b. Figure 3-5a and b show the measured dispersions of the TE_{21} mode of the microresonator used in this paper (a ring width of 2 µm) and the TE_{11} mode of the microresonator with a different ring width of 1.55 µm, respectively. Both measurements show good agreements with the COMSOL calculations (D_{mea} = 2.2 MHz versus D_{sim} = 2.4 MHz, and D_{mea} = 330 kHz v.s. D_{sim} = 500 kHz). The good agreements give us confidence in the COMSOL calculations, and thus we use the calculated dispersions in the Kerr comb numerical simulation for the wavelength range not covered by the dispersion measurements (due to the unavailability of the suitable tunable laser).

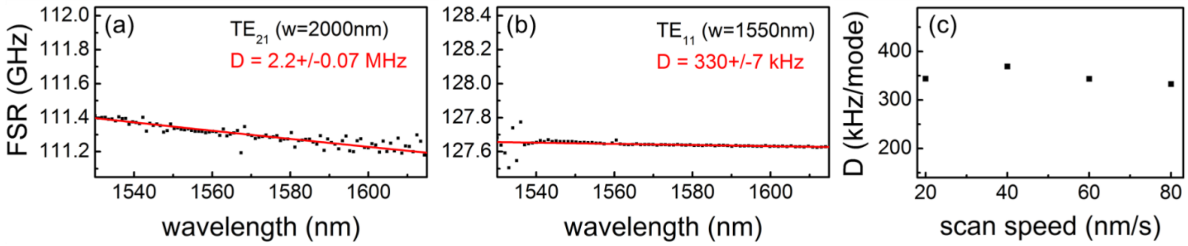

Figure 3-5. Measured dispersions by swept wavelength interferometry.

(a) Wavelength dependence of the FSR, measuring a non-equidistance of the modes, *D*, of 2.2 MHz, in a good agreement with the COMSOL simulations, *D* = 2.4 MHz. (b) Wavelength dependence of the FSR, measuring a non-equidistance of the modes, *D*, of 330 kHz, in a good agreement with the COMSOL simulations, *D* = 500 kHz. (c) Dispersion measured at different wavelength scan speeds, showing the minimal effect of the temperature drift when the wavelength scan speed is set higher than 20 nm/s.

It has been shown that the resonance shift due to the temperature drift is the major cause in the uncertainty of the dispersion measurements [89]. In our measurement setup, we actively control both the ambient and the on-chip temperature and the temperature drift in 2 second is measured to be less than 5 mK. Such a temperature drift will lead to a resonance shift that can be calculated by $\frac{\Delta\upsilon}{\upsilon_0} = -\left(\alpha + \frac{1}{n}\frac{dn}{dT}\right)\Delta T$, where the thermal expansion coefficient $\alpha = 3.3 \times 10^{-6}/K$ and the thermo-optic coefficient $\frac{dn}{dT} = 2.45 \times 10^{-5}/K$ [90,91]. Thus, the uncertainty of our dispersion measurement setup, limited by the temperature induced resonance shift, is estimated to be less than 175 kHz/mode. Experimentally, we observe measurement errors of less than ± 70 kHz/mode, in good agreement with the estimation. For each measurement, four datasets are taken and independently fit to find the dispersion. The reported *D*s are the average values and the measurement errors are the standard deviations of the four datasets. Furthermore, we also confirm the temperature drift has minimal effect when the wavelength scan speed is set higher than 20 nm/s (Figure 3-5c).

Note that, the non-equidistance of the modes in our ring resonator can be estimated as $D_2 = -270\,kHz$. Compared to the resonance linewidth, $2\gamma_0 = 180\,MHz$, the non-equidistance is insignificant and thus comb spacing alterations due to mode interaction are pronounced in our ring resonator [92]. The frequency shift Δ_a of mode a due to interaction with mode b can be estimated using the formula $\Delta_a = -\frac{\kappa^2}{\Delta}$, where κ is the interaction constant and $\Delta$is the difference in eigenfrequencies of the interacting modes (a and b) [92]. Even with an assumption of large Δ of 10 GHz, a small mode interaction constant $\kappa = 0.6\gamma_0$ can change the local dispersion from normal dispersion to anomalous dispersion. Similar effect was also observed and characterized in Ref. [93].

Figure 3-6 plots the resonance frequency offsets with respect to the fundamental mode family (top) as well as the wavelength-dependent FSRs of the fundamental mode family (bottom). The zero crossings on the upper panel represent the wavelengths where the fundamental mode family experiences mode crossings with other higher order mode families. The lower panel then shows that the disruption of the dispersion continuity of the fundamental mode family is dominated by the mode interaction with the first higher order TE mode family.

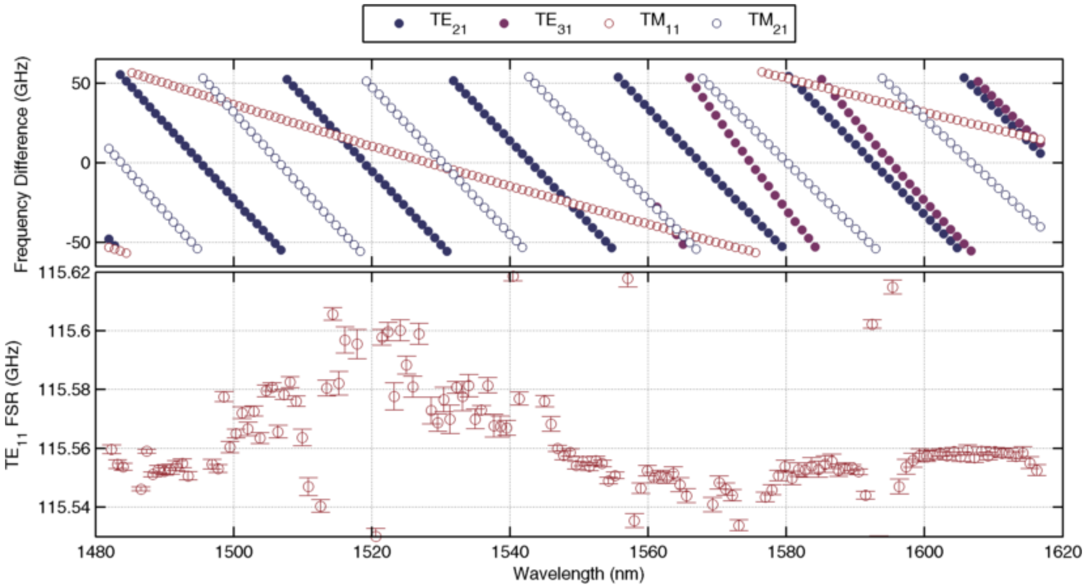

Figure 3-6. Frequency offset and FSR of the modal families.

Upper panel: The resonance frequency offsets with respect to the fundamental mode family. Lower panel: Wavelength-dependent FSRs of the fundamental mode family.

3.2. Globally-Normal GVD Mode-Locked Frequency Combs

The transmission of Si_3N_4 microring resonator under investigation is shown in Figure 3-7a. Five modal families (3 TE and 2 TM) are identified from the transmission and each Lorentzian resonance is fitted to determine its frequency and *Q*-factor as described in session 3.1.1. The frequency data is then used to evaluate the GVD. For the fundamental mode family, a loaded *Q*-factor of more than 10^6 is achieved at 1600 nm while the *Q*-factors at the telecommunications C-band wavelengths are more than 4× lower due to residual N-H absorption [94]. For the higher order mode families, *Q*-factors are orders of magnitude smaller and thus no Kerr comb is generated from these mode families. *Q*-factors are also reduced at longer than 1625 nm due to increasing coupling loss. Therefore, the resonator has a distinct spectrally restricted area characterized with the highest *Q*-factor. As discussed later, this feature is critical for the mode-locked pulse generation in our normal GVD microresonators. Figure 3-7b shows the measured fundamental mode dispersion of the ring resonator, in a good agreement with our numerical modeling using a full-vectorial finite-element mode solver. Across the whole L-band, the fundamental mode features a normal GVD with local disruptions induced by mode interaction with the higher-order modes. Such change of local GVD facilitates the start of the hyper-parametric oscillation from our microresonator. An example Kerr comb spectrum is shown in Figure 3-7c, with a spectral width spanning more than 200 nm. The optical spectrum shows a clean mode structure with comb lines separated by single free spectral range (FSR) of the fundamental mode family, without identifiable noise peaks between comb lines (Figure 3-3b, inset). We investigated the Kerr comb coherence by measuring the RF amplitude noise with a scan range much larger than the cavity linewidth and by performing a cw heterodyne beat note measurement [24,95]. Both measurements confirmed the coherence of the Kerr comb. The use of RF amplitude noise as a measure of low phase noise operation has been demonstrated and widely employed [24,77,95]. With proper change of the pump power and detuning (detailed in Figure 3-8), the Kerr comb is driven into the low phase noise regime as shown in Figure 3-7d. The cw heterodyne beat note measurements are shown in Figure 3-7e. Besides the beat note of the cw laser with the pump laser, beat notes between the cw laser and different comb lines are also measured. All beat notes exhibit the same linewidth of 800 kHz, limited by coherence between the cw laser and the pump laser. Neither additional linewidth broadening of the comb lines relative to the pump nor multiple beat notes were observed, confirming the comb lines exhibit a similar level of phase noise as the pump.

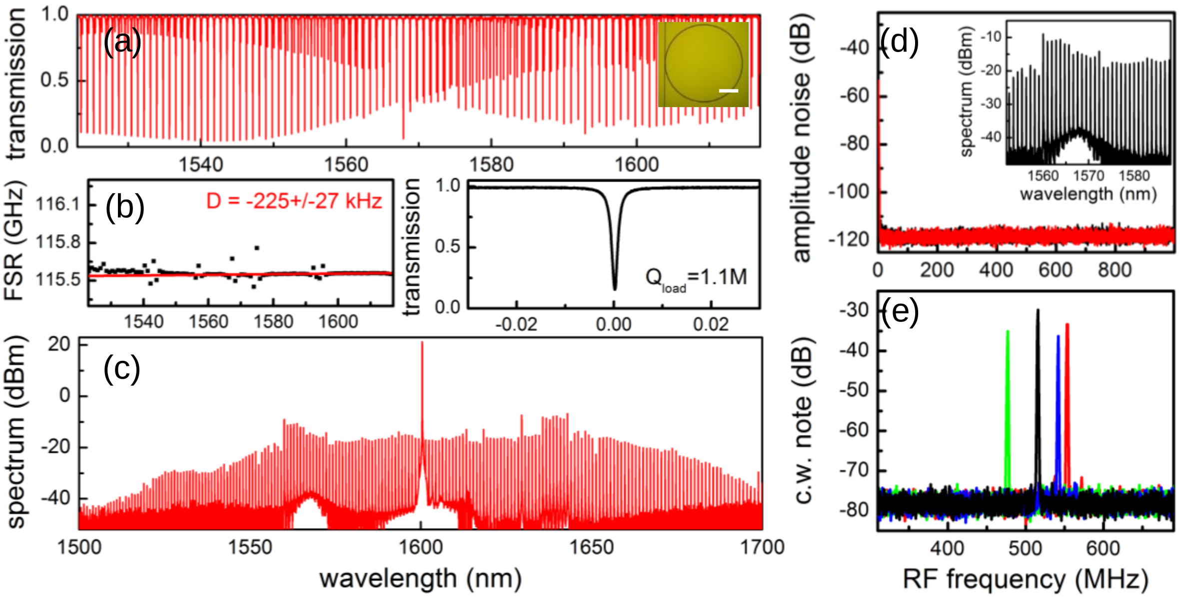

Figure 3-7. Microresonator frequency comb generation and characterization. (a) Transmission of the cavity modes. Inset: an optical micrograph of the ring resonator. Scale bar: 100µm. (b) Left: wavelength dependent FSR, measuring a non-equidistance of the modes, $D_2 \equiv -\beta_2 c\omega_{FSR}^2/n_0$, of -225kHz, in a good agreement with the simulation result from a full-vector finite-element mode solver, $D_2 = -270kHz$. Right: transmission of the cavity mode at the pump wavelength, measuring a quality factor of 1.1×10^6. (c) Example Kerr comb spectrum, with a spectral width spanning more than 200 nm. (d) RF amplitude noise of the Kerr comb (black curve) along with the detector background (red curve), indicating the low phase noise operation. Inset: a zoom-in plot of the optical spectrum, showing a clean comb structure. (e) cw heterodyne beat notes between a cw laser and different comb lines (black: pump; blue: 10th mode; red: 20th mode; green: 21st mode). No linewidth broadening of the comb lines relative to the pump is observed, showing the comb retains a similar level of phase noise as the cw laser.

Note that, the comb experiences several stages before driven into a coherent state. As we tune the pump wavelength further into resonance and more power is coupled into the microresonator, the bandwidth of the secondary comb families grows and the spectral overlap between them becomes more extensive, resulting in an increase of RF amplitude noise and merging of multiple RF spikes to form a continuous RF noise spectrum. Note that, a dedicated study on the dynamics of coherent state transition is detailed in **Error! Reference source not found.**. After sweeping the detuning and power levels to generate a broad comb spectrum, we next perform an abrupt discrete step-jump in both detuning and power to achieve the low phase noise state, and are able to find a set of parameters at which the RF amplitude noise drops by orders of magnitude and approaches the detector background noise (Figure 3-7d). The phase-locked comb typically stabilizes for more than three hours.

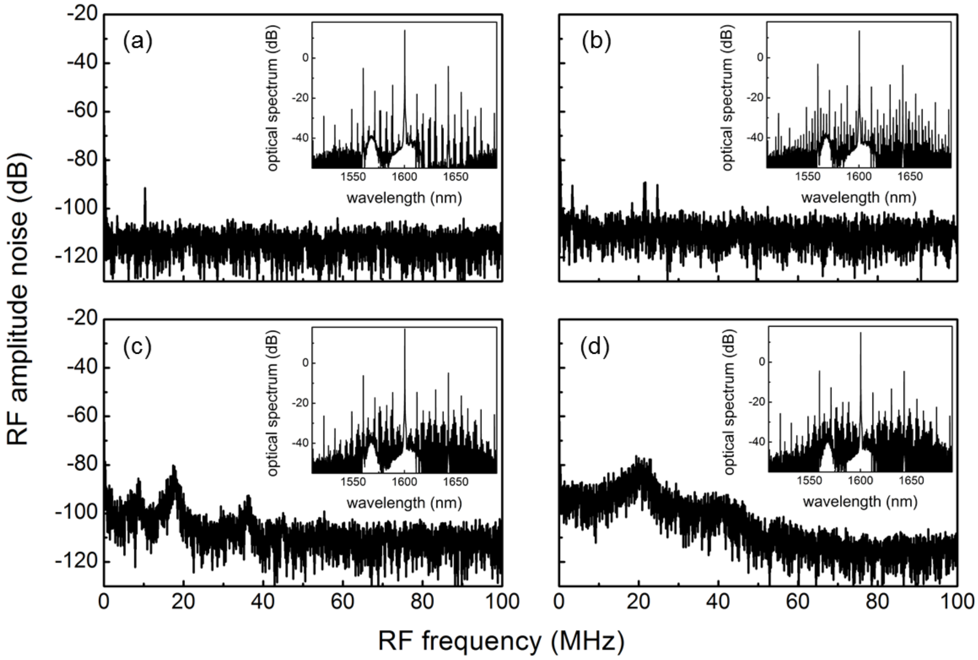

Figure 3-8. Normal dispersion Kerr comb evolution.

Growth of the RF amplitude noise and the comb spectrum (inset) are measured at four different pump detunings over a 30 pm range as the pump is tuned into the cavity resonance (from (a) to (d)).

3.3. Ultrashort Pulse Formation and Characterization

Hyper-parametric oscillation in an anomalous dispersion microresonator starts from the modulation instability of the intra-cavity cw light. When the intra-cavity power exceeds a certain threshold, the cw field becomes modulated and the modes of the resonator that is phase matched start to grow. Since most materials possess positive Kerr nonlinearities, anomalous GVD is tuned in prior resonators to satisfy the phase matching condition. Increase of the optical power can result in soliton formation, leading to the generation of a broad frequency comb and short pulses.

Hyper-parametric oscillation as well as Kerr comb formation is also possible in the case of normal GVD, but a non-zero initial condition is required for frequency comb and pulse generation [83]. In our microresonator, the comb can be ignited due to the change of local GVD resulting from the mode interaction between the fundamental mode family, which has a normal GVD, and the first higher order mode family, which has an anomalous GVD (see Figure 3-7b). Mode interaction enables excitation of the hyper-parametric oscillation from zero initial conditions. It is possible then to introduce a non-adiabatic change to the system parameters and transfer the system from the hyper-parametric oscillation regime to the frequency comb generation regime [83]. Here a non-adiabatic change means a stepwise change of resonance detuning or pump power, instead of a continuous scan, in a time shorter than the time of the comb growth, which is much longer compared to the cavity lifetime [83,96].

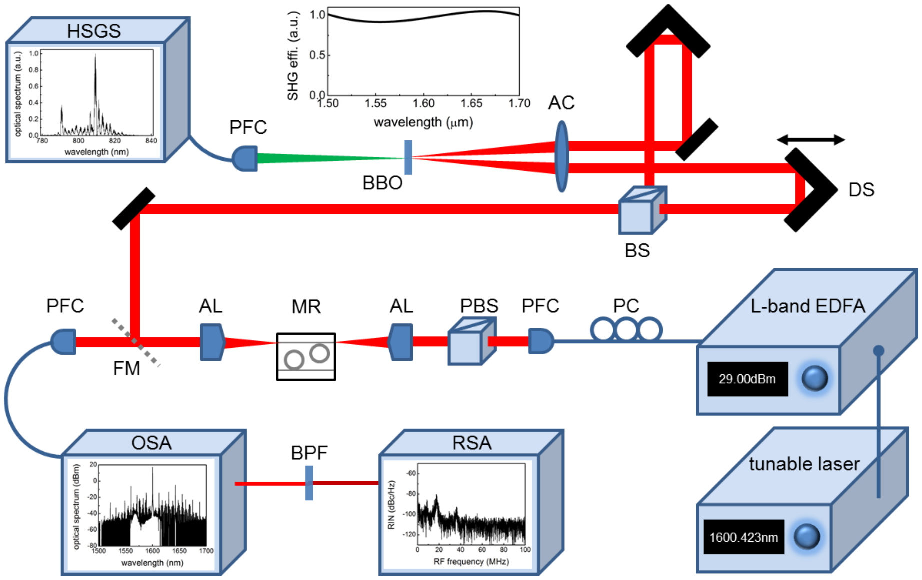

Figure 3-9. Comb characterization and FROG measurement setup.

PC, polarization controller; PFC, pigtailed fiber coupler; PBS, polarization beamsplitter; AL, aspheric lens; MR, micro-resonator; FM, flip mirror; OSA, optical spectrum analyzer; BPF, bandpass filter; RSA, RF spectrum analyzer; BS, beamsplitter; DS, delay stage; AC, achromatic lens; HSGS, high-sensitivity grating spectrometer; BBO, β-barium borate. BBO is chosen to be the second-harmonic generation crystal because it has been shown to exhibit ultrabroad phase matching bandwidth at the telecommunication wavelengths [97,98].

We measured the pulse duration via sub-femto-joule sensitive second-harmonic-generation (SHG) non-collinear frequency-resolved optical gating (FROG) [99,100] without involvement of any optical amplification nor external bandpass filtering, to minimize pulse distortion.

The schematic diagram of FROG setup is shown in Figure 3-9. The cw pump started from an external cavity stabilized tunable laser (Santec TSL-510C). The linewidth of the laser is 200 kHz and the frequency stability over an hour is <120MHz. The pump power was increased from 8dBm to 29 dBm in an L-band EDFA (Manlight HWT-EDFA-B-SC-L30-FC/APC). A 3-paddle fiber polarization controller and a polarization beam splitter cube were used to ensure the proper coupling of TE polarization into the microresonator. The total fiber-chip-fiber loss is 6 dB. The microresonator chip was mounted on a temperature controlled stage set to 60°C. The temperature stability over an hour is <0.1°C so that the change in coupling loss is negligible (<0.5%). The output light was sent to an optical spectrum analyzer (Advantest Q8384) and a photodiode (Thorlabs DET01CFC) connected to an RF spectrum analyzer (Agilent E4440A) for monitoring of comb spectrum and RF amplitude noise, respectively. For the RF amplitude noise measurement, a 10 nm portion of the optical spectrum (1560 nm to 1570 nm) was filtered from the comb. The output light can also be sent by a flip mirror to the FROG setup for pulse characterization. The FROG apparatus consists of a lab-built interferometer with a 1 mm thick β-BBO crystal and a high-sensitivity grating spectrometer with a cryogenically-cooled deep-depletion 1024×256 Si CCD array (Horiba Jobin Yvon CCD-1024×256-BIDD-1LS). The FROG setup is configured in a non-collinear geometry and careful checks were done before measurements to ensure only background-free SH signals were collected. The use of dispersive optics is minimized and no fiber is used in the FROG apparatus such that the additional dispersion introduced to the pulse is only -50 fs^2. The FROG can detect pulses with a bandwidth of >200 nm [101] and a pulse energy of <100 aJ (10 μW average power) with a 1 second exposure time. With the sensitive FROG, no additional optical bandpass filtering and amplification is needed (minimizing pulse distortion), though there is a small amount of dispersive filtering and intensity modification with the coupling optics and ring-waveguide coupling. The FROG reconstruction was done iteratively using genetic algorithm [102]. Genetic algorithm is a global search method based on ideas taken from evolution and is less susceptible to becoming trapped by local extrema in the search space. Both the spectral amplitudes and phases are encoded as strings of 8-bit chromosomes and two genetic operators, crossover and mutation, are used to generate the next-generation solutions. Tournament selection with elitism is employed to ensure monotonically convergence of the solution [103]. The FROG error is defined as $\varepsilon = \sqrt{\frac{1}{N^2}\sum_{i,j=1}^{N}|S_{mea}(\omega,t) - S_{ret}(\omega,t)|^2}$, where $S_{mea}(\omega,t)$ and $S_{ret}(\omega,t)$ are the measured and reconstructed spectrograms.

Careful checks were conducted to ensure no interferometric SH signal was collected in the FROG spectrogram [104]. Figure 3-10a is the spectrogram with 32 ps delay scan and it shows a pulse train with 8.7 ps period, the inverse of the fundamental mode family FSR (115.56 GHz). For better visualization, Figure 3-10a is plotted on log-scale and the bright cw pump component is removed in the plot. Spectral interferometric fringes are clearly visible for delays longer than the pulse duration. This interference arises due to the presence of the cw background as it can also mix with the pulse, generating two temporally-separated FROG signal pulses. The fringes become sparse as the delay approaches zero and the patterns depend on the relative phase between the cw pump and the pulse [105]. Figure 3-10b and c is the spectrogram measured with a finer time resolution, 4 fs, and Figure 3-10c is the reconstructed spectrogram with a FROG error of 2.7%. Due to the complexity of the pulses, an iterative genetic algorithm is developed specifically to retrieve the spectrograms. Figure 3-10d shows the retrieved pulse shape (red curve) and temporal phase profile (blue curve), with a 1.3 rad relative phase contrast observed within the pulse. The full-width-half-maximum (FWHM) pulse duration is measured at 74 fs, positively chirped from its transform-limited FWHM pulse duration of 55 fs. Due to the nature of the cw driven nonlinearity, the observed mode-locked pulse necessarily sits on a pedestal, analogous to a cavity soliton.

Figure 3-10e shows the measured optical intensity autocorrelation (AC) trace of the generated pulse train and the left panel of Figure 3-10f plots the zoom-in view. Of note, this is not an interferometric autocorrelation and thus the temporal fringes in the AC trace represent the actual oscillating structures of the pulse. Between the pulses, temporal fringes with a period of ~200 fs are clearly observed and these fringes arise from the presence of the primary comb lines, ~4.85 THz (42nd mode) away from the pump. In addition, the right panel of Figure 3-10f shows the calculated AC traces of a stable transform-limited pulse train (black curve) and an unstable pulse train (red curve). As the instability results in the significantly increased background level of the AC trace, it shows that the instability of the generated pulse train is minimal and provides another confirmation of the stable mode-locked pulse generation [106].

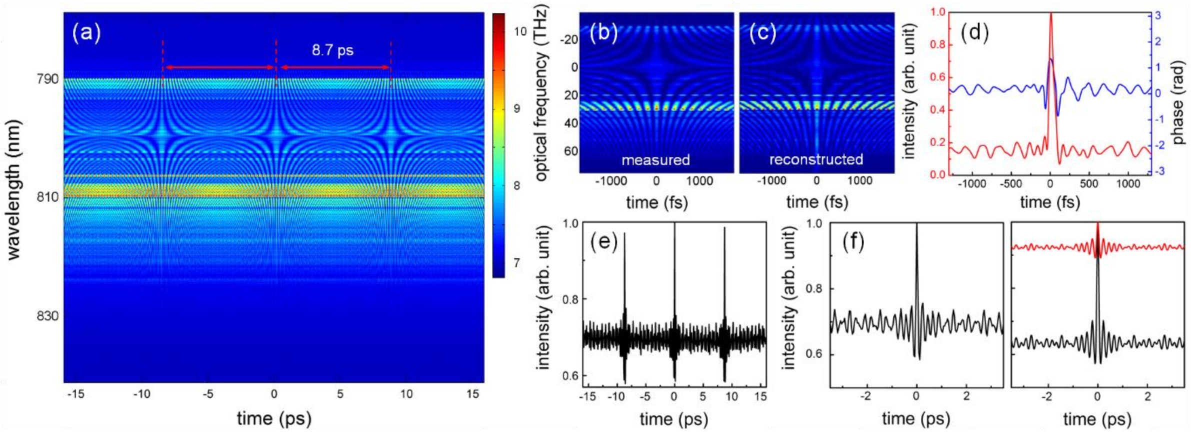

Figure 3-10. Pulse duration measured via sub-femto-joule sensitive second-harmonic-generation (SHG) non-collinear frequency-resolved optical gating (FROG).

(a) FROG spectrogram with a delay scan of 32 ps, showing a fundamentally mode-locked pulse train. (b) FROG spectrogram measured with a finer time resolution of 4 fs. (c) Reconstructed FROG spectrogram achieved by use of genetic algorithms. (d) Retrieved pulse shape (red curve) and temporal phase profile (blue curve), measuring a 74 fs FWHM pulse duration. (e) Measured AC of the generated fundamentally mode-locked pulse train. (f) Left:

a zoom-in plot of the measured AC. Right: the calculated ACs of a transform-limited stable pulse train (black curve) and an unstable pulse train showing a significantly larger AC background (red curve).

3.4. Numerical Simulation by Solving the Master Equation

To shed light on the pulse generation mechanism, we first performed numerical simulation solving the Lugiato-Lefever equation for 512 modes [30]. Experimentally-measured dispersion (Figure 3-7b) and wavelength-dependent Q values (Figure 3-2), including the local dispersion disruptions, are entered into the modeling.

In the simulation, we present the spectrum of the resonator as $2\pi\left(\nu_j - \nu_{j0}\right)/\gamma_0 = \nu_{FSR}(j - j_0) + \delta\nu_{j,j_0}$, where $\nu_j = \omega_j/2\pi$ is the linear frequency of the mode, $2\gamma_0$ is the FWHM of the pumped mode, ν_{FSR} is the dimensionless local averaged free spectral range of the resonator (in the simplest case of no mode interaction it is $2\nu_{FSR} = \left(\nu_{j_0+1} - \nu_{j_0-1}\right)/(\gamma_0/2\pi)$), and $\delta\nu_{j,j_0}$ is the dimensionless GVD parameter. For the microresonator used in this study, $\nu_{FSR} = 1283.965$ and $\gamma_0 = 2\pi \cdot 90MHz.$). Figure 3-11 plots the dimensionless GVD parameter as a function of mode number. In the simulation shown in Figure 3, the experimentally measured resonant frequencies, whenever possible, and Q-factors of the fundamental mode family are input directly into the model. For modes beyond our measurement capability, we assume the GVD is normal without higher order dispersions and local dispersion disruptions induced by modal interactions. Namely, $\delta\nu_{j,j_0} \cong -\frac{D_2}{2}(j - j_0)^2$. The procedure is justified by the good agreements between the COMSOL calculations and the dispersion measurements (Figure 3-7b, Figure 3-5a and Figure 3-5b) and the small TOD from the COMSOL calculation.

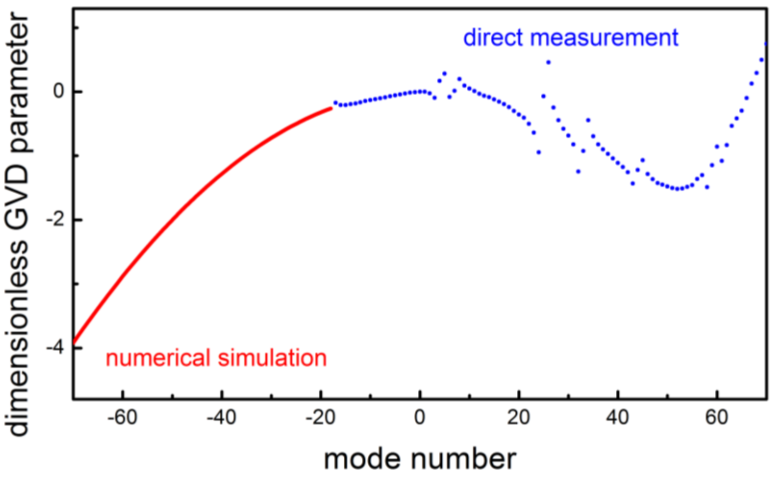

Figure 3-11. Dimensionless GVD parameters used in numerical modeling.

In the simulation shown in Figure 3-12, the experimentally measured resonant frequencies, whenever possible, and *Q*-factors of the fundamental mode family are input directly into the model (blue curve and datapoints). For wavelength range not covered by the measurement, we assume the GVD is normal without higher order dispersions and local dispersion disruptions induced by modal interactions (red curve).

Figure 3-12a shows the simulation results, illustrating the emergence of the first pairs of hyper-parametric oscillation sidebands around the ±42nd modes. A good agreement with the experimental emergence result (inset) is achieved. With the proper pump power and detuning, a fundamentally mode-locked pulse train is generated as shown in Figure 3-12b. The modeled FWHM pulse duration is 110 fs and the relative phase contrast is 1.7 rad (positively chirped), in good agreements with the FROG measurements.

We next numerically examined idealistic nonlinear microresonators characterized by solely normal GVDs and symmetric wavelength-dependent *Q* factors to elucidate the mode-locking physics. Figure 3-14 shows the case with larger D_2 of 0.03 (or -2.7 MHz) and without wavelength dependence in *Q* factors. A phase-locked Kerr comb can be generated, but the pulse duration is long and the shape complex. This is because, unlike in anomalous GVD microresonators, pulse broadening due to the normal GVD is not balanced by SPM and thus an additional mechanism has to be introduced to stabilize and shape the pulses. In Figure 3-15, we numerically introduce wavelength-dependent *Q*-factors, effectively a bandpass filter, and then clean mode-locked pulses are generated from the microresonator. These are dark pulses and the exact pulse shapes depend on the bandpass filter bandwidth. Next, when D_2 is numerically set smaller at 0.003 (and closer to the experimental value), bright pulses can also be observed. Different from the case of large normal dispersion where only dark pulses exist, both bright and dark pulses are possible in the small normal dispersion case, depending on the exact combination of dispersion and bandpass filter bandwidth (Figure 3-16). Experimentally, the mode-mismatched coupling also plays a role in changing the pulse shape as the imperfect coupling [107] acts as an external filtering. A microresonator with add-drop ports will serve as a better platform for further investigation on the dark solitons [108].

It is even possible to generate square pulses directly with the correct sets of *Q*-factor profile, GVD, and detuning (Figure 3-12c). We note that the mode-locking mechanism has analogies, but is not identical, to the pulse generation mechanism in all-normal dispersion fiber lasers [109], a variant of additive pulse mode-locking [110]. We further verify that the temporal fringes of the pulse come from the strong primary comb lines as shown in Figure 3-13.

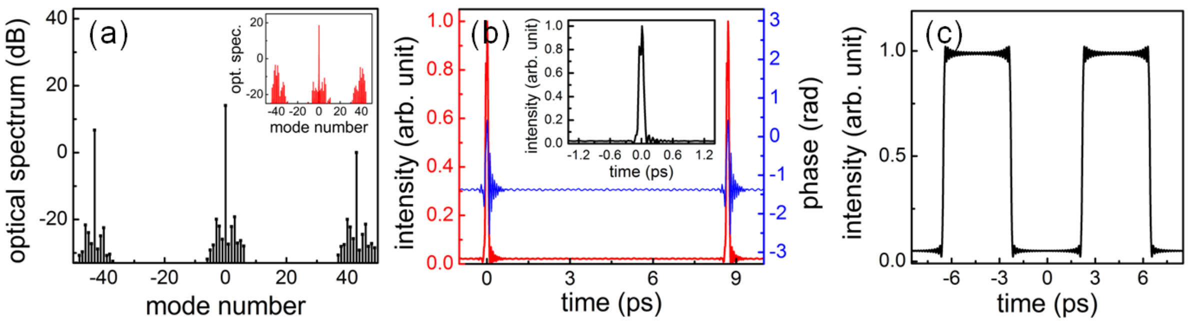

Figure 3-12. Numerically modeled frequency comb by solving the Lugiato-Lefever equation.

(a) Near the threshold and with a small red-detuning of 180 MHz, the first pairs of hyper-parametric oscillation sidebands emerge at around the ± 42nd modes, showing a good agreement with the experimental result (inset). (b) With the proper pump power (260 mW) and red-detuning (2.5 GHz), a mode-locked pulse train is generated. The red and blue curves are the modeled pulse shape and the temporal phase profile, respectively. Inset: a zoom-in plot of the pulse shape, showing an ultrashort FWHM pulse duration of 110 fs. (c) Square optical pulses can also be generated directly from a normal GVD microresonator. The conditions for the observation of these square pulses are $D_2 = 0.002$, red-detuning of $7.7\gamma_0$, resonance linewidth of $\gamma_j = \gamma_{j0}[1 + 0.01(j - j_0)^2]$ and pump power 25 times larger than the threshold.

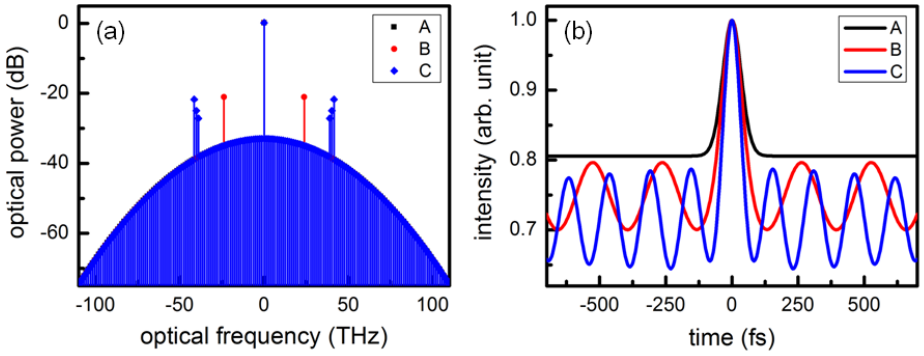

Figure 3-13. Temporal fringes resulting from the primary comb lines.

Without the primary comb lines (A), the AC trace shows no temporal fringes. When the primary comb lines are present (B,C), temporal fringes with a period matching the separation of the primary comb lines are clearly observed.

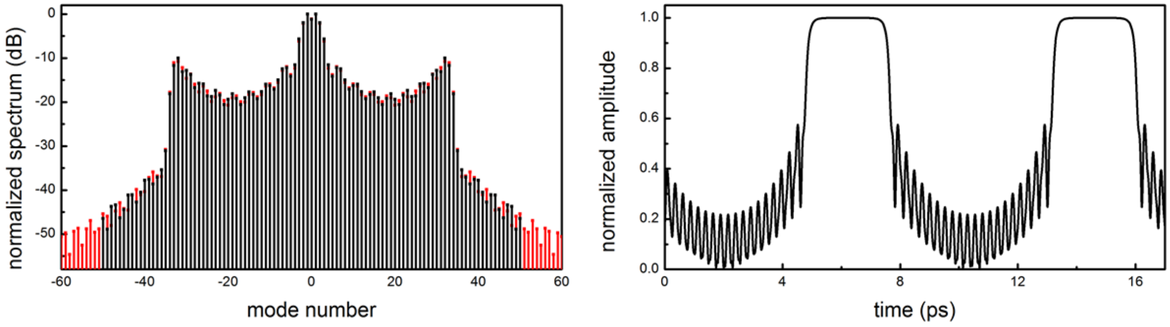

Figure 3-14. Kerr comb generated in a microresonator characterized by a large normal GVD and a wavelength independent Q-factors.

In this simulation, we assume the microresonator has no higher-order dispersions and its GVD is characterized by $D_2 = 0.03$. Furthermore, the Q-factor is assumed to be a constant across the whole wavelength range. The pump power is 49 times larger than the threshold and the resonance red-detuning is $17.4\gamma_0$.

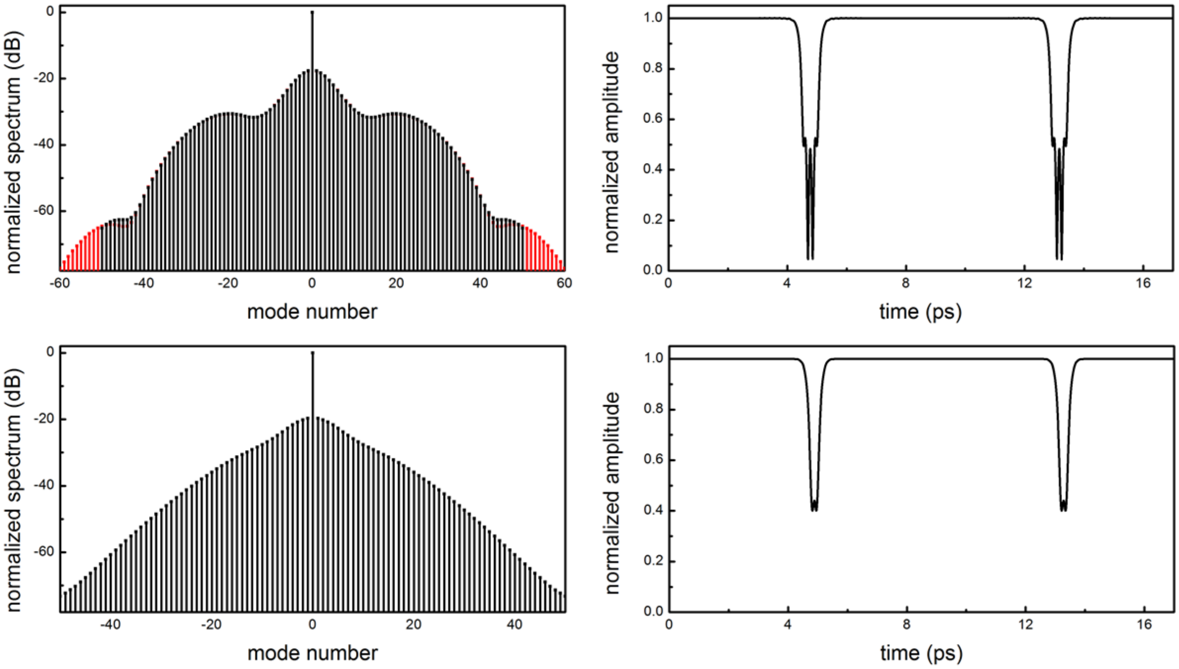

Figure 3-15. Kerr comb generated in a microresonator characterized by a large normal GVD and a wavelength dependent Q-factors.

Different from Figure 3-14, here we assume the microresonator has a wavelength-dependent Q-factor and its resonance linewidth is in the forms of $\gamma_j = \gamma_{j0}[1 + 0.003(j - j_0)^2]$ (top) and $\gamma_j = \gamma_{j0}[1 + 0.01(j - j_0)^2]$ (bottom). The resonance red-detuning is $14.2\gamma_0$ and $11.5\gamma_0$, respectively.

To characterize the numerical artifact due to limited number of modes taken into consideration, we repeated the simulations for 121 modes. We observed that the solution (comb spectra, pulse width and shape) only has a relatively weak dependence on the number of modes when the modes are more than 100 in the simulations. Furthermore, the artifact was mainly observed on the spectral wings. For the modes close to the carrier, the comb line intensities vary only by roughly 1% between simulations with 101 and 121 modes.

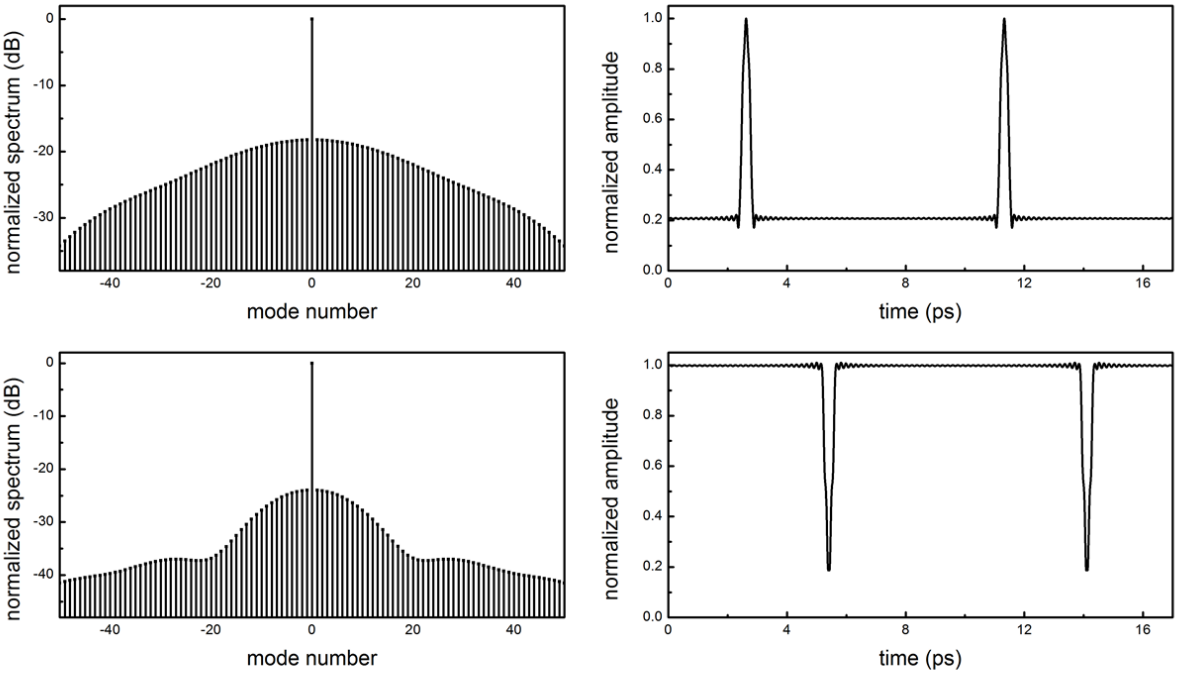

Figure 3-16. Kerr comb generated in a microresonator characterized by a small normal GVD and a wavelength dependent Q-factors.

For microresonators possessing a small normal GVD, both bright pulse (top) and dark pulse (bottom) can be generated. For the bright pulse generation shown here, $D_2 = 0.003$ and $\gamma_j = \gamma_{j0}[1 + 0.003(j - j_0)^2]$. The pump power is 49 times larger than the threshold and the resonance red-detuning is $10\gamma_0$. For the dark pulse generation shown here, $D_2 = 0.002$ and $\gamma_j = \gamma_{j0}[1 + 0.001(j - j_0)^2]$. The pump power is 25 times larger than the threshold and the resonance red-detuning is $7.2\gamma_0$.

There exist multiple other solutions besides the fundamentally mode locked frequency combs generating short pulses. Dynamical solutions, such as breathers, are available. Multi-pulse regimes are feasible. Sometimes multiple pulses overlap, creating unexpected pulse shapes. For example, it is possible to generate square pulses directly out of the microresonator (Figure 3-12c). The simulation shows that tuning the profile of the Q-factors as well as the

GVD is a powerful way to significantly increase the capability of these microresonators to generate arbitrary optical pulse shape.

3.5. Examination of The Spectral Filtering Effect on Mode-Locked State

To experimentally examine the effect of wavelength-dependent *Q*-factors, we then re-annealed the same microresonator at 1200ºC to reduce the absorption in the shorter wavelengths such that the *Q* roll-off is less pronounced (Figure 3-2). Figure 3-17a shows the Kerr comb generated from the re-annealed microresonator, showing a smoother and broader spectrum than the one shown in Figure 1c. Similarly, the comb can be driven into a low phase noise state (Figure 3-17b). However, now without the effective narrow bandpass filter, mode-locked pulses are not observed as evidenced by the high background level (≈ 0.85) in the AC trace. A phase stable state without mode-locking is also observed in another recent study using a different microresonator platform [111].

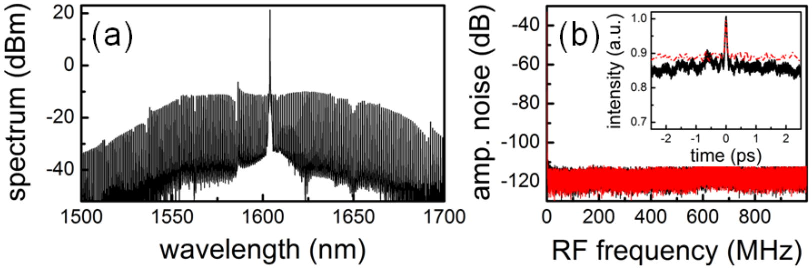

Figure 3-17. Examination of spectral filtering effect.

(a) Example Kerr comb spectrum from the re-annealed microresonator, showing a smoother and broader spectrum. (b) RF amplitude noise of the Kerr comb (black curve) along with the detector background (red curve). While the Kerr comb can also be driven to a low phase noise state, the high background level of the AC trace (inset) indicates the absence of mode-locked pulses. The red dashed line is the calculated AC trace assuming random spectral phases.

3.6. Closed-Form Solution of The Master Equation

Furthermore, we seek the closed-form solution of the master equation for the Kerr comb and pulse generation:

$$T_R \frac{\partial}{\partial T} A + \frac{i}{2}\left(\beta_{2\Sigma} + i\frac{T_c}{\Omega_f^2}\right)\frac{\partial^2}{\partial t^2} A - i\gamma|A|^2 A = -\left(\alpha + \frac{T_c}{2} + i\delta_0\right) A + i\sqrt{T_c P_{in}} e^{i\varphi_{in}} \tag{3-1}$$

where $A(T, t)$ is the electric field envelope in the microresonator, T_R the cavity roundtrip time, t the retarded time, T the slow time of the cavity, $\beta_{2\Sigma}$ the cavity GVD, T_c the power coupling loss per roundtrip, Ω_f the spectral characteristics of the coupling, γ the nonlinear coefficient, α the amplitude attenuation per roundtrip, δ_0 the resonance detuning, and $\sqrt{P_{in}} e^{i\varphi_{in}}$ the cw pump. Here, for simplicity, we assume the intracavity bandpass filter results solely from wavelength-dependent coupling loss: $T_{coupling} \approx T_c\left[1 + \frac{(\omega_c - \omega)^2}{\Omega_f^2}\right]$, where ω_c is the frequency for maximal coupling.

Assuming Gaussian input pulse and applying the variational method [112],

$$\begin{cases} A(T, t) = A_c + A_p(T, t) \\ A_c = \sqrt{P_c} e^{i\varphi_c} \\ A_p(T, t) = \sqrt{\frac{P_p}{\sqrt{\pi}}}\left[exp\left(\frac{t}{\sqrt{2}\tau}\right)^2\right]^{-1-iq} e^{i\varphi_p} \end{cases} \tag{3-2}$$

where P_c is the power of the cw background, φ_c is the phase of the background wave, P_p is the pulse peak power ($E_p = P_p\tau$ is the pulse energy), q is the chirp, τ is the pulse duration, and φ_p is the phase of the pulse.

Substituting Eq. (3-2) into Eq. (3-1) and assuming that the pulse energy is much lower than the cw energy but the pulse peak power is much higher than the DC background ($P_c T_R / P_p \tau \gg 1$ and $P_p / P_c \gg 1$), we can get the equation describing the cw background as

$$\sqrt{P_c}\left(\alpha + \frac{T_c}{2} + i\delta_0 - i\gamma P_c\right) = i\sqrt{T_c P_{in}}\, e^{i(\varphi_{in} - \varphi_c)}$$

(3-3)

and the approximate solution is

$$\begin{cases} \varphi_{in} - \varphi_c \cong \dfrac{\alpha + T_c/c}{\delta_0} \\ P_c \cong \dfrac{T_c P_{in}}{\delta_0^2}\left(1 + \dfrac{2T_c \gamma P_{in}}{\delta_0^3}\right) \end{cases}$$

(3-4)

On the other hand, the time-dependent part of Eq. (3-1) can be written as

$$\begin{cases} T_R \dfrac{\partial}{\partial T} A_p + \dfrac{i}{2}\beta_{2\Sigma}\dfrac{\partial^2}{\partial t^2} A_p - i\gamma\left|A_p\right|^2 A_p = R(T,t) \\ R(T,t) = \dfrac{T_c}{2\Omega_f^2}\dfrac{\partial^2}{\partial t^2} A_p - \left(\alpha + \dfrac{T_c}{2} + i\delta_0\right) A_p + \\ \qquad i\left[\gamma\left(\left|A_c + A_p\right|^2 (A_c + A_p) - \left|A_p\right|^2 A_p\right) - \dfrac{\gamma}{T_R}\displaystyle\int_{-T_R/2}^{T_R/2} A|A|^2 dt\right] \end{cases}$$

(3-5)

To describe the behavior of the pulse generated in the resonator we have to find values of four parameters: P_p, φ_p, q, and τ. The parameters are connected by a set of self-consistent equations which can be found using variational approach [112]. We introduce the Lagrangian density $\mathcal{L} = \frac{T_R}{2}\left(A_p^* \frac{\partial A_p}{\partial T} - A_p \frac{\partial A_p^*}{\partial T}\right) - \frac{i}{2}\left(\beta_{2\Sigma}\left|\frac{\partial}{\partial t} A_p\right|^2 + \gamma\left|A_p\right|^4\right)$ and the variation of the Lagrangian density results in the unperturbed nonlinear Schrödinger equation

$$\frac{\delta\mathcal{L}}{\delta A^*} = \frac{\partial\mathcal{L}}{\partial A^*} - \frac{\partial}{\partial T}\frac{\partial\mathcal{L}}{\partial(\partial A^*/\partial T)} - \frac{\partial}{\partial t}\frac{\partial\mathcal{L}}{\partial(\partial A^*/\partial T)} =$$

$$T_R \frac{\partial}{\partial T} A_p + \frac{i}{2}\beta_{2\Sigma}\frac{\partial^2}{\partial t^2} A_p - i\gamma\left|A_p\right|^2 A_p = 0$$

(3-6)

Taking into account that A does not depend on T directly, we write

$$\frac{\partial}{\partial T}A_p = \frac{\partial A_p}{\partial P_p}\frac{\partial P_p}{\partial T} + \frac{\partial A_p}{\partial \varphi_p}\frac{\partial \varphi_p}{\partial T} + \frac{\partial A_p}{\partial q}\frac{\partial q}{\partial T} + \frac{\partial A_p}{\partial \tau}\frac{\partial \tau}{\partial T}$$

(3-7)

From Eqs. (3-2), (3-6) and (3-7), we can write the Lagrangian of the system and the Lagrangian equations as

$$\begin{aligned} L = -i\frac{\beta_{2\Sigma}P_p}{4\tau}(1+q^2) - \frac{i}{2\sqrt{2\pi}}\gamma P_p^2\tau + \\ \frac{i}{4}P_pT_R\left[2q\frac{\partial \tau}{\partial T} - \tau\left(\frac{\partial q}{\partial T} - 4\frac{\partial \varphi_p}{\partial T}\right)\right] \end{aligned}$$

(3-8)

$$\frac{d}{dT}\left(\frac{\partial L}{\partial \dot{r}_j}\right) - \frac{\partial L}{\partial r_j} = \int_{-\infty}^{\infty}\left(R^*\frac{\partial A_p}{\partial r_j} - R\frac{\partial A_p^*}{\partial r_j}\right)dt$$

(3-9)

where $\dot{r}_j = \{\partial P_p/\partial T\,, \partial \varphi_p/\partial T\,, \partial q/\partial T\,, \partial \tau/\partial T\}$ and $r_j = \{P_p, \varphi_p, q, \tau\}$.

Again, under the assumption that the pulse energy is much lower than the cw energy but the pulse peak power is much higher than the DC background ($P_cT_R/P_p\tau \gg 1$and $P_p/P_c \gg 1$), we can get the equations describing the Gaussian pulse as

$$\begin{cases} T_R\dfrac{dE_p}{dT} = -E_p\left[T_c + 2\alpha + T_c\dfrac{1+q^2}{2\Omega_f^2\tau^2} + \right. \\ \qquad \left. \dfrac{2\sqrt{2}}{\left(\pi(9+q^2)\right)^{1/4}}\gamma\sqrt{P_pP_c}sin\left(\varphi_c - \varphi_p - \varphi_q\right)\right] \\ T_R\dfrac{d\varphi_p}{dT} = \dfrac{\beta_{2\Sigma}}{2\tau^2} + \dfrac{5}{4\sqrt{2\pi}}\gamma P_p - \delta_0 - \dfrac{qT_c}{2\Omega_f^2\tau^2} \\ T_R\dfrac{dq}{dT} = -\dfrac{T_R}{E_p}q\dfrac{dE_p}{dT} + \dfrac{\beta_{2\Sigma}}{\tau^2}(1+q^2) + \dfrac{1}{\sqrt{2\pi}}\gamma P_p - \left(T_c + 2\alpha + \dfrac{3}{2}T_c\dfrac{1+q^2}{\Omega_f^2\tau^2}\right)q \\ T_R\dfrac{d\tau}{dT} = -\dfrac{T_R}{2E_p}\tau^2\dfrac{dE_p}{dT} + \beta_{2\Sigma}q - T_c\dfrac{3q^2-1}{4\Omega_f^2} - \dfrac{\tau^2}{2}(T_c + 2\alpha) \\ \sqrt{3 - iq} = (9+q^2)^{1/4}e^{i\varphi_q} \end{cases}$$

(3-10)

Further assuming that $q^2 \gg \Omega_f^2\tau^2 \gg 1$, we finally reach the approximate solution

$$\boldsymbol{E_p \approx \frac{8\sqrt{10\pi}}{15}\frac{\beta_{2\Sigma}^{\frac{3}{2}}\Omega_f^2\sqrt{\delta_0}}{T_c\gamma}}$$

(3-11)

$$\boldsymbol{\tau \approx \frac{2\sqrt{5}}{3}\frac{\beta_{2\Sigma}^{\frac{3}{2}}\Omega_f^2}{T_c\sqrt{\delta_0}}}$$

(3-12)

$$\boldsymbol{q \approx \frac{4\beta_{2\Sigma}\Omega_f^2}{3T_C}}$$

(3-13)

$$sin(\varphi_c - \varphi_p - \varphi_q) \cong -\frac{9}{64\sqrt{5}}\frac{(1+q^2)\big(2(9+q^2)\big)^{1/4}T_c^3\sqrt{\delta_0}}{\beta_{2\Sigma}^3\Omega_f^6\sqrt{\gamma P_c}}$$

(3-14)

By fitting the measured *Q*-factor (Figure 3-2) of the ±20 modes around *Q*$_{max}$ with the wavelength-dependent coupling loss profile defined above, a filter bandwidth of 2.3 THz is found. A chirp q of 1.6 is then obtained after the filter bandwidth and the other measured parameters ($T_c = 0.003, \beta_{2\Sigma} = 17.14\, fs^2$) are entered into equation (3-13). This chirp is close to that obtained from the FROG measurement ($q = 1.5$), and the resulting calculated FWHM pulse duration (98 fs) is close to our measurements.

While the total power in the microresonator reduces as the pump detuning gets larger, equations (3-11) and (3-12) show the pulse energy actually increases and the pulse duration gets shorter. Overall, the pulse quality improves. It illustrates the active role of pump detuning: it is not simply a parameter that controls the coupled power in the microresonator, but an important physical factor that determines the pulse duration and energy distribution between the pulse and cw background. Furthermore, the closed-form solutions show that the pulse generated from a normal GVD microresonator is always chirped [equation (3-13)], and a narrower bandpass filter is necessary to keep the pulse short when the dispersion increases.

3.7. Summary

In this chapter, we discuss the generation of mode-locked pulses from on-chip normal dispersion microresonator, supported by phase noise characterization, FROG pulse measurement, and numerical modeling with exact experimental parameters. The excitation of the hyper-parametric oscillation is facilitated by the local dispersion disruptions induced by mode interactions. Then the system is driven from the hyper-parametric oscillation to the mode-locked pulse generation by a proper change of the pump power and detuning. The phase retrieval from the FROG measurement reveals a 74 fs fundamentally mode-locked pulse sitting on a cw background. Numerical modeling of the cw-driven nonlinear microresonator, capturing the full spectra with the measured GVD and *Q*s, confirms the feasibility of mode-locked pulse generation and agrees with our measurements. We show, both experimentally and numerically, the importance of pump detuning and effective bandpass filtering in stabilizing and shaping the pulses generated from normal GVD microresonators. Finally, we present the closed-form solution of the master equation under appropriate approximations, facilitating the design of mode-locked pulse generation from microresonators.

Chapter 4.

Optical Frequency Synthesis with Bichromatically-Pumped Coherent Kerr Frequency Comb

4.1. Introduction

Chip-scale frequency combs attract significant interests in a broad range of fundamental sciences and applications. A frequency comb links the frequency stability from microwave to optical spectral range, serving as a frequency gear for precision frequency synthesis and clockwork. Enabled by advances in frequency stabilization techniques, a real frequency comb can be achieved by phase-locking its spectrum to optical or microwave references. Based on these theories and techniques, frequency combs generated from a bichromatic pump has become an intriguing topic, advantaging on the additional control field with the threshold-less operation as frequency comb generation, and the possibility to achieve digitalized tuning of an optical frequency synthesizer. We here report our study of the coherent comb formation by introducing a low-power (10% of pump power) on-resonance seeding. Assisted by this artificially introduced seed pump, we detail the observation of comb transitions from incoherent to coherent state and the dynamics of self-injection locking between different comb families. A locked range of 40 MHz is achieved in the ~ 230 GHz carrier, leading to deterministically controlled comb repetition rates by the seeding laser detuning. The frequency stability measurement proves that the seeding pump does not introduce additional noise to the system. The work paves the way towards all-optical tunable comb oscillator for chip-scale RF-optical clockwork.

4.2. Experimental Design

The comb formation with a bichromatic pump is schematically shown in Figure 4-1, where the bichromatic pump consists of a pump laser and a seeding laser. Both lasers can be phase-locked to the reference fiber frequency comb (Menlo System FC1500-250-WG Optical Frequency Comb, referred as Menlo comb, same below) by a servo controller (Newport LB1005) respectively as shown in Figure 4-2b. Turing pattern state is chosen owing to its pristine structure without triggering sub-comb formation [33], as schematically shown in Figure 4-2a. Such a comb state maintains a clean structure with the comb spacing of 4 free-spectral-ranges (FSRs) without triggering the sub-comb modes.

After the spontaneous comb is generated with the pump laser only (dark blue lines in Figure 4-2a), we lock the pump laser to a Menlo comb mode, resulting a fixed beat note of *fp*; then we inject the seeding laser around 2-FSR away from the pump, such that a new family of comb lines (red lines) are generated, where two separated comb lines (dark blue solid line and red dashed line) may exist in the same resonance. We detune the seeding by tuning the microwave synthesizer employed to lock the seeding laser in order to examine the dynamics as discussed below. In this method, the coherence of bichromatic pump maintains in the detuning process.

The two lasers employed are Santec TSL-510 and New Focus Velocity 6730, where the former serve as the pump and latter the seeding. The instantaneous linewidth of the two lasers (Gaussian fitted ~ 370 kHz and instrument limited 6 Hz, respectively) after stabilization are shown in Figure 4-2a. In this study, the seeding power is chosen to be 10% compared to the pump; and when the detuning changes, the power of the seeding laser is slightly adjusted to maintain the output seeding power level after the amplifier.

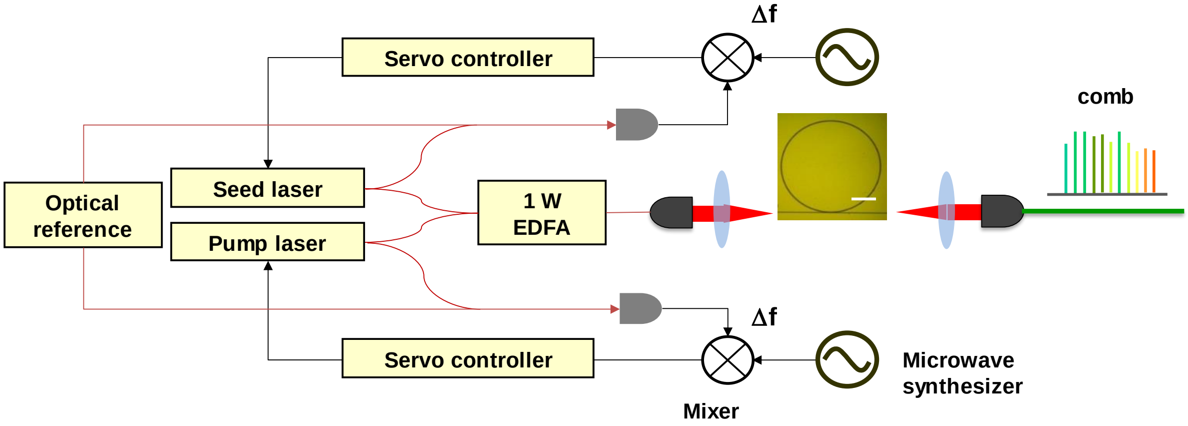

Figure 4-1. Experimental scheme for coherent comb generations via bichromatic pump. Both the pump and seed laser are locked to optical reference (Menlo comb). Inset: microscopc image of the microring resonator, scale bar 100 µm.

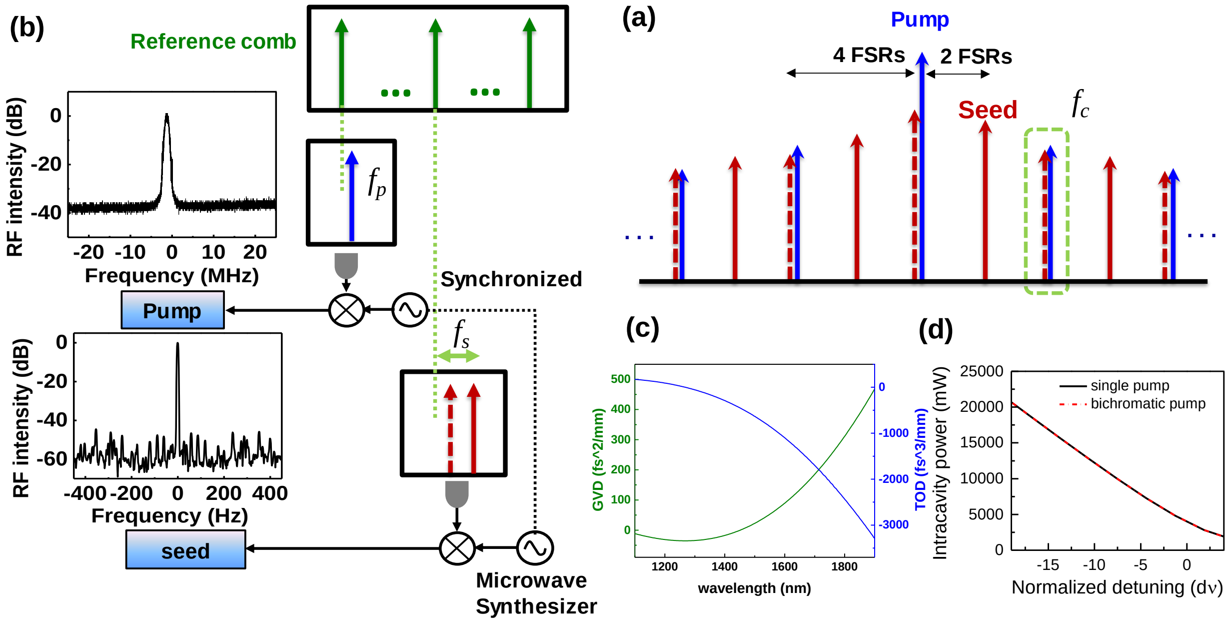

Figure 4-2. Comb states chosen and approach to realize bichromatic pump.

(a) A Turing pattern comb with 4 free-spectral-ranges (FSRs) is chosen for the observation, where the seed laser will be injected spaced with 2 FSRs from the pump (2^{nd} azimuthal mode).

(b) Scheme for tuning the seed laser by a microwave synthesizer. After the comb in (a) generated (blue), the pump laser is phase locked to Menlo comb, while the seed is injected to the 2nd azimuthal mode and phase locked to Menlo comb too. The detuning of the seeding is adjusted by the microwave synthesizer used for the phase locking. (c) The dispersion profile simulated by COMSOL module, featuring with high third-order dispersion (TOD) for maintaining a Turing comb. (d) Thermal load examination under single pump (black solid line) and bichromatic pump (red dashed line), where the seed laser is 2 FSRs spaced with the major pump.

4.3. Noise States Transition and Dynamics Of Injection Locking

As the seeding goes from blue side to red side of the resonance, the RF tone firstly decreases and then clamps to zero in a certain range, then increases at the red detuning side. At detuning of Δ_2, the full comb is in coherent states, as shown in Figure 4-3. Self-injection locking is the fundamental mechanism that drives the Kerr frequency comb into a coherent state. In this bichromatically-pumped comb, there are two comb families (I) generated from spontaneous four-wave-mixing (FWM) from the pump, i.e. the primarily comb lines; (II) generated from stimulated FWM between (I) and the seeding, i.e. the red dashed lines. The comb will be driven to a new coherent state when (I) and (II) commensurate. Hence by monitoring the offset of two comb lines in the same resonance where the primary comb line is generated (orange dashed box), one can observe this dynamical transitions of noise states. Figure 4-4a shows the offset measurement by changing the seeding detuning, where at the certain detuning range of ~ 40 MHz, the offset between the two comb lines turns to zero, indicating the two lines get injection-locked [113], i.e. the whole comb is driven to a new coherent state with 2-FSR comb spacing.

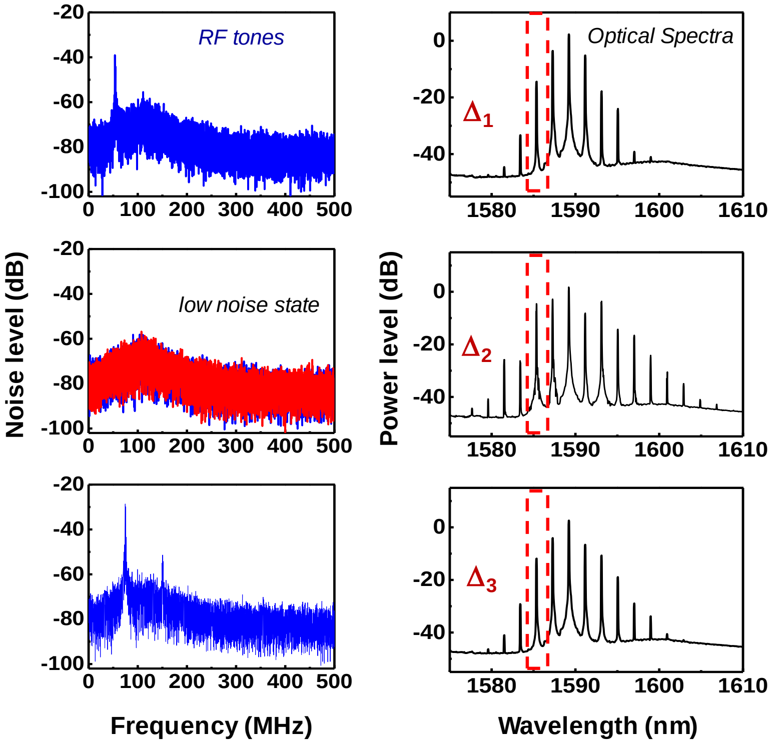

Figure 4-3. Examples of optical spectra and corresponding radio-frequency noise when adjusting the detunings (Δ_1, Δ_2 and Δ_3) of the seed laser.

As the seeding goes from blue side to red side of the resonance, the RF tone firstly decreases and then clamps to zero in a certain range, then increases at the red detuning side. At detuning of Δ_2, the full comb is in coherent states.

4.4. Coherent Comb with Controllable Repetition Rates

To further demonstrate the coherent state, we conduct the equidistance measurement. By adjusting the repetition rate of Menlo comb, we make sure that the pump, seeding and the monitored comb mode sit on the same side of the closet Menlo comb modes (with a beat note from 0 to 125 MHz) [16,20]. In theory *fp*, *fs* and *fc* satisfy the relation $(f_c - f_p)/(f_s - f_p) = 2 + \varepsilon$. As *fp* is fixed and *fs* is detuned by the synthesizer, stability of *fc* is a measure of the equidistance. A fitted slope of ~ 2 indicates the state being examined is a coherent state and that the repetition rate of the comb is effectively controlled by the seeding detuning. The Allan deviation for one detuning at different integration times is plotted in Figure 4-5 by comparison with that of the pump. The close levels between the pump and the monitored comb show that the coherence of the newly generated comb is only limited by the pump source.

Note that it is hard to tune the seeding through microwave synthesizer by more than 100 MHz directly, due to the limited range of receiving signal for laser diode current modulation. We overcome it through adjusting the locking point in the servo controller when the control signal reaches the limit, such that the *fs* can be continuously tuned. The absolute value of *fs* hence changes in each adjustment, and is normalized to starting frequency in the analysis.

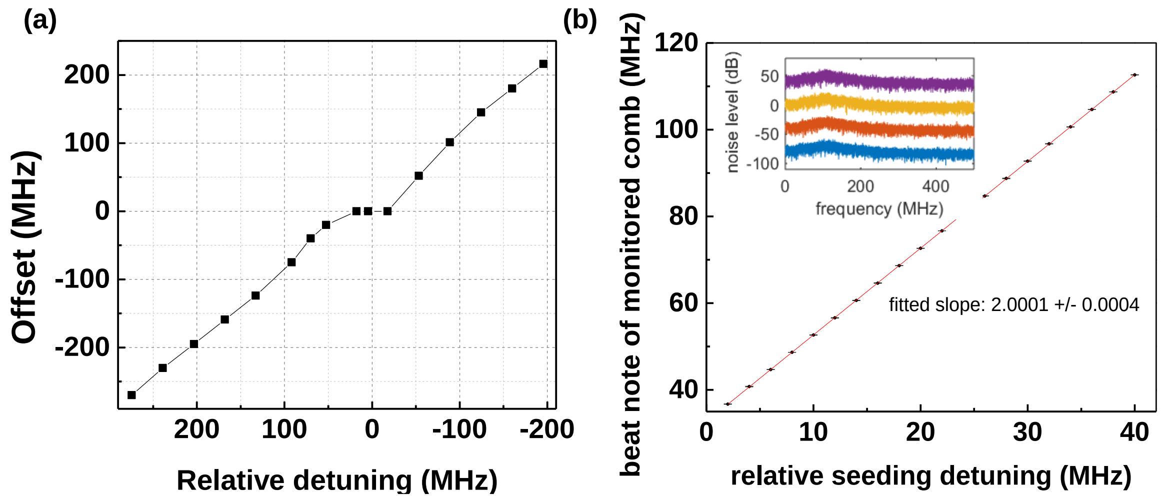

Figure 4-4. Observation of self-injection locking regime and controllable comb spacing by the seeding through a microwave frequency.

(a) A self-injection locking range of 40 MHz is observed in the 230 GHz comb. (b) The measured comb spacing changes versus the microwave frequency used for frequency synthesis. A fitted slope of 2 indicates that the new comb spacing follows with the microwave frequency synthesizer.

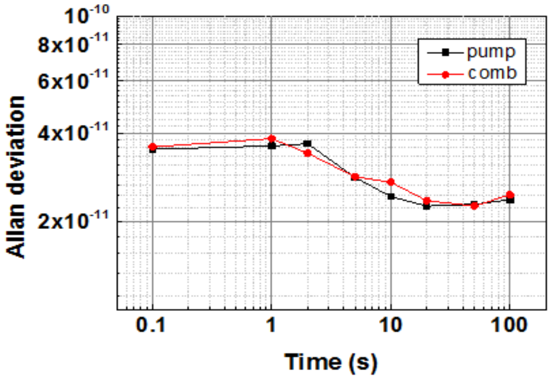

Figure 4-5. Measured Allan deviation of pump source (black square) and the monitored comb (red dot).

We provide a numerical simulation based referred to [114], by deriving the intracavity power on the two resonances at pump and seed. The coupled equation as below, where η_{ext} represents power coupling efficiency

$$P_{cav,\mathrm{p}} = P_{in,\mathrm{p}} \cdot \eta_{ext,\mathrm{p}} \cdot \frac{F}{2\pi} \cdot \frac{1}{1+4\left(\frac{\nu_p - \nu_{p0} - \Gamma_p^* \cdot (P_{cav,p} + P_{cav,s})}{\Delta\nu}\right)^2}$$

$$P_{cav,s} = P_{in,s} \cdot \eta_{ext,s} \cdot \frac{F}{2\pi} \cdot \frac{1}{1+4\left(\frac{\nu_s - \nu_{s0} - \Gamma_s^* \cdot (P_{cav,p} + P_{cav,s})}{\Delta\nu}\right)^2}$$

The calculated powers versus detunings are shown in Figure 4-2d. The overlap of the two curves indicates that adding a seed laser far away from the pump resonance won't influence the pump modal dynamics thus maintain the comb dynamics. This also verifies that the 40 MHz range comes from injection-locking, instead of increased loaded power inside the cavity. Hence the presented scheme allows tolerance from resonance shift, e.g. induced by environmental changes such as thermal drift, up to 40 MHz.

We here show the process of self-injection locking between two comb mode families, one of which artificially introduced by an external optical pump with controlled properties. In more complex comb dynamics [113,115], the self-injection locking occurs between different comb mode families, governing the comb coherent states transitions, and is a key nonlinear process in frequency comb synthesis between multiple optical spectral ranges.

4.5. Summary

We have experimentally shown that a coherent Kerr frequency comb can be generated using a bichromatic pump, where the spacing can be controlled by a seeding laser pumped at another resonance with 10% power compared to the primary pump. The dynamical study on transition between incoherent and coherent comb states helps to understand the self-injection locking mechanism as well as demonstrate deterministic control of the coherent comb formation through another low-power laser.

Chapter 5.

A Low-Phase-Noise 18 GHz Kerr Frequency Microcomb Phase-Locked Over 65 THz

5.1. Introduction

This chapter discusses a low-phase-noise Kerr frequency comb generated from a silicon nitride spiral resonator. With the small and flattened group velocity dispersion, the 18 GHz Kerr frequency comb spans nearly half an octave and contains a record-high number of comb lines at more than 3,600. Spectral modulation induced by mode interactions is also evidently observed. A single bandwidth-limited RF beat note is observed and the single-sideband (SSB) phase noise analysis reveals the lowest phase noise floor achieved to date in free-running Kerr frequency combs, -130 dBc/Hz at 1 MHz offset for the 18 GHz carrier. The long-term frequency stability is characterized and the measured free-running Allan deviation is 2×10^{-8} in 1 s, consistent with the frequency fluctuations caused by the pump wavelength drift. Feedback stabilization further improves the frequency stability to 7×10^{-11} in 1 s.

5.2. An 18 GHz Frequency Comb Generated in A Silicon Nitride Microring

Figure 5-1a shows an optical micrograph of the silicon nitride spiral resonator and the cavity dispersion simulated with full-vector finite-element mode solver. The microresonator is fabricated with CMOS-compatible processes for the low-pressure chemical vapor deposition of the nitride and it is annealed at a temperature of 1200^{o}C to reduce the N-H overtone absorption. The spiral design ensures the relatively large resonator fits into a tight field-of-view to avoid stitching and discretization errors during the photomask generation [27], which can lead to higher cavity losses. Bends in the resonator have diameters greater than 160 μm to minimize the bending-induced dispersion. The waveguide cross-section is designed to be 2 μm × 0.75 μm so that not only the group velocity dispersion (GVD) but also the third order dispersion (TOD) is small in this microresonator. The small and flattened GVD is critical for broadband comb generation [116]. Figure 5-1b shows the pump mode is critically coupled with a loaded quality factor approaching 660,000 (intrinsic quality factor at 1,300,000). A tunable external-cavity diode laser (ECDL) is amplified by an L-band erbium doped fiber amplifier (EDFA) to 2W and then coupled to the microresonator with a single facet coupling loss of 3 dB, resulting in a coupled pump power 5 times higher than the threshold pump power. A 1583-nm long-pass filter is used to remove the amplified spontaneous emission noise from the EDFA. Both the pump power and the microresonator chip's temperature are actively stabilized such that the fluctuation of the on-chip pump power is less than 10^{-3}. A 3-paddle fiber polarization controller and a polarization beam splitter cube are used to ensure the proper coupling of TE polarization into the microresonator. To obtain the Kerr frequency comb, the pump wavelength is first tuned into the resonance from the high frequency side at a step of 1 pm (~118 MHz) until a broadband comb is observed on the optical spectrum analyzer. Importantly, it is then necessary to switch to fine control of the pump wavelength at a step of <5 MHz in order to drive the comb from a noisy state to a phase-locked state. At the output, 5-nm WDM filters are used to notch the pump and a dispersion compensating fiber jumper is used to properly cancel the dispersion introduced by the WDM filters. An example of the Kerr frequency comb is shown in Figure 5-1c, spanning nearly half an octave (65 THz, defined as

60 dB below the maximum comb line power) and covering multiple telecommunication bands (E, S, C, L and U bands) with the comb spacing of 17.986 GHz. Of note, the generated Kerr frequency comb contains more than 3,600 comb lines, the record large number of Kerr comb lines made possible by the small and flattened GVD.

Two TE modes with different free spectral ranges (18 and 17.4 GHz) are supported in the spiral resonator and their resonance wavelengths periodically get close to each other with a period of ≈ 4 nm. Figure 5-2a (top) plots the resonance wavelength offsets of the second-order mode family with respect to the fundamental mode family. The zero crossings (red horizontal line) represent the wavelengths where the resonances of the two mode families are supposed to be degenerate. However, the degeneracy is lifted due to the mode interaction, as evidenced by the openings in the resonance wavelength offsets around the zero crossings. Such anti-crossing phenomena leads to the local disruption of dispersion and modifies the phase matching condition of the comb generation process [20,92,117,118]:

$$\Delta k(\omega_{FSR}\mu) = \beta_2 \omega_{FSR}^2 \mu^2 + \kappa(\omega_{FSR}\mu) + \gamma P_{int} - \delta$$

where β_2 is the GVD, ω_{FSR} the free spectral range, μ the mode number, $\kappa(\omega_{FSR}\mu)$ the periodic local dispersion disruption by the mode interaction, γ the nonlinear coefficient, P_{int} the intracavity pump power, and δ the pump wavelength detuning. While the local dispersion disruption is 2 to 3 GHz, the GVD is only 20 fs^2/mm and it takes ≈ 1,000 modes before the GVD induced phase mismatch becomes comparable to that induced by the mode interaction. Thus the phase matching condition around the pump should be dominated by the mode interaction, as evidently shown in Figure 5-2a where the correlation between the zero crossings (top) and the local maxima of the Kerr frequency comb (bottom) is observed. Figure 5-2b shows the simulated Kerr frequency comb obtained by numerically solving the Lugiato-

Lefever equation for 3500 modes, including the local dispersion disruptions [20]. The broad bandwidth and the apparent 4-nm periodic spectral modulation agree with the experimental observation. The dynamics of mode interaction effect in shaping the comb formation is discussed in details in Turing pattern comb in session 7.2.2.

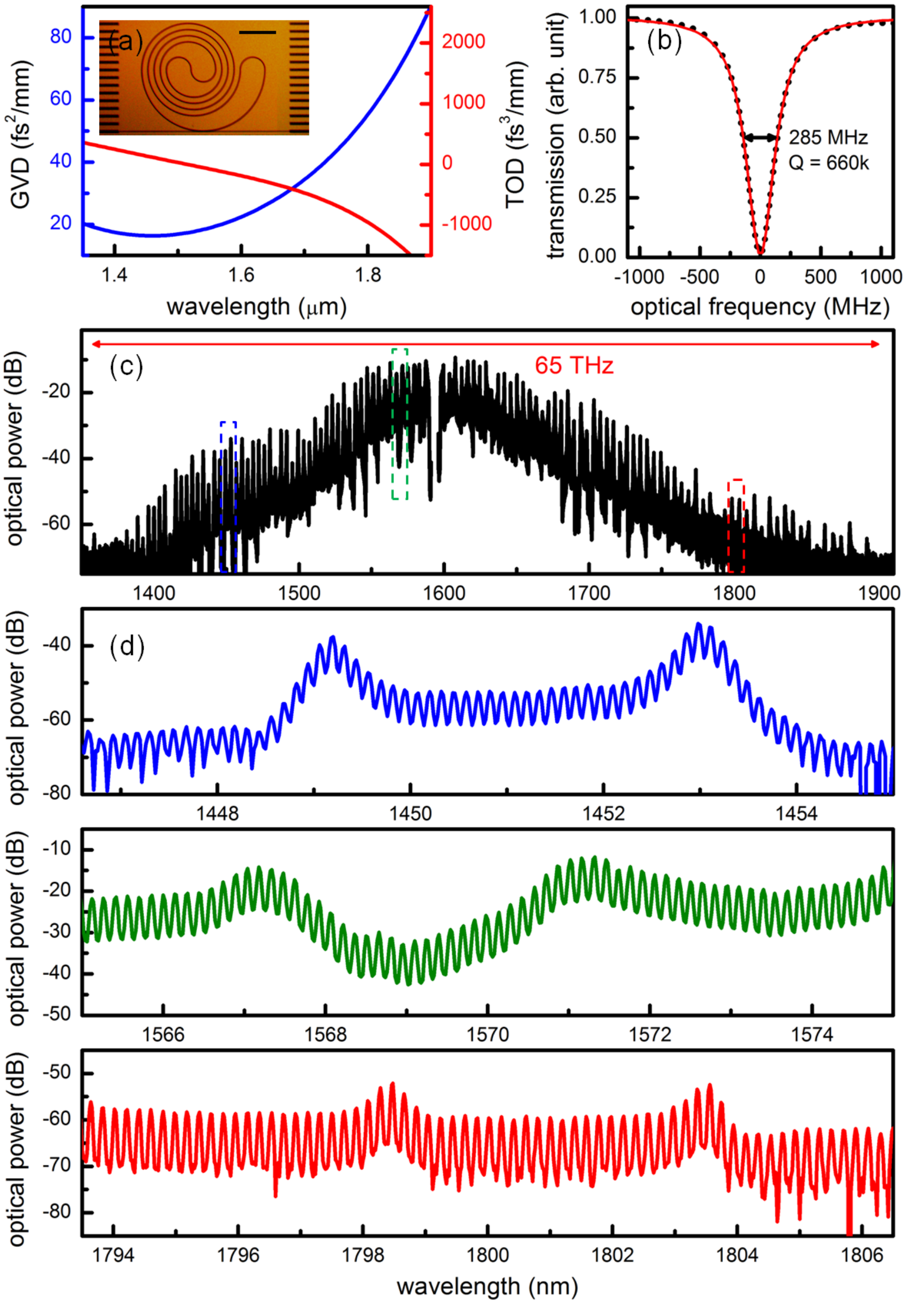

Figure 5-1. A phase-locked 18 GHz Kerr frequency comb spanning over 65 THz.

(a) Simulated group velocity dispersion (GVD) and third order dispersion (TOD) of the ring resonator, featuring small TOD which is beneficial for broad comb generation. Inset: An optical micrograph of the spiral resonator, with a total cavity length of 8.04 mm and a mode area of 1.3 μm^2. Adiabatic mode converters (the dark bars on the side of the chip) are implemented to improve the coupling efficiency from the free space to the bus waveguide (the bottom straight line across the chip). Scale bar: 250 μm. **(b)** Example critically-coupled resonant pump mode at 1595.692 nm, with a 285 MHz loaded cavity linewidth. Black dots are the measured data points and the red curve is the fitted Lorentzian lineshape. **(c)** Example generated Kerr frequency comb, with a broad spectrum spanning nearly half an octave at 65 THz and covering multiple telecommunication bands (E, S, C, L and U bands). **(d)** Zoom-in views of the comb spectra from 1446.5 nm to 1455 nm (blue), 1565 nm to 1575 nm (green), and 1793.5 nm to 1806.5 nm (red). Even in the wings of the spectrum, native-FSR-spacing comb lines are clearly observed.

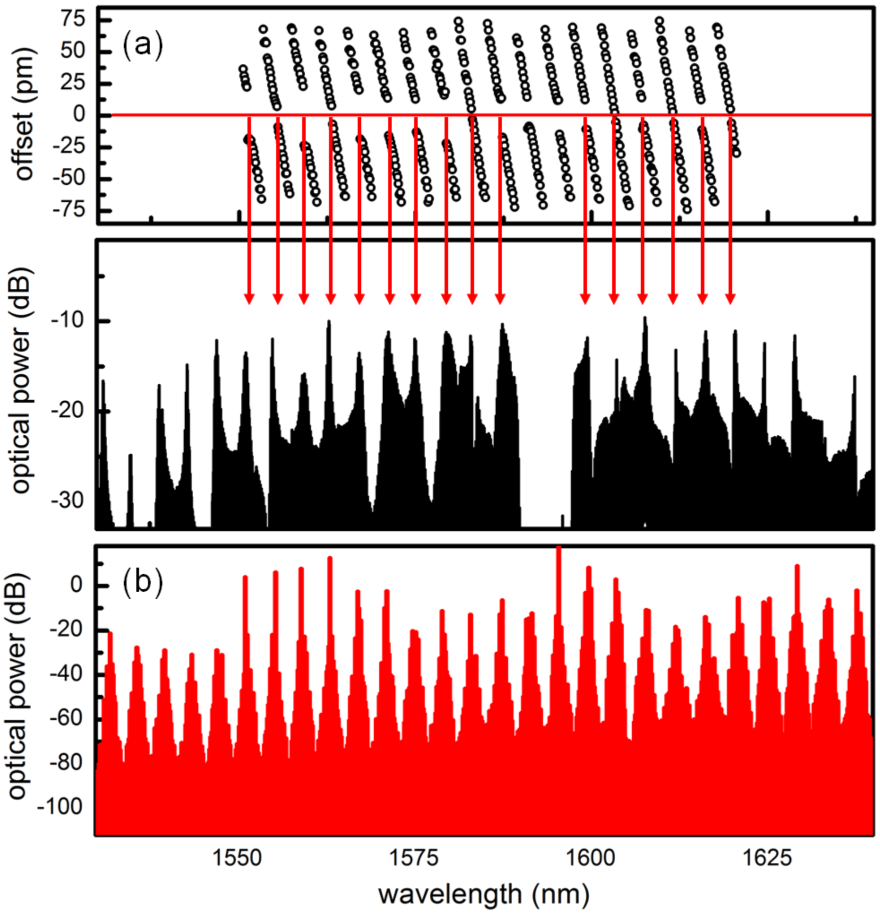

Figure 5-2. Mode interaction induced spectral modulation of the Kerr frequency comb. (a) Resonance frequency offsets of the second-order mode family with respect to the fundamental mode family (top) as well as the zoom-in view of the Kerr frequency comb (bottom). **(b)** Simulated Kerr frequency comb by solving the Lugiato-Lefever equation, also showing a 4-nm periodic spectral modulation when the local dispersion disruptions are included in the model.

5.3. Phase Noise Measurement of The Photonic-Microwave Oscillator

Figure 5-3a shows the RF amplitude noise spectra of the Kerr frequency comb [24,119]. When the primary comb line spacing is incommensurate with the fundamental comb spacing, multiple RF peaks will occur due to the beating between different comb families (Figure 5-3a inset). Next, with fine control of the pump wavelength, the offset between different comb families can be made zero such that the RF amplitude noise spectrum shows no excess noise (Figure 5-3a). To characterize the RF beat note of the 18 GHz Kerr frequency comb, a high-speed photodetector is used to demodulate the frequency comb at 17.986 GHz, and an 18.056 GHz local oscillator is used to downmix the electronic signal to the baseband for analysis. Figure 3b plots the RF spectra of the beat notes from three different filtered spectral regions of the comb (black curve: whole spectrum excluding the pump; blue curve: 1529 to 1538 nm; red curve: 1555 to 1564 nm). The pedestal below 500 kHz offset frequency comes from the 18.056 GHz local oscillator. All three measurements show bandwidth-limited beat notes at 17.986 GHz, characteristic of an equidistant Kerr frequency comb as those of a non-equidistant comb will either reside at distinct frequencies or show different linewidths and phase noise characteristics (Figure 5-4) [27]. A second-harmonic-generation optical intensity autocorrelation is implemented to characterize the temporal structure of the phase-locked Kerr frequency comb and the result is shown in Figure 5-3c. The trace has a contrast of ≈ 2, characteristic of a comb without a clean circulating high-peak power pulse. Recently, a phase-locked Kerr frequency comb without mode-locking is also observed in a WGM microresonator [26] and the self-injection locking is shown to be the underlying mechanism for driving the Kerr frequency comb into a phase-locked state [25,26]. Compared to smaller microresonators where mode-locking are demonstrated [77,120], self-injection locking plays a more important role in low-repetition-rate Kerr frequency combs because the more frequent local dispersion disruptions impede the mode-locking from occurring [121].

Figure 5-4shows the SSB phase noise spectra of the RF beat notes. To probe the possibility of degraded phase noise for different spectral slices of the comb due to the complicated nonlinear comb generation process [24], here again we measure the phase noises at three different spectral regions (A, blue curve: 1529 to 1538 nm; B, red curve: 1555 to 1564 nm; C, black curve: whole spectrum excluding the pump). Compared to the comb lines in the region A, the comb lines in the region B are characterized by their higher optical power and better amplitude uniformity. However, the phase noise results show that the mechanism for phase noises at different parts of the Kerr frequency comb is identical and the minutely better phase noise floor of the region B and C is a direct consequence of the higher comb power. The olive line shows the phase noise of the local oscillator used for downmixing the RF beat note of Kerr frequency comb and it is worth mentioning that the phase noise of the comb beat note becomes comparable or better than that of the commercially available high performance microwave local oscillators for offset frequencies higher than 20 kHz. The record low phase noise floor of -130 dBc/Hz, as well as the record large number of Kerr comb lines, can be well-suited for further improving the high-capacity coherent data transmission with advanced phase modulation techniques [12]. For offset frequency below 10 kHz, the phase noise is dominated by frequency flicker (30 dB/decade) which can be accounted by noise induced from the wavelength drift of the pump laser.

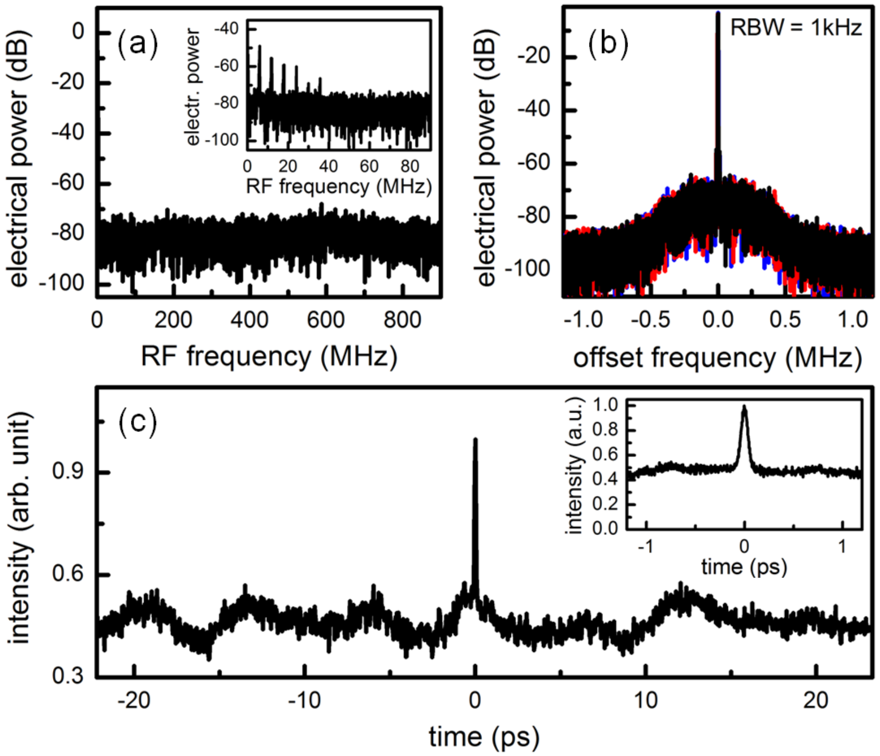

Figure 5-3. Offset and noise characteristics of the phase-locked 18 GHz comb.

(a) RF amplitude noise of the offset-free Kerr frequency comb. Inset: an example RF amplitude noise of the Kerr frequency comb showing multiple peaks due to the beating between different comb families. The comb is tuned to be offset-free by fine control of the pump wavelength. **(b)** RF spectra of the beat notes from three different filtered spectral regions of the comb (black curve: whole spectrum excluding the pump; blue curve: 1529 to 1538 nm; red curve: 1555 to 1564 nm). All three measurements show bandwidth-limited beat notes at 17.986 GHz, characteristic of a phase-locked comb. The pedestal below 500 kHz offset frequency comes from the local oscillator used for downmixing the 17.986 GHz beat note. **(c)** Optical intensity autocorrelation of the phase-locked Kerr frequency comb. The trace has a contrast of ~ 2, characteristic of a comb without a clean circulating high-peak power pulse.

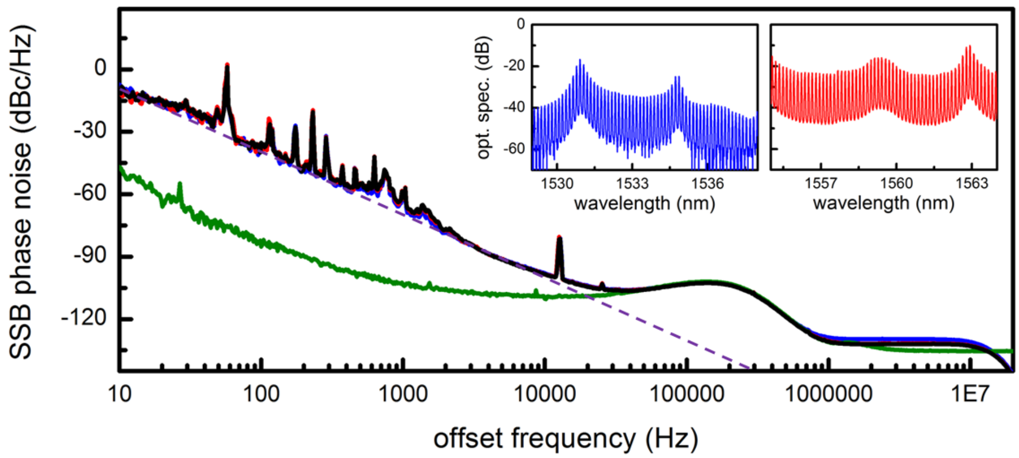

Figure 5-4. Single-sideband (SSB) phase noises of the beat notes from different spectral regions of the comb.

Three filtered spectral regions of the comb with the comb lines are shown in the inset (blue curve: 1529 to 1538 nm; red curve: 1555 to 1564 nm). The black curve shows the whole spectrum excluding the pump. All SSB phase noise spectra show a very low phase noise floor of -130 dBc/Hz at 1 MHz offset from the carrier. For offset frequency below 10 kHz, the phase noise has a roll-off of 30 dB/decade (purple dashed line). The olive curve is the SSB phase noise of the local oscillator used for downmixing the 17.986 GHz beat note.

5.4. Allan Deviation Characterization and Stability Improvement

Figure 5-5 shows the Allan deviation of the free-running (open squares) and the stabilized (closed squares) Kerr frequency comb spacing. The free-running Allan deviation is measured at 2×10^{-8} in 1 s, increase to 1×10^{-7} in 10 s, and then gradually decrease to 5×10^{-8} in 100 s. As the detuning changes the intracavity power, the comb spacing linearly shifts by 57 Hz per MHz of pump wavelength detuning in our microresonator (Figure 5-5 inset). On the other hand, the instability of the employed pump laser wavelength is characterized by measuring the heterodyne beat note between the pump laser and a tooth of a fiber frequency comb. The estimated comb spacing instability caused by the pump wavelength drift is also plotted in Figure 5-5 (red diamond) and it shows the pump wavelength drift is the main noise source limiting the long term stability of the Kerr frequency comb spacing. Finally, a proportional-integral feedback stabilization of the comb spacing by controlling the pump wavelength is implemented to improve the long-term stability by more than two orders of magnitude, reaching $7\times10^{-11}/\tau^{0.84}$, comparable to that of a commercially available high performance microwave oscillator.

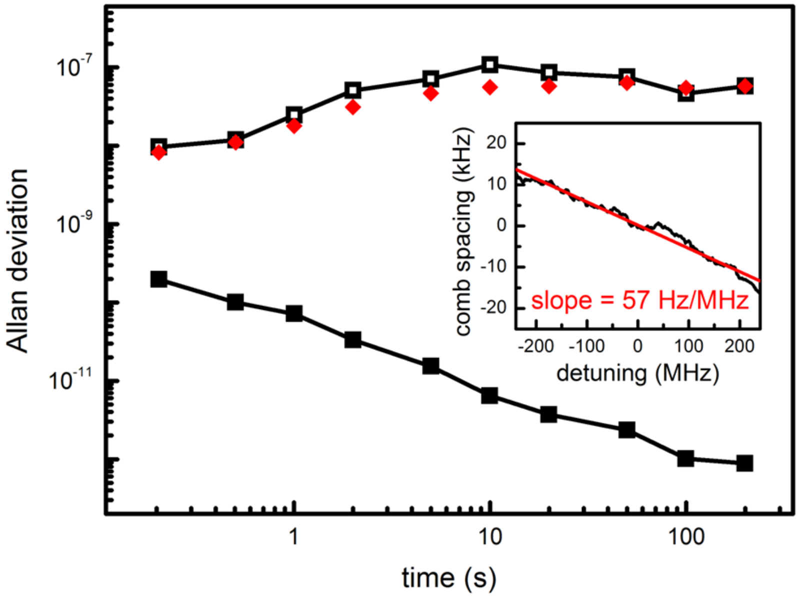

Figure 5-5. Allan deviation of the free-running (open squares) and the stabilized (closed squares) Kerr frequency comb spacing.

In free running mode, the comb spacing stability is limited by the fluctuation resulting from the pump laser wavelength drift (red diamond). Feedback stabilization is achieved by monitoring the comb spacing and controlling the pump laser wavelength to compensate the errors with a proportional-integral controller. Inset: The comb spacing as a function of the pump wavelength detuning, determined at 57 Hz/MHz in our microresonator.

5.5. Conclusion

In summary, we report a low-phase-noise Kerr frequency comb generated from a silicon nitride spiral resonator. The 18 GHz Kerr frequency comb spans nearly half an octave and contains a record-high number of comb lines at ~3,600. We study the SSB phase noise and report the lowest phase noise floor achieved to date in Kerr frequency combs, -130 dBc/Hz at 1 MHz offset for 18 GHz carrier. Limited by the wavelength drift of the employed pump laser, the free-running Allan deviation is measured at 2×10^{-8} in 1 s and it is improved to 7×10^{-11} at 1 s by a feedback control of the pump wavelength. With half-octave-spanning bandwidth, record large number of Kerr comb lines, and record low phase noise floor, the reported system is a promising compact platform not only for achieving self-referenced Kerr frequency combs but also for improving high-capacity coherent telecommunication systems. Although ultrashort pulses are not generated directly from this microresonator, the high-coherence phase locking property lends itself to pulse shaping technique for harvesting the temporal features of the Kerr frequency comb [14].

Chapter 6.

A Broadband Chip-Scale Optical Frequency Synthesizer at 2.7×10^{-16} Relative Uncertainty

6.1. Introduction

This chapter, as continuous work based on the last chapter, discusses the first fully stabilized CMOS-compatible chip-scale Kerr microcomb with a frequency relative uncertainty down to 2.7×10^{-16}. The silicon nitride spiral resonator is designed and fabricated to generate a Kerr microcomb, at 18 GHz native spacing and spanning more than 8 THz over more than 400 comb lines. The comb's two degrees of freedom, one of the comb line frequencies and the comb spacing, are phase locked to a known optical reference and a microwave synthesizer respectively. Active stabilization on the comb spacing improves the RF stability by six orders of magnitude, reaching residual instrument-limited close-to-carrier (10 Hz) phase noise of -70 dBc/Hz and Allan deviation of 3.6 $\mathrm{mHz}/\sqrt{\tau}$. In the optical frequency, forty-six lines of the Kerr microcomb subset are selected and compared against the current benchmark fiber laser frequency comb and the frequency relative uncertainty of the stabilized Kerr microcomb is demonstrated down to 50 mHz. The reported system is a promising compact platform for coherent Raman spectroscopy [122], optical clockwork [7], coherent communications [123], arbitrary waveform generation [124], and astrophysical spectrography [9,10,125].

6.2. Device Characterization and Kerr Comb Generation

Figure 6-1a shows the experimental setup for the Kerr microcomb generation and stabilization. The silicon nitride spiral resonator is fabricated with CMOS-compatible processes and the waveguide cross-section is designed to have small and flattened group velocity dispersion for broadband comb generation. Planar ring geometry is employed because of the reduced sensitivity to the environmental perturbation, along with the fewer discrete transverse resonator modes, and the flexibility to tailor the cavity dispersion for efficient and broadband comb generation. Detailed properties of the microresonator is shown in Figure 6-2. Figure 6-2a shows a cross-section scanning electron micrograph of the microresonator waveguide, with an estimated 82° to 88° slope of the vertical sidewalls. The refractive index of the low pressure chemical vapor deposition (LPCVD) Si_3N_4 film was measured with an ellipsometric spectroscopy (Woollam M-2000 ellipsometer) and then fitted with the Sellmeier equation assuming a single absorption resonance in the ultraviolet. The fitted Sellmeier equation, $n(\lambda) = \sqrt{1 + \frac{2.90665\lambda^2}{\lambda^2 - 145.05007^2}}$, and the sidewall angle were both imported into the COMSOL Multiphysics for the microresonator design. Figure 6-2b shows the modeled free spectral range (FSR) of the first two TE modes of the microresonator. While the fundamental mode features a FSR of 17.9 GHz, the TE_2 mode has a slightly lower FSR and thus the resonances of the TE_2 family approaches that of the fundamental family about every 4 nm ($\frac{FSR^2}{\Delta FSR} = 460GHz$). The mode interaction when the resonances are close leads to local disruption of the phase matching condition [92,117,118] and results in the periodic amplitude modulation on the Kerr comb spectrum (Figure 6-1b).

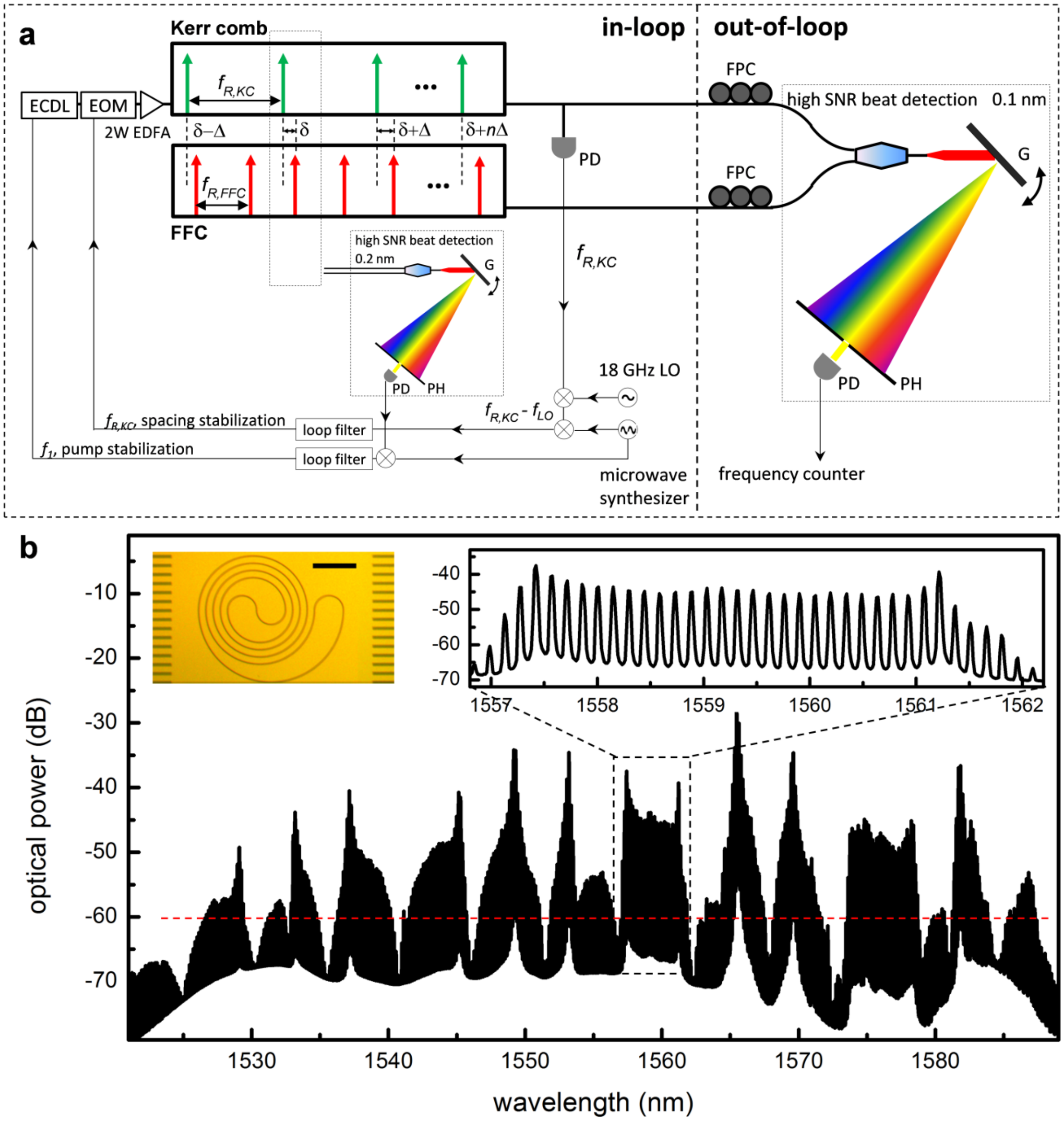

Figure 6-1. A stabilized chip-scale optical frequency comb.

(a) Measurement setup schematic for the generation and stabilization of the chip-scale optical frequency comb. To stabilize the comb's first degree-of-freedom, an ECDL is phase-locked to an optical reference, here a mode of a stabilized fiber laser frequency comb, and then amplified to 2 W to pump the Si_3N_4 microresonator. To stabilize the comb's second degree-of-freedom, the Kerr comb spacing, $f_{R,KC}$, is monitored by sending the comb to a high-speed photodetector (3 dB bandwidth more than 15 GHz) and downmixing the electronic signal to the baseband with a local oscillator at f_{LO} = 18 GHz. A fiber electro-optic modulator (EOM) controls the pump power and stabilizes the comb spacing.. δ: frequency difference between the pump and the adjacent fiber laser frequency comb line. Δ= $f_{R,KC} - \lfloor f_{R,KC}/f_{R,FFC} \rfloor f_{R,FFC}$. FFC: erbium fiber laser frequency comb; PD: the photodetector; G: grating; PH: pinhole; and FPC: fiber polarization controller. (**b)** Example stabilized Kerr frequency comb spectrum, consisting of more than 400 comb lines in the telecommunication wavelength range. The horizontal (red) dashed line denotes the 1 μW per comb line power level. Left inset: optical micrograph of the spiral microresonator. Scale bar: 250 μm. Right inset: comb lines with native spacing at the cavity's free-spectral range are clearly observed.

Figure 6-2c and d show the modeled group velocity dispersion (β_2, GVD) and third order dispersion (β_3 , TOD). The non-equidistance of the cold cavity modes, $D = (\omega_{m+1} - \omega_m) - (\omega_m - \omega_{m-1})$, can be calculated using the equation $D = -\frac{(\beta_2 L)}{2\pi}\omega_{FSR}^3 + \frac{(\beta_2 L)^2}{4\pi^2}\omega_{FSR}^5 - \frac{(\beta_3 L)}{4\pi}\omega_{FSR}^4$, where L is the cavity's length and ω_{FSR} is the cavity's free spectral range.

Due to the large refractive index of the Si_3N_4 waveguide, a 600 µm long adiabatic mode converter (the Si_3N_4 waveguide, embedded in the 5×5 µm^2 SiO_2 waveguide, has gradually changing widths from 0.2 µm to 1 µm) is implemented to improve the coupling efficiency from the free space to the bus waveguide. The input-output insertion loss for the waveguide does not exceed 6 dB.

The loaded quality factor Q of the pump mode is 660,000 (intrinsic Q ~ 1,300,000) and 1 W of pump power is critically coupled to the microresonator, resulting in a maximum coupled pump power 5 times higher than the threshold pump power. The pump wavelength is 1598.7 nm. A 1583-nm long-pass filter removes the amplified spontaneous emission noise from the EDFA. The microresonator chip temperature is actively stabilized to +/- 10 mK. A 3-paddle fiber polarization controller and a polarization beam splitter cube are used to ensure proper coupling of the TE polarization into the microresonator. To obtain the Kerr microcomb, the pump wavelength is first tuned into the resonance from the high frequency side at a step of 10 pm until primary comb lines are observed on the optical spectrum analyzer, prior to fine control to drive the comb from a noisy state to a phase-locked state. The threshold pump power is estimated to be 200 mW using the equation $P_{th} = \frac{\pi}{8\eta}\frac{n_0}{n_2}\frac{\omega_p}{\omega_{FSR}}\frac{A}{Q^2}$, where A=1.3μm^2 is the mode area, η=0.5 is the coupling parameter, ω_p is the pump frequency, and ω_{FSR} is the cavity's free spectral range [25].

The output is first short-pass filtered using a 1550/1590 nm wavelength division multiplexer and then boosted in power with a 13 dBm C-band preamplifier to increase the signal to noise ratio (SNR) of the photodetector signal. Figure 6-1b shows the Kerr microcomb spectrum, spanning more than 8 THz and consisting of more than 400 comb lines.

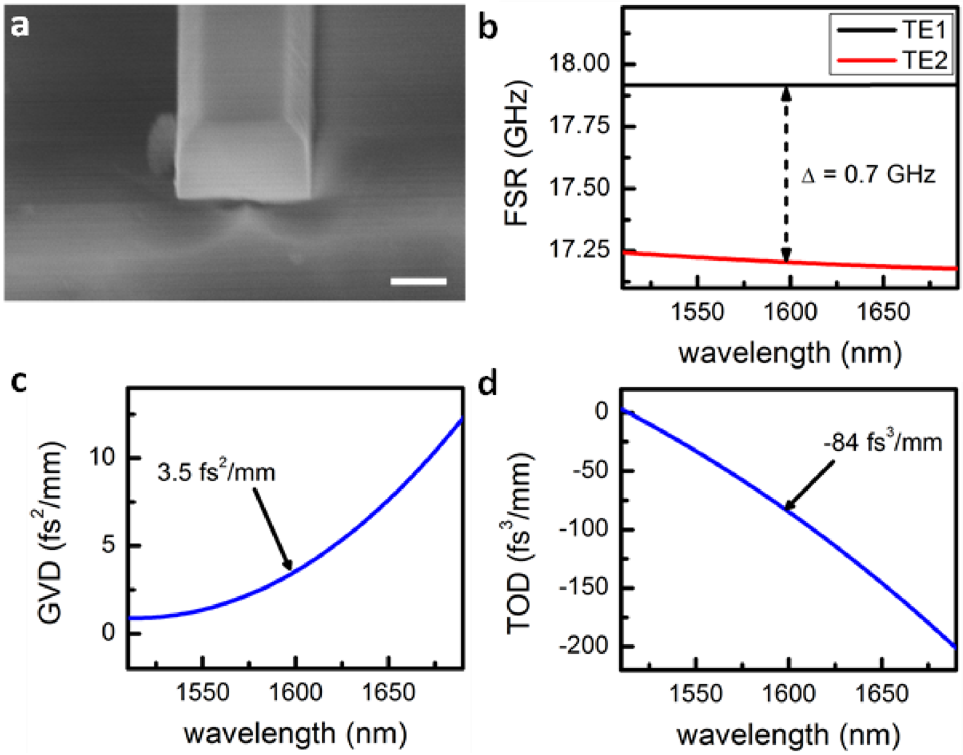

Figure 6-2. Properties of the Si_3N_4 microresonator.

(a) Scanning electron micrograph of the waveguide cross-section. Scale bar: 500 nm. **(b)** Modeled free spectral range of the first two TE modes of the chip-scale optical frequency comb. **(c)** Modeled group velocity dispersion of the fundamental mode, measuring a GVD of 3.5 fs^2/mm at the pump wavelength. **(d)** Modeled third order dispersion of the fundamental mode, measuring a TOD of -84 fs^2/mm at the pump wavelength.

To ensure the Kerr microcomb is driven from a noisy state to a phase-locked state [32] and to verify it is not consisted of many sub-comb families with offsets [115,126], RF amplitude noise and fundamental beat note of different filtered Kerr microcomb segments are monitored.

As the pump wavelength was tuned into the resonance from the high frequency side, we first observed multiple RF spikes because the primary comb line spacing is incommensurate with the fundamental comb spacing. The state with incommensurate spacing was unstable and it made frequent transition to high-noise state characterized by elevated RF amplitude noise (45 dB higher than the phase-locked comb state). Next, with fine control of the pump wavelength (10 MHz/step), the offset between different comb families can be made zero such that the RF amplitude noise spectrum showed no excess noise (Figure 6-3). The phase-locked comb typically stabilized for hours.

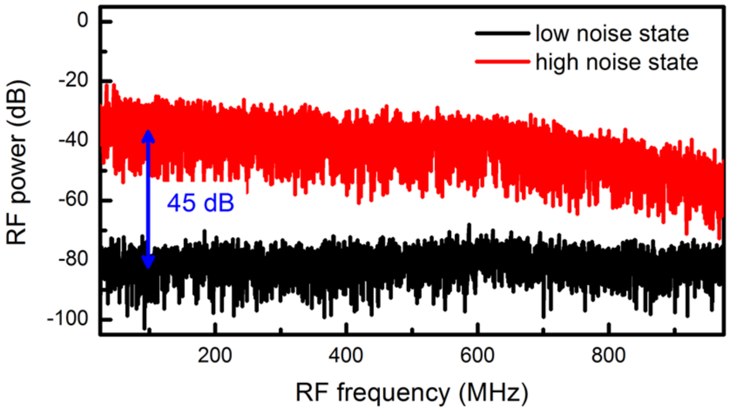

Figure 6-3. RF amplitude noise spectra of the high noise state and the low noise phase-locked comb state.

With the proper pump wavelength, RF amplitude noise dropped by 45 dB and approached the detector background noise, indicative of the transition into a phase-locked state.

To verify the Kerr frequency comb is continuously equidistant, not consisted of many sub-comb families with offsets [24], we measured the comb spacing and the amplitude noise of various different filtered segments of the Kerr frequency comb (1553.5-1554.5nm, 1555-1556nm, 1556.2-1557.2nm, 1558-1559nm, 1560-1561nm, 1561.7-1562.7nm, 1563.5-1564.5nm, 1566-1567nm, 1568.5-1569.5nm, 1570.5-1571.5nm, 1572.3-1573.3nm, 1574-1575nm, 1577-1578nm 1578.5-1579.5nm, 1580.3-1581.3nm). The comb spacing was measured to be identical at 17.9 GHz within the RBW of 390 kHz (Figure 6-4a) and 1 kHz (Figure 6-4b) for the 15 filtered comb segments from 1553.5nm to 1581.3nm. No other peaks were observed. Absence of sub-comb families with offset frequencies was also independently confirmed by the amplitude noise measurements, showing no peaks and excess noise above the detector background noise. The Kerr microcomb’s continuous equidistance was thus verified.

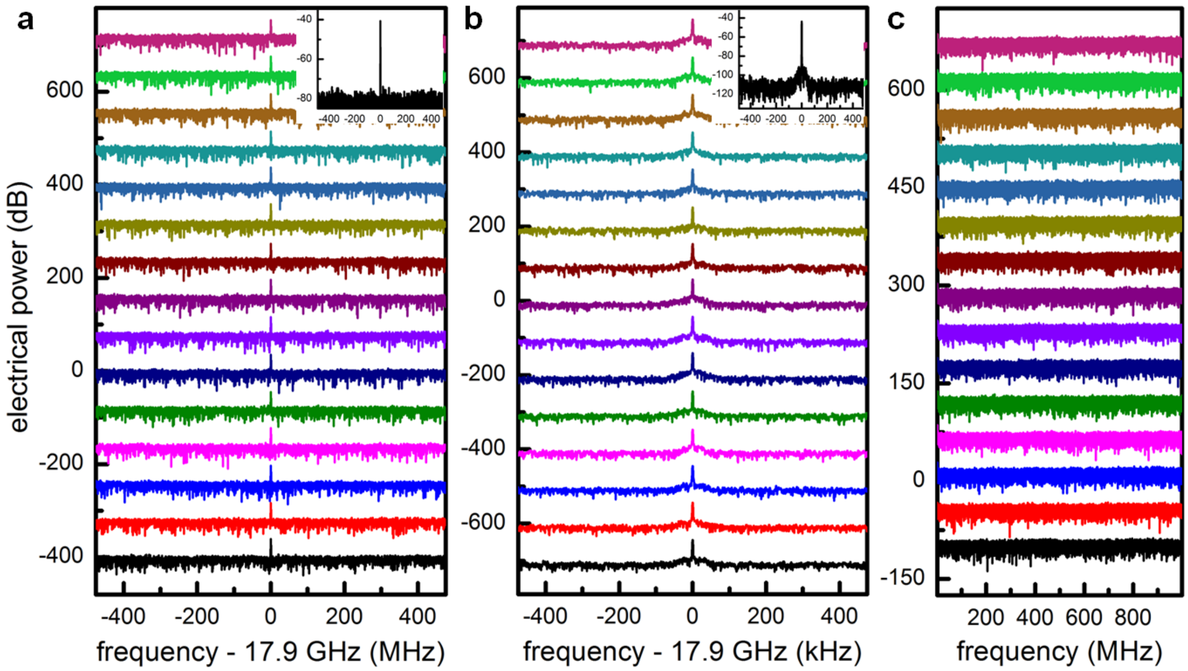

Figure 6-4. Confirmation of continuously equidistant Kerr frequency comb.
(a) Comb spacing spectra of 15 filtered comb segments with scan ranges of 1 GHz. **(b)** Comb spacing spectra of 15 filtered comb segments with scan ranges of 1 MHz. **(c)** Amplitude noise spectra of 15 filtered comb segments with a scan range of 1 GHz.

6.3. Frequency Comb with Full Stabilization

To stabilize the Kerr microcomb, one of the comb lines and the comb spacing are phase locked to a known optical reference and a microwave synthesizer, respectively. In our system, the known optical reference is derived from an approximately 200 Hz stabilized erbium fiber laser frequency comb (FFC; Menlo Systems) which is also used as a calibration standard later to assess the uncertainty of the Kerr microcomb. As shown in the Figure 6-1a, 1% of the pump mode, which is also the strongest Kerr microcomb line, is tapped and beat with the optical reference on a photodetector. To ensure the beat note has sufficient SNR for reliable feedback stabilization (more than 35 dB with 100 kHz RBW), a 0.2 nm narrow bandwidth monochromator is built to filter the FFC before it is beat with the pump. Figure 6-5a is the free-running beat note, showing a few MHz pump frequency drift in one second. For high bandwidth control of the pump frequency, the diode current of the external-cavity diode laser (ECDL) is directly modulated. Such high bandwidth feedback control, however, has a tradeoff of amplitude modulation of the pump power and consequently excess instability in the comb spacing.

After the Kerr frequency comb was driven into the low phase noise state, we characterized the dependence of the comb spacing on the pump properties by adding a 0.1 Hz sinusoidal change of either pump frequency or pump power and measuring the corresponding comb spacing oscillation amplitude with a frequency counter. Figure 6-6b depicts the dependence of comb spacing on pump power. This effect is partly compensated by saturating the erbium doped fiber amplifier and later eliminated by the second feedback loop on the comb spacing. Figure 6-5b shows the stabilized beat note, illustrating a clear single peak at the center with uncompensated noise above the feedback bandwidth of 300 kHz. The beat has a 70 MHz offset to allow RF amplification for higher SNR in the feedback loop. Figure 6-5c is the zoom-in view of the stabilized beat note, showing a resolution limited linewidth of 6 Hz. To quantify the long-term stability of the locked pump frequency, the beat signal is analyzed by a frequency counter and the counting results are shown in Figure 6-5d. The pump frequency remains steady over 1000 seconds with the standard deviation of 1 mHz and the peak-to-peak deviation of 5 mHz.

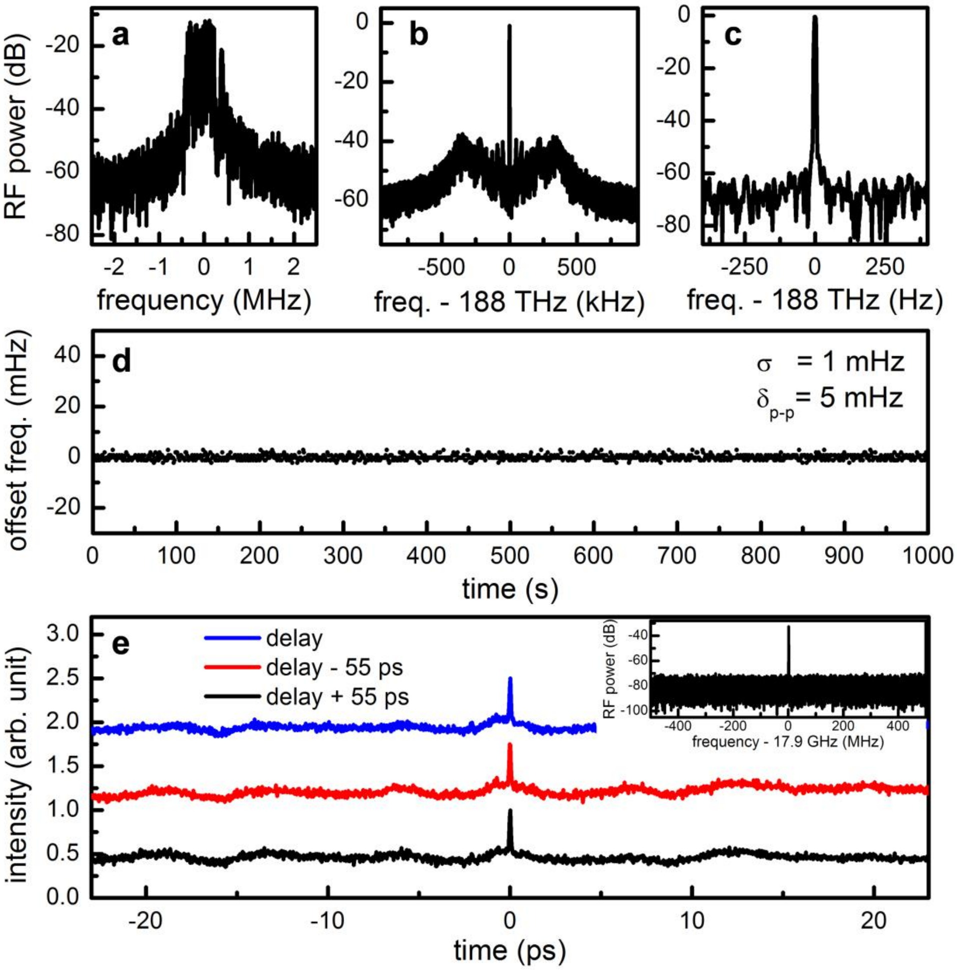

Figure 6-5. Stabilizing the pump frequency to the mHz level residual error and time domain picture of the phase-locked Kerr comb.

(a) Free-running beat note between the pump and the fiber laser frequency comb. To obtain a sufficient signal-to-noise ratio for reliable feedback stabilization (more than 35 dB with 100 kHz RBW), a 200 pm bandwidth monochromator is built to filter the fiber laser frequency comb before it is mixed with the pump. Sweep time is 10 ms. **(b)** RF spectrum of the stabilized beat note with 1 kHz RBW. Control of the pump frequency is achieved by modulating the ECDL diode current, with 300 kHz bandwidth. **(c)** RF spectrum of the stabilized beat note with 6 Hz RBW, showing a resolution limited linewidth of 6 Hz. **(d)** Frequency counting of the stabilized beat note with a gate time of 1 s. The standard deviation over 1000 seconds is 1 mHz, instrument-limited by the stability of the frequency counter. (**e)** Optical intensity autocorrelations of the phase-locked Kerr frequency comb at different delays, showing evidently the repetitive structures and excluding the possibility of noise correlation. Inset: RF spectrum of the free-running comb spacing with a scan range much larger than the cavity linewidth (290 MHz). The comb is tuned to enter the phase-locked state by fine control of the pump frequency.

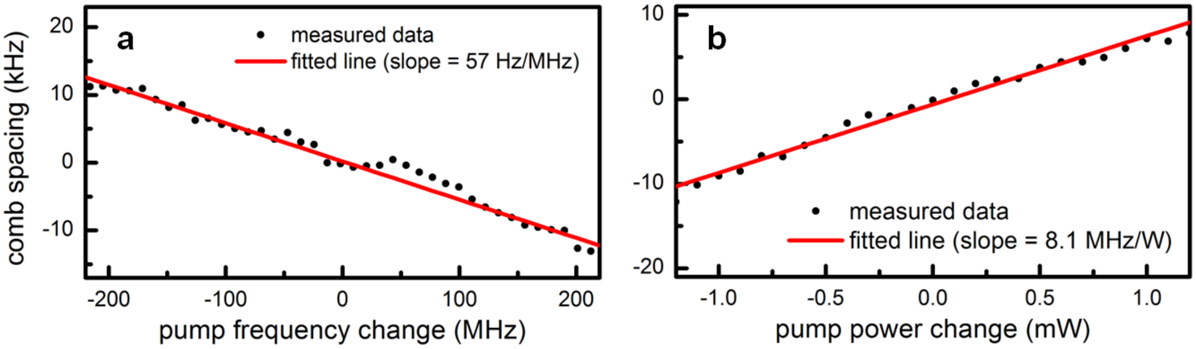

Figure 6-6. Dependence of the comb spacing on the pump properties.
(a) The comb spacing as a function of the pump frequency change, determined at 57 Hz/MHz in our microresonator. **(b)** The comb spacing as a function of the pump power change in the ring, determined at 8.1 MHz/W in our microresonator.

The comb spacing of 17.9 GHz is directly measurable by sending the output to a high speed photodetector (3 dB bandwidth of more than 15 GHz). An 18 GHz local oscillator is used to downmix the electronic signal to the baseband for analysis. The inset of Figure 6-5e plots the free-running comb spacing beat with a scan range of 1 GHz, showing a clean single peak characteristic of an equidistant Kerr microcomb. Details to confirm the continuous equidistance of the Kerr microcomb are summarized in Figure 6-4. Figure 6-5e illustrates the non-collinear second-harmonic-generation optical intensity autocorrelation to reveal the time domain picture of the Kerr microcomb. Careful checks are done to make sure no collinear second-harmonic background is collected in the setup. Even though the Kerr microcomb is operated in a low noise state, clean circulating mode-locked pulses are not formed as evidenced by the elevated AC background of nearly half of the peak. Furthermore, the autocorrelation measurements are performed at three different delays, showing evidently the repetitive temporal structures of the Kerr microcomb and excluding the possibility of noise correlation. Here, a fixed phase relationship between different comb lines is obtained, but the phase relationship may contain some abrupt changes associated with the local dispersion disruptions. Thus mode-locking is prohibited and $\delta - \Delta$ matching becomes the underlying mechanism for driving the Kerr microcomb into a low noise state [24,25,126,127].

The comb spacing is then phase locked and stabilized to a microwave synthesizer by controlling the pump power with a fiber electro-optic modulator (EOM). Pump power is an effective way to control the comb spacing through thermal expansion and thermo-optic effects {Citation} and nonlinear phase accumulation. Figure 6-7a shows the stabilized beat note, with a resolution limited linewidth of 6 Hz and a low close-to-carrier phase noise. To characterize the frequency stability of the comb spacing, single sideband (SSB) phase noise spectra and Allan deviations are measured and shown in Figure 6-7b. Free running with none of the feedback loops engaged, the phase noise of the comb spacing shows a $f^{-3.5}$ dependence on the offset frequency in the vicinity of the carrier. Such close-to-carrier behavior suggests the phase noise is currently dominated by a mixture of technical noise of frequency flicker (30 dB/decade) and frequency random walk (40 dB/decade), rather than limited by quantum noise phase diffusion [128]. Since the microresonator is not thermally insulated from the environment, its interaction with the fluctuating ambient temperature results in the random walk of the comb spacing. Meanwhile, the pump wavelength drift leads to the flicker noise mediated by the residual optical absorption in the microresonator [107]. Such technical noise, however, can be removed by phase locking the beat note to a high performance microwave synthesizer. As shown in Figure 6-7b, the resulting close-to-carrier phase noise can reach the level of -70 dBc/Hz at 10 Hz with a $f^{-1.5}$ dependence on the offset frequency, limited only by the noise of the microwave synthesizer.

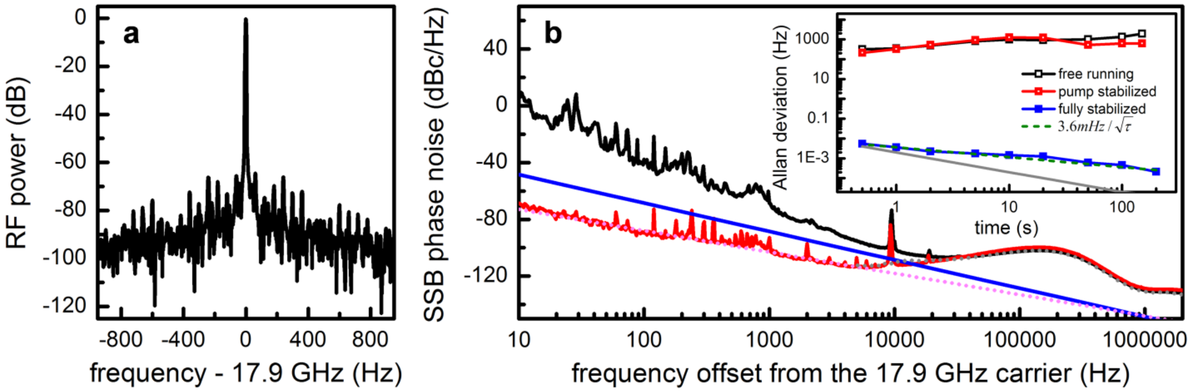

Figure 6-7. Stabilizing the comb spacing to the mHz level residual error.

(a) RF spectrum of the stabilized comb spacing, showing a resolution limited linewidth of 6 Hz. Control of the comb spacing is achieved by modulating the pump power via a fiber EOM. (**b)** Single-sideband (SSB) phase noises of the free-running (black curve) and stabilized (red curve) comb spacing. Free running, the phase noise of the comb spacing shows a $f^{-3.5}$ dependence on the offset frequency in the vicinity of the carrier. Such technical noises can be removed by phase locking the beat note to a high performance microwave synthesizer and the resulting close-to-carrier phase noise can reach the level of -70 dBc/Hz at 10 Hz with a $f^{-1.5}$ dependence on the offset frequency (pink dashed curve), limited only by the microwave synthesizer. For offset frequencies above 10 kHz, on the other hand, the phase noise of the comb spacing is better than that of the 18 GHz local oscillator used for downmixing the electronic signal (gray dashed curve) and the measurement is thus instrument limited. Phase noise estimated from Eq. 1 is −148 dBc/Hz at 1 MHz and it grows with a f^{-2} dependence on the offset frequency. The estimated phase noise reaches −108 dBc/Hz at 10 kHz and starts to exceed the noise level of the 18 GHz local oscillator, matching the experimental observations (blue curve). Inset: Allan deviation of the comb spacing under free-running (black open squares), pump frequency stabilization (red semi-open squares) and full stabilization (blue closed squares). The fully stabilized comb spacing shows a consistent trend of 3.6 mHz/$\sqrt{\tau}$ (green dashed line) when the gate time is in the range from 0.5 s to 200 s. The gray line denotes the counter-limited Allan deviation.

In terms of the stabilization approach, alternatively a rubidium locked diode laser at 1560 nm can also be used as the optical reference for phase locking one of the comb lines [129–131]. As Si_3N_4 microresonators suffer from lower Q at optical C-band due to residual N-H absorption [20], we prefer to pump the microresonator at optical L-band for low threshold comb generation. In the alternative scheme, the 1560 nm comb line is thus only accessible after the microresonator when the Kerr microcomb is generated (Figure 6-8). Here the 1560 nm comb line was selected by a narrowband monochromator and beat with the optical reference on a photodetector after the comb generation stage. The rest of the setup was the same as the one shown in Figure 6-1a. Figure 6-8b shows that the beat note can be equally well stabilized to a resolution limited linewidth of 6 Hz.

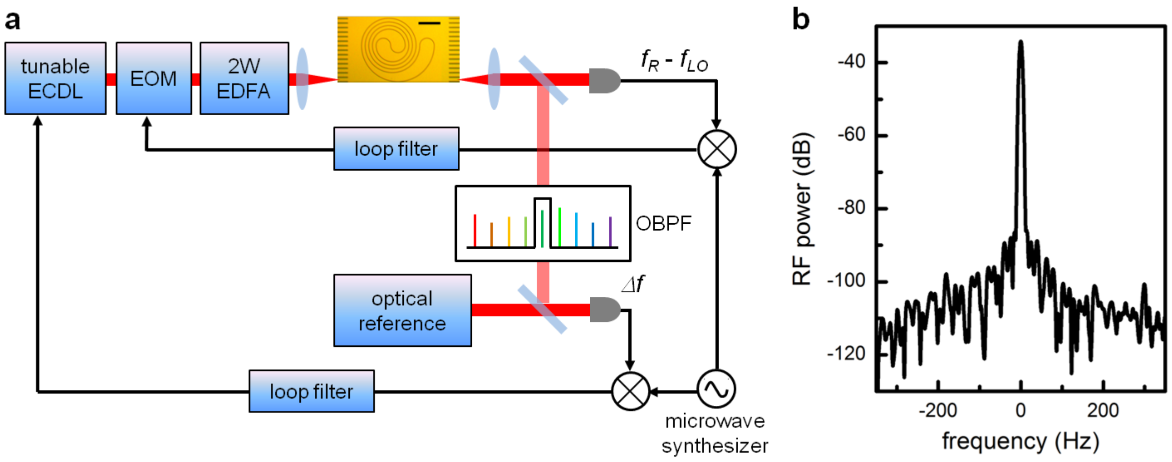

Figure 6-8. Schematic of the alternative experimental setup for generation and stabilization of the chip-scale optical frequency comb.

(a) After the microresonator, the 1560 nm comb line was selected by a narrowband monochromator and beat with the optical reference on a photodetector. The rest of the setup was the same as the one shown in Figure 6-1a. **(b)** RF spectrum of the stabilized beat note, showing a resolution limited linewidth of 6 Hz. Control of the comb line frequency was achieved by modulating the diode current of the ECDL. OBPF: optical bandpass filter.

6.4. Out-of-Loop Characterization of Fully-Stabilized Chip-Scale Optical Frequency Comb Synthesizer

For offset frequency above 10 kHz, the phase noise of the fully stabilized comb spacing is better than that of the 18 GHz local oscillator used for downmixing the electronic signal. The measurement is instrument limited to the level of ≥ -108 dBc/Hz from 10 kHz to 300 kHz and −130 dBc/Hz at 1 MHz. It is therefore informative to calculate the theoretical limit of the phase noise at large offset frequencies and compare with the measurement. Using the equations with the pump-resonance detuning of $\frac{T_R \gamma^2}{D}$ derived in Ref. [128] and assuming $\left(\frac{f}{\gamma}\right)^2 \ll 1$, we obtain the lower limit of the phase noise expressed as

$$\boldsymbol{\mathcal{L}(f) \approx \frac{2\sqrt{2}\pi\hbar c n_2}{n_0^2 V_0} Q^2 \left[\frac{23}{24} + \left(\frac{4+\pi^2}{96\pi^2}\right)\frac{\gamma^2}{f^2}\right]} \quad \textbf{(6-1)}$$

where $D \equiv (\omega_{m+1} - \omega_m) - (\omega_m - \omega_{m-1})$, Q, n_0, n_2, V_0, 2γ, and f are the non-equidistance of the cold cavity modes, quality factor, linear refractive index, nonlinear refractive index, mode volume, FWHM resonance linewidth, and frequency offset from the 17.9 GHz carrier respectively. For our spiral microresonator, the estimated phase noise at 1 MHz is −148 dBc/Hz and it grows quadratically with the inverse of the offset frequency. The estimated phase noise reaches −108 dBc/Hz at 10 kHz and starts to exceed the noise level of the 18 GHz local oscillator, matching the experimental observations. Of note, Eq. $\boldsymbol{\mathcal{L}(f) \approx \frac{2\sqrt{2}\pi\hbar c n_2}{n_0^2 V_0} Q^2 \left[\frac{23}{24} + \left(\frac{4+\pi^2}{96\pi^2}\right)\frac{\gamma^2}{f^2}\right]}$ (6-1) derivation requires a single-moded microresonator and the Kerr microcomb to be mode-locked, and hence only serves as a lower limit to our measurements.

Figure 6-7b inset plots the Allan deviations of the comb spacing under different conditions. After the comb spacing is downmixed with the 18 GHz local oscillator, the beat frequency is counted with a Λ-type frequency counter. Allan deviation is then estimated using the equation $\sigma_A(\tau) = \sqrt{\frac{1}{M}\sum_{i=1}^{i=M}\frac{(\bar{y}_{i+1}-\bar{y}_i)^2}{2}}$, where τ, $\bar{y}_i$, and $M = min\left\{60, \left[\frac{1000}{\tau}\right]\right\}$ are the gate time, the fractional frequency, and the number of samples respectively [132]. Free running, the Allan deviation increases as $\tau^{1/3}$ as the result of technical noise including the pump wavelength drift and the fluctuating ambient temperature (black open squares). Pump frequency stabilization reduces the increase of Allan deviation over the gate time, but interestingly the level of Allan deviation remains unimproved because of the additional pump power fluctuation from the employed pump frequency control (red semi-open squares). With pump power feedback control, the active stabilization on the comb spacing improves the long-term stability by six orders of magnitude, reaching 3.6 $\text{mHz}/\sqrt{\tau}$ (blue closed squares). The residual comb instability is limited by the microwave synthesizer and close to the counter limit at 1 second gate time.

To assess the uncertainty of the fully stabilized Kerr microcomb, we use the Menlo FFC as the calibration standard and measure the out-of-loop frequencies of forty-six Kerr microcomb lines around 1576 nm (Figure 6-9a) by beating each comb line with the adjacent FFC mode as shown in Figure 6-1a. When the comb spacings of the FFC and Kerr microcomb are made unequal, the beat frequencies should strictly follow the relationship of

$$\boldsymbol{f_{beat}^{n} = \delta + n\left(f_{R,KC} - \left\lfloor\frac{f_{R,KC}}{f_{R,FFC}}\right\rfloor f_{R,FFC}\right)} \quad \textbf{(6-2)}$$

where δ is the beat frequency at the pump mode, $f_{R,KC}$ is the Kerr microcomb spacing, and $f_{R,FFC}$ is the FFC comb spacing. Deviation from this expression poses an upper bound on the frequency uncertainty of the Kerr microcomb. Figure 6-9b shows two example histograms of the frequency counting measurement. 600 counts are accumulated at 1 second gate time for the statistical analysis and the Gaussian curve fitting is implemented to derive the mean values and standard deviations. Counting results on all forty-six comb lines are shown in Figure 6-9c. The mean values of the comb frequencies stray from the ideal with a 190 mHz peak-to-peak deviation and a 50 mHz standard deviation. The relative frequency uncertainty of the stabilized chip-scale frequency comb is thus calculated at 2.7×10^{-16}, referenced to the optical carrier at 188 THz. Of note, the 17.9 GHz comb spacing generated directly from the microresonator is compatible for high resolution astrospectrography and thus sophisticated Fabry-Perot (FP) filtering cavities, which limits the precision of state-of-the-art astrocomb [9,10,125], is circumvented. Due to the residual FP cavity dispersion and fluctuations of the FP cavity resonance, leading to changes in the extraneous-line suppression, the uncertainty of the astrocomb line frequency is typically degraded to kHz level [9,10,125]. The uncertainty, σ, then translates linearly to the systematic error, ε, in astrophysical velocity measurements with an approximate relation of $\varepsilon \cong \frac{\sigma}{f_p} \cdot c$ [9]. Thus, the 50 mHz frequency uncertainty of the Kerr microcomb can potentially improve the precision in astrophysical radial velocity measurements by orders of magnitude.

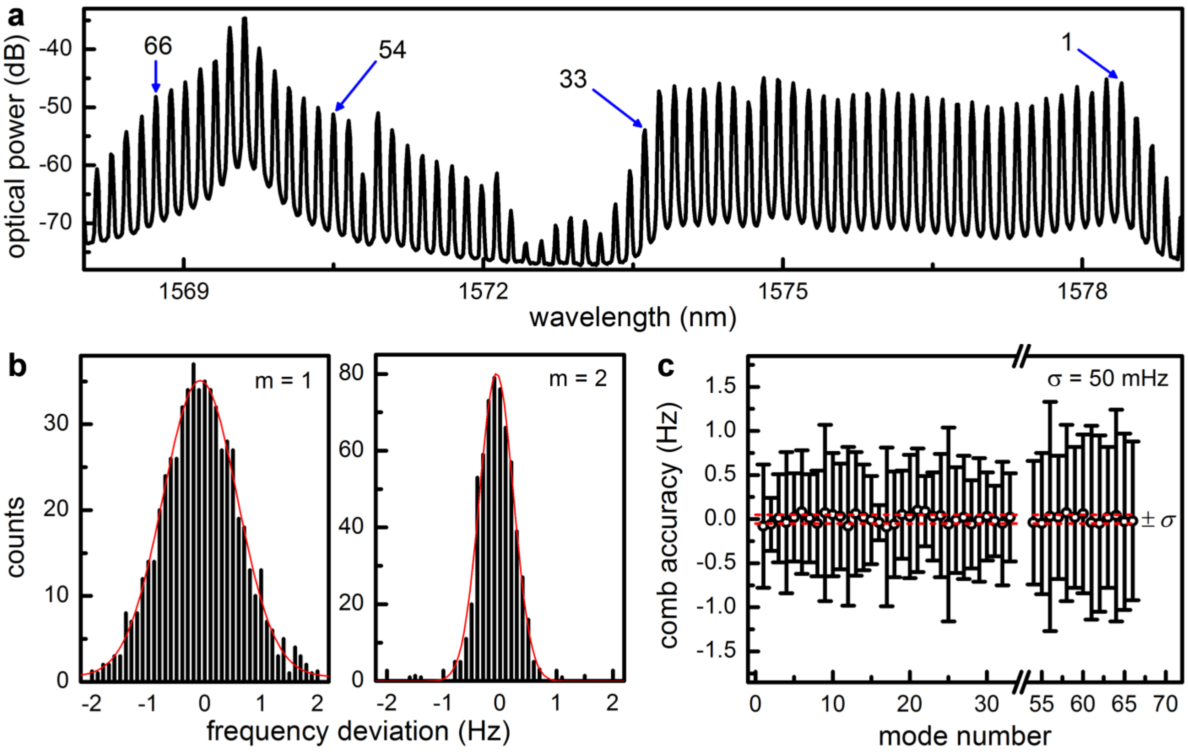

Figure 6-9. Out-of-loop characterization of the fully-stabilized chip-scale optical frequency comb.

(a) To quantify the uncertainty of the stabilized chip-scale optical frequency comb, each of the comb lines from 1578.4 to 1573.6 nm (*m*=1 to *m*=33) and from 1570.5 to 1568.7 nm (*m*=54 to *m*=66) is mixed with the fiber laser frequency comb and the beat frequency is counted with a gate time of 1 second. The beat frequencies should change progressively by Δ, where $\Delta = f_{R,KC} - \lfloor f_{R,KC}/f_{R,FFC} \rfloor f_{R,FFC}$, and the deviation from this relationship poses an upper bound on the frequency uncertainty of the chip-scale optical frequency comb. **(b)** Example histograms of the frequency counting measurement on the 1st and 2nd modes (*m*). 600 counts are accumulated for the statistical analysis. The red lines are the Gaussian fits to the histograms. **(c)** Counting results on the optical frequencies of 46 comb lines. The centroid of the comb frequencies stray from the ideal with a 190 mHz peak-to-peak deviation and a 50 mHz standard deviation. The frequency relative uncertainty of the fully stabilized chip-scale optical frequency comb is thus calculated at 2.7×10^{-16}, referenced to the 188 THz optical carrier.

6.5. Summary

This chapter discusses the first fully stabilized CMOS-compatible solid-state optical frequency comb. Based on the silicon nitride spiral resonator, a native 18 GHz Kerr microcomb is generated and its single-sideband phase noise reaches the instrument limited floor of -130 dBc/Hz at 1 MHz offset. The comb's two degrees of freedom, one of the comb line frequencies and the comb spacing, are phase locked to a known optical reference and a microwave synthesizer respectively, reaching an instrument limited residual comb spacing instability of $3.6\ \mathrm{mHz}/\sqrt{\tau}$. Forty-six Kerr microcomb lines are compared with the current benchmark FFC and the relative frequency uncertainty of the fully stabilized Kerr microcomb is measured down to 2.7×10^{-16}. The reported system is a promising scalable platform for coherent Raman spectroscopy, high-precision optical clockwork, high-capacity coherent communications, arbitrary waveform generation, and astrophysical spectrography.

Chapter 7.

Globally Stable Microresonator Turing Pattern Formation for Coherent High-Power THz Radiation On-Chip

In nonlinear microresonators driven by continuous-wave (cw) lasers, Turing patterns have been studied in the formalism of Lugiato-Lefever equation with emphasis on its high coherence and exceptional robustness against perturbations. Destabilization of Turing pattern and transition to spatio-temporal chaos, however, limits the available energy carried in the Turing rolls and prevents further harvest of their high coherence and robustness to noise. Here we report a novel scheme to circumvent such destabilization, by incorporating the effect of local mode hybridizations, and attain globally stable Turing pattern formation in chip-scale nonlinear oscillators with significantly enlarged parameter space, achieving a record high power conversion efficiency of 45% and an elevated peak-to-valley contrast of 100. The stationary Turing pattern is discretely tunable across 430 GHz on a THz carrier, with a fractional frequency sideband non-uniformity measured at 7.3×10^{-14}. We demonstrate the simultaneous microwave and optical coherence of the Turing rolls at different evolution stages through ultrafast optical correlation techniques. The free-running Turing roll coherence, 9 kHz in 200 ms and 160 kHz in 20 minutes, is transferred onto a plasmonic photomixer for one of the highest power THz coherent generation at room-temperature, with 1.1% optical-to-THz power conversion. Its long-term stability can be further improved by more than two orders of magnitude, reaching an Allan deviation of 6×10^{-10} at 100 s, with a simple computer-aided slow feedback control. The demonstrated on-chip coherent high-power Turing-THz system is promising to find applications in astrophysics, medical imaging, and wireless communications.

7.1. Introduction

7.1.1. Revisit of Kerr Frequency Comb Evolution Dynamics

The spontaneous formation of stationary periodic patterns from homogenous background firstly elucidated by Turing has served as the basis for developmental biology morphogenesis, chemical kinetics far-from-equilibrium, and the formation of fractals and chaos in nonlinear dynamics [133–135]. Of both conceptual importance and practical interest, optical Turing pattern formation has been theoretically proposed and investigated in cw-laser-pumped Kerr-active microresonators [85,86,136], with emphasis on its high coherence and exceptional robustness against perturbations. Generally the Kerr-active microresonator is designed to possess anomalous group velocity dispersion (GVD) for convenient phase matching fulfillment and the formation dynamics of the spontaneous patterns can be described by the Lugiato-Lefever equation [137]. As the driving laser is frequency tuned into the cavity resonance from the blue side, stable Turing rolls first spontaneously emerge from the background, then quickly destabilize into spatio-temporal chaos [96,138], and eventually transition into dissipative Kerr solitons [20,76,108,139,140] or Kerr frequency comb [72,141,142] (Figure 7-1).

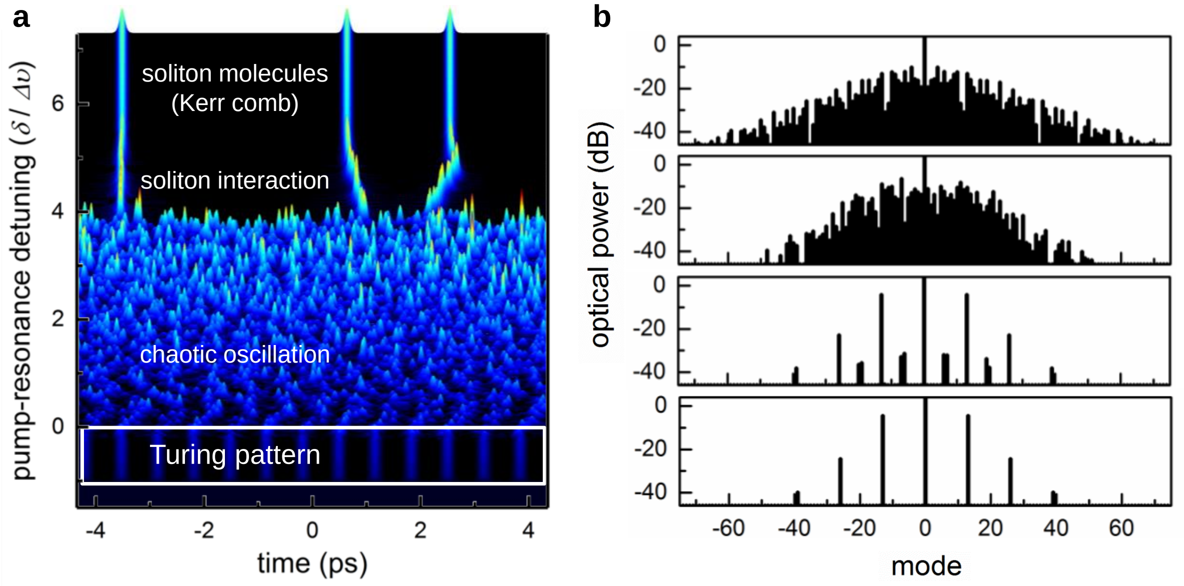

Figure 7-1. Evolution dynamics of a Kerr frequency comb under 100 mW on-chip power in (a) temporal domain and (b) spectral domain in a 116 GHz microresonator. The horizontal axis is the azimuthal direction, mapped with cavity round-trip time; the vertical axis is the pump-resonance detuning, normalized with cavity linewidth. A typical evolution includes Turing pattern, chaotic oscillation, soliton interaction and soliton or soliton molecules. Spontaneous Turing pattern, after formed, is quickly collapsed into spatio-temporal chaos, and eventually transformed into soliton molecules with a proper scan protocol of pump detuning.

7.1.2. Stability Map of Turing Comb in Anomalous Dispersion

We note that the Turing roll in this dispersion regime, despite its optimally coherent properties [143], only exists in a limited phase space and its quick destabilization into chaos limits the attainable power conversion efficiency (Figure 7-2), preventing further harvest of the high coherence and the noise robustness of the Turing pattern.

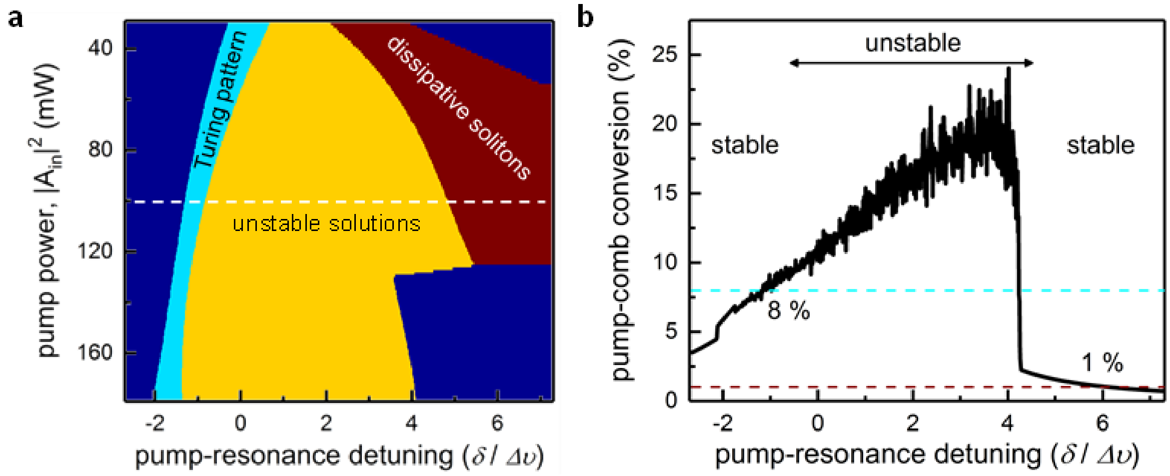

Figure 7-2. Stability diagram and pump-to-comb power conversion.

(a) Stability diagram of the Turing pattern in the anomalous GVD regime. Light blue: region of stable Turing pattern; yellow: region of breathers and spatio-temporal chaos; red: region of soliton and soliton molecules. The comb evolution dynamics along the dashed line is shown in Figure 7-1). (b) Pump-to-comb power conversion efficiency along the white dashed line in (a), showing only 8% maximum power conversions to Turing pattern before destabilization and transition to chaos happens.

7.2. Realization of Preventing Turing Comb Destabilization with high-efficiency conversion

7.2.1. Expanding Turing Pattern Stability Zone with Mode Hybridization Mediated Phase Matching

To expand the stability zone and attain higher power conversion, we approach the spontaneous Turing pattern formation in a distinctly different way. Our Kerr-active microresonator is designed to possess a large globally normal GVD of 100 fs^2/mm (Figure

7-3) and thus phase matching is strictly forbidden unless local dispersion anomalies are introduced to the system, providing additional GVD to balance the nonlinearity locally. In our high *Q* microresonator (loaded quality factor of 3.7×10^5), such anomalies result from the hybridization of two transverse modes (TM_{11} and TM_{21}) with distinct free spectral ranges (FSRs) when their resonant frequencies are in the vicinity of each other [32,87,92,118,144,145]. The spectral position of the mode hybridization defines the Turing pattern formation dynamics and it can be changed by the design of the FSR difference. As the balance between the GVD and the Kerr nonlinearity is only fulfilled locally in the confined spectral range where mode hybridization occurs, sub-comb growth and subsequent destabilization of the Turing pattern is avoided (Figure 7-4). By enabling the deeper driving-into-resonance without transition into chaos or soliton states, the conversion efficiency from pump to Turing pattern can thus be significantly enhanced in our system. The mode hybridization mediated phase matching – by adjusting the relative frequency between the pump mode and the mode hybridization position – further enables the repetition rate of the Turing roll to be discretely tunable. Moreover, the Turing roll spectra can exhibit controllable asymmetry through registering the pump mode on different sides of the first local-mode hybridization region ε_1 (Figure 7-9a).

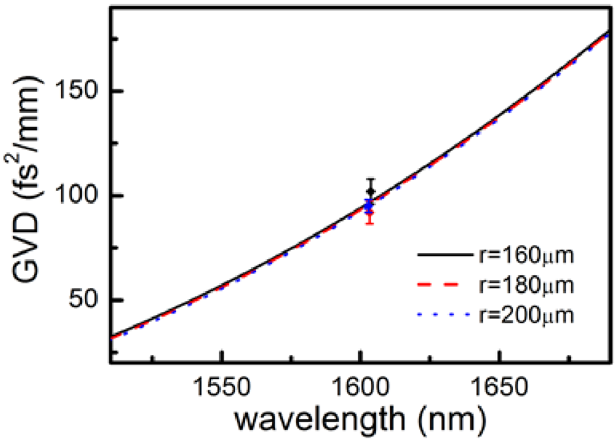

Figure 7-3. Group velocity dispersion (GVD) of microring resonators for spontaneous Turing pattern formation, featuring large normal GVDs of +100 fs^2/mm.

The ring radius is designed to be large enough (more than 160 μm) such that the bending-induced dispersion is negligible. Measured GVDs at 1603 nm (circles with error bars) show good agreements with the numerical modeling. Inset: scanning electron micrograph of the nonlinear ring resonator.

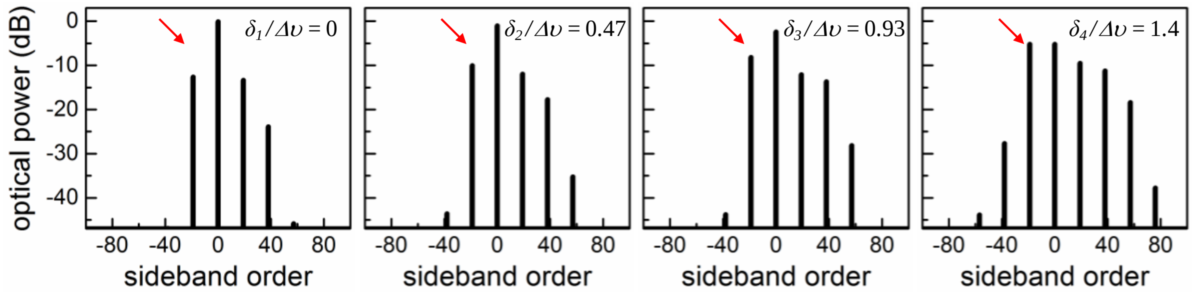

Figure 7-4. Simulation of the Turing roll in the normal dispersion microresonator (1300 fs^2), where the Turing roll is excited by local mode hybridization.

The red arrow points to the mode where local dispersion disruption is introduced in the Lugiato-Lefever model. It shows an apparent asymmetry and can be tuned further into resonance without triggering the sub-comb growth and the associated Turing pattern destabilization, expanding the stability zone and opening the route to harness Turing pattern's high coherence and exceptional robustness at high optical powers. Note that the pump-resonance detuning used in the simulation is referenced to the cold cavity resonance frequency.

Here we demonstrate for the first time the scheme of incorporating the mode hybridization effect to attain globally stable microresonator Turing patterns in chip-scale nonlinear nitride cavities with significantly enlarged parameter space, achieving an unprecedented pump depletion and a record high power conversion efficiency of 45% with an elevated peak-to-valley contrast of 100. We interrogate the commensurate and coherent nature of the spontaneous dissipative structure with ultrafast optical intensity autocorrelation, microwave spectral noise analysis, and heterodyne beating against a benchmark fiber frequency comb. The fractional frequency sideband non-uniformity of the Turing pattern is measured at 7.3×10^{-14}, with a short-term (200 ms sweep time) linewidth of 9 kHz and a long-term (over 20 minutes) fluctuation of 160 kHz in the free-running mode. The long-term stability can be further improved by more than two orders of magnitude, reaching an Allan deviation of 6×10^{-10} at 100 s, with a simple computer-aided slow feedback control. Towards THz applications, we then transfer the Turing pattern optical coherence to the THz carrier through a plasmonic ErAs:InGaAs photomixer, generating up to 600 μW THz radiation power at room temperature. The carrier frequency is discretely tunable over a broadband from 1.14 THz to 1.57 THz. The demonstrated coherent high-power Turing-THz system offers the potential to be the room temperature on-chip THz local oscillator for astrophysics, medical imaging, and wireless communication [146–151].

Here a TM-polarized cw laser with an optical power of 29.5 dBm is frequency tuned from the blue side of the cavity resonance to trigger the Turing pattern formation. The measured spectra of the spontaneous Turing patterns generated from ring resonators with different radii are shown in Figure 7-9a, with the pump illustrated in blue and the mode hybridization positions labeled as red dashed lines. Despite very similar GVD (β_2) from different radii ring resonators, the Turing patterns show spectral shapes distinct from each other. Specifically, the spectral lines on the side of the first mode hybridization position are suppressed due to the increasing phase mismatch associated with the mode hybridization induced local dispersion disruption. With the first sideband pair ($m = \pm 1$) phase matched due to the additional contribution from the mode hybridization on mode 1, then the phase matching condition can be written as:

$$\Delta k(2\omega_0 - \omega_1 - \omega_{-1}) = \beta_2\Delta^2 + \gamma P_{int} - \varepsilon = 0\ ,$$

where ε represents the contribution from the mode hybridization, Δ the Turing roll repetition rate, γ the nonlinear Kerr coefficient, and P_{int} the intracavity power. Here $k_1 = k_0 + \beta'\Delta + \frac{\beta_2}{2}\Delta^2 + \varepsilon$, and $k_m = k_0 + \beta'(m\Delta) + \frac{\beta_2}{2}(m\Delta)^2$, where β' is the group velocity. Then the phase matching condition for the first cascaded FWM on *either* side of the pump can be written as:

$$\Delta k(2\omega_1 - \omega_2 - \omega_0) = \beta_2\Delta^2 + \gamma P_{int} + 2\varepsilon = 3\varepsilon$$

$$\Delta k(2\omega_{-1} - \omega_0 - \omega_{-2}) = \beta_2\Delta^2 + \gamma P_{int} = \varepsilon\ .$$

The phase mismatch on the side of the mode crossing position is three times larger than the other process and thus the symmetry of the Turing roll spectra is broken. Similar symmetry breaking by mode hybridization has also been demonstrated in the microwave photonics recently [152]. Turing roll repetition rates also show dramatic variations, ≈ 640 GHz in the 180 μm radius ring and ≈ 1.72 THz in the 160 μm and 200 μm rings, that cannot be solely explained by the change in the cavity round-trip time. These features are direct consequences of the unique phase matching configuration employed in our design, with critical roles in the efficient coherence transfer from Turing pattern to THz radiation detailed in Chapter 7.5. Note that, the mode hybridization induced local dispersion disruption ε can be dynamically tuned by changing the temperature of the microresonator, thereby providing an additional dimension to control the Turing pattern formation dynamics. The dynamics is detailed in Session 7.2.2.

7.2.2. Dynamic Tuning of Mode Hybridization by Device Temperature Control

The two transverse mode families can be solved by 3D finite-element analysis [153], as shown in Figure 7-5. *Mode 0* is where the resonance frequencies of the two mode families (ω_{11} and ω_{12}) cross each other. The exact crossing point is determined by the distinct free spectral ranges (FSRs) of the two transverse modes (TM_{11} and TM_{21}), and it can be tuned by design of the waveguide geometry. Here without considering modal interaction effect, as Figure 7-5b shows, the frequency difference can be simply expressed as $\Delta_{\mathrm{eig}}/2\pi = (\omega_{11} - \omega_{12})/2\pi$ and it has a linear relationship with the mode number.

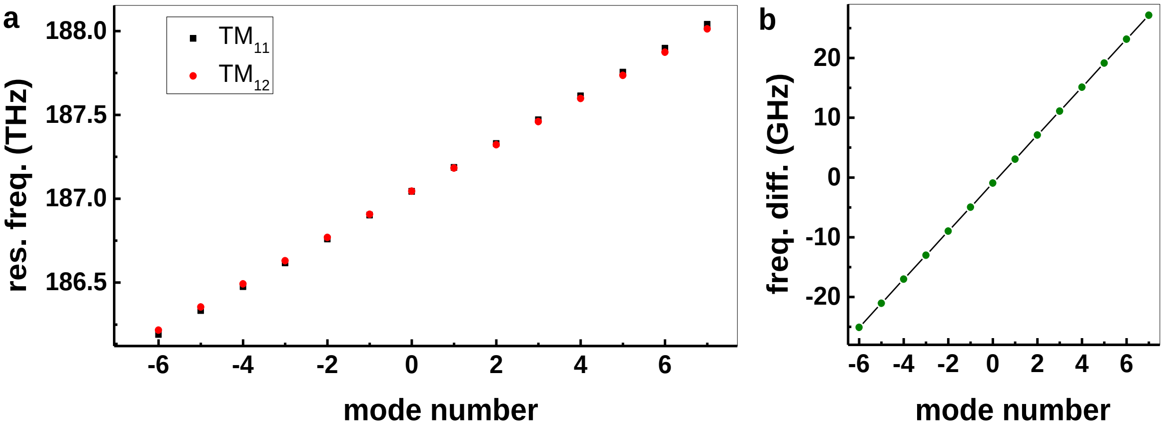

Figure 7-5. Numerically modeled cavity resonances and mode crossing without mode coupling effect.

(a) Resonance frequencies of TM_{11} ($\omega_{11}/2\pi$, black square) and TM_{12} ($\omega_{12}/2\pi$, red dot) at the temperature of 60 °C. (b) Frequency difference between TM_{11} and TM_{12} mode, *i.e.*, $\Delta_{\mathrm{eig}}/2\pi$, showing a linear relationship with mode number. The crossing point between the two mode families is a function of FSR difference and can be tuned by design of the waveguide geometry.

In real devices, however, the two modes can couple with each other when their resonance frequencies are close, owing to imperfections in material growth, waveguide cross-section, and bending geometry. Figure 7-6a plots the experimentally measured and fitted resonance frequencies for the two modes at the temperature of 60 ^{o}C. Figure 7-6b shows the frequency differences calculated from the measurements at two different temperatures of 60 ^{o}C and 70 ^{o}C respectively; at *mode 0*, the cavity mode experiences a frequency shift Δ_{m}, leading to an offset from the otherwise linear relationship (blue lines) between the frequency difference and the mode number. Note that, Figure 7-6c shows that Δ_{m} is inversely proportional to Δ_{eig} and their exact values are temperature dependent. Both relationships are consistent with the coupled mode theory elaborated later in details.

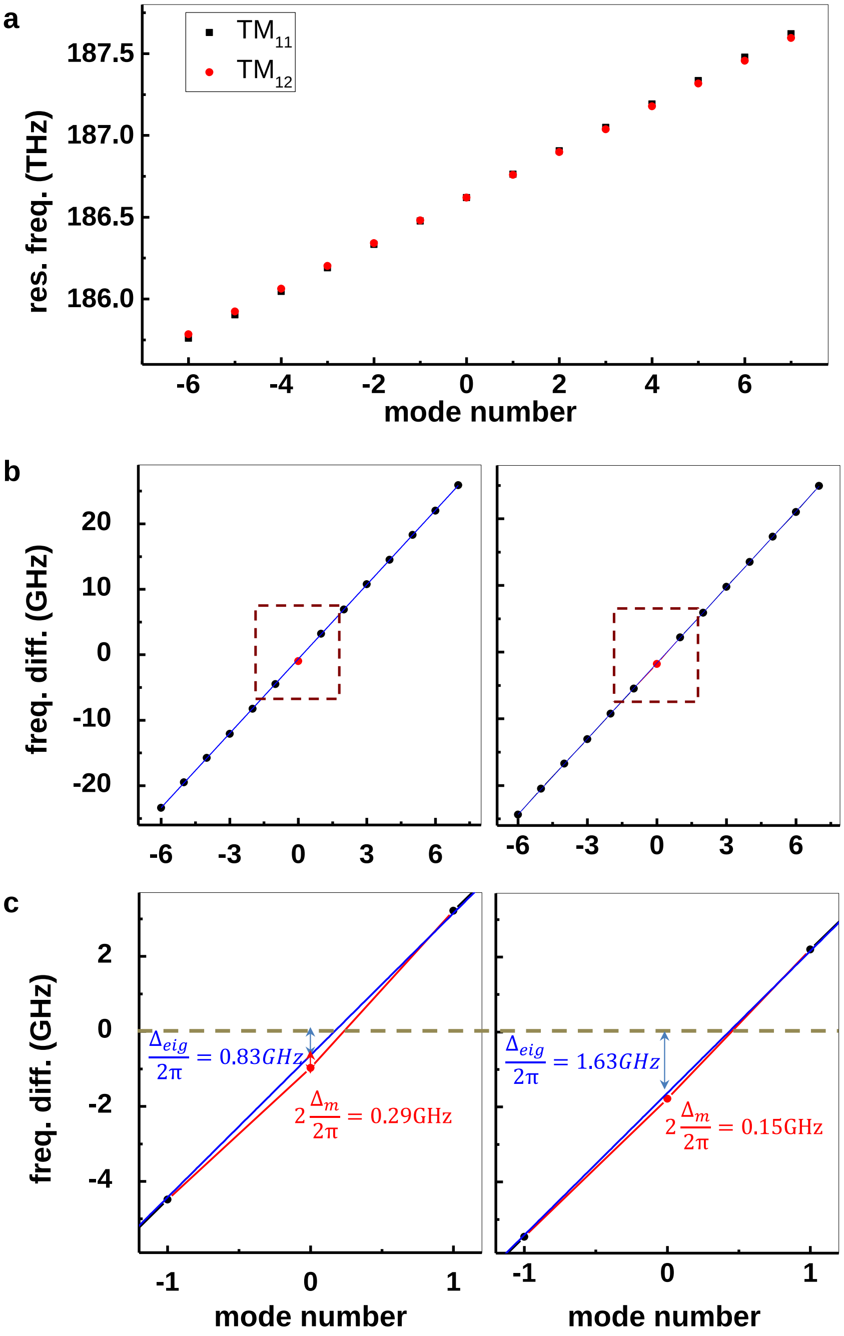

Figure 7-6. Experimentally measured two transverse mode families with mode coupling effect under different temperatures.

(a) Experimentally measured resonance frequencies of TM_{11} (black square) and TM_{12} (red dot) at the temperature of 60 °C. (b) Frequency difference between TM_{11} and TM_{12} at 60 °C (left) and 70 °C (right). (c) Zoom-in frequency difference around *mode 0*. The linearly fitted value at *mode 0* is the frequency difference between the two eigenmodes $\Delta_{\mathrm{eig}}/2\pi$, 0.83 GHz at 60 °C and 1.63 GHz at 70 °C, without considering the modal interaction effect; the additional offset from the measurement (red dot) shows the modal frequency shift induced by mode hybridization $\Delta_{\mathrm{m}}/2\pi$, 0.29 GHz at 60 °C and 0.15 GHz at 70 °C.

From the coupled mode theory, Δ_{eig} and Δ_{m} have a fixed relationship in a given device $\Delta_{\mathrm{m}} = -\frac{\kappa^2}{\Delta_{\mathrm{eig}}}$ [20,92], where κ is the mode interaction constant. Note that, while it is very challenging to control the mode interaction constant, adjusting Δ_{eig} through either waveguide design or dynamic temperature tuning is an effective way to engineer the overall effect of mode hybridization. When the magnitude of temperature tuning is sufficiently high, it can even shift the mode hybridization position, a phenomenon that is later utilized for discrete tunability of THz frequency. A summary of all measured Δ_{eig} at the temperature ranging from 30 °C to 90 °C are shown in Figure 7-7 (red dots). An analytic fit is performed based on the relation $\mathrm{R_0}(1 + \alpha\Delta\mathrm{T})\mathrm{n_0}\left(1 + \frac{\frac{1}{\mathrm{n_0}}\mathrm{dn}}{\mathrm{dT}}\Delta\mathrm{T}\right)\omega = \mathrm{mc}$ [153], where $\mathrm{R_0}$ is the original ring radius, $\mathrm{n_0}$ the original index, $\Delta\mathrm{T}$ the temperature change, m the mode number, $\frac{\mathrm{dn}}{\mathrm{dT}}$ the thermal optic coefficient, and α the thermal expansion coefficient [154]. A better fit to the measurement data points (blue line) can be obtained by adjusting $\frac{\mathrm{dn}}{\mathrm{dT}}$ from 2.45×10^{-5} / °C as reported in the literature [154] to 1.76×10^{-5} / ˚C. To further validate our results, we calculate the mode interaction constant κ as a function of temperature using the measured Δ_{eig} and Δ_{m}. As expected, κ is practically temperature invariant from 50 °C to 70 °C, with a mean value of 2.1 GHz and a standard deviation of 2 % (Figure 7-8).

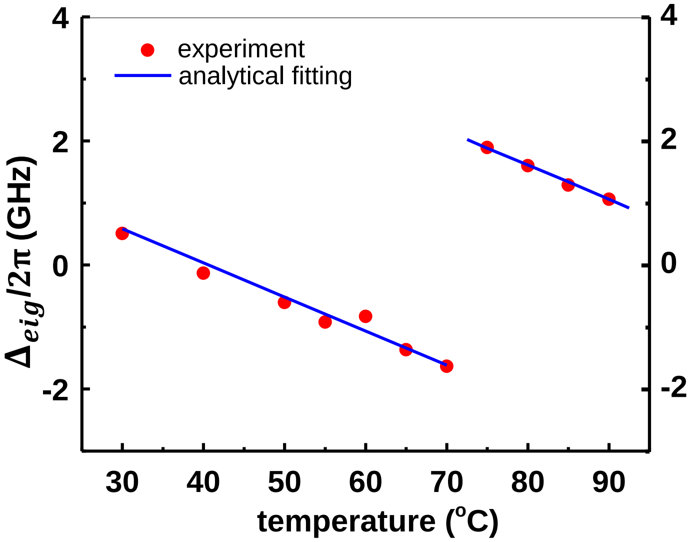

Figure 7-7. Measured eigenmode frequency difference Δ_{eig} with respect to device temperature tuning with a fitted linear relationship.

Tuning of Δ_{eig} through chip temperature control changes the mode hybridization effect. Δ_{eig} shows a linear relationship with temperature. When the chip temperature is increased to more than 75 °C, the mode hybridization effect shifts to the adjacent mode.

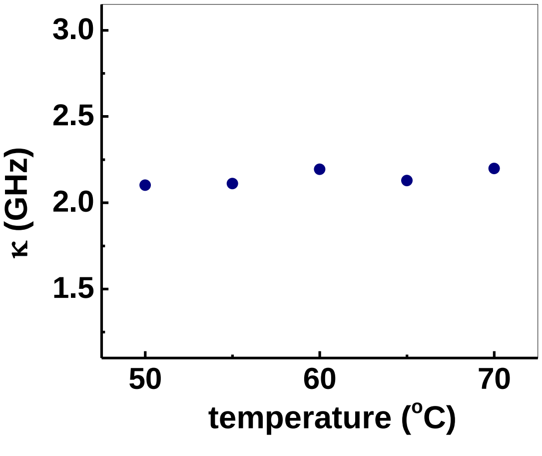

Figure 7-8. Mode interaction constant κ derived from experimental measurements.

Mode interaction constant κ is derived using the relation $\Delta_{\mathrm{m}} = -\frac{\kappa^2}{\Delta_{\mathrm{eig}}}$. Across all temperatures, the κ is consistently 2.1 GHz with 2% standard deviation.

To complete this discussion, we quantitatively examine the mode hybridization mediated phase matching as outlined in Session 7.2.1. The wavenumber with mode hybridization effect ($\mathrm{k_1}$) and without mode hybridization effect ($\mathrm{k_{1o}}$) can be written as:

$$\mathrm{k_1 = k_0 + \beta'(\Delta + \Delta_m) + \frac{\beta_2}{2}(\Delta + \Delta_m)^2}$$

$$\mathrm{k_{1o} = k_0 + \beta'\Delta + \frac{\beta_2}{2}\Delta^2}$$

hence the phase mismatch induced by mode hybridization can be expressed as $\mathrm{\varepsilon = k_1 - k_{1o} \approx \beta'\Delta_m + \beta_2\Delta \cdot \Delta_m}$. Consequently, a modal frequency shift of $\mathrm{\Delta_m \approx \frac{\beta_2\Delta^2 + \gamma P_{int}}{\beta'}}$ is required to satisfy the phase matching condition, $\mathrm{\Delta k(2\omega_0 - \omega_1 - \omega_{-1}) = \beta_2\Delta^2 + \gamma P_{int} - \varepsilon = 0}$. Plugging in the measured $\mathrm{\Delta_m/2\pi}$, $\mathrm{\Delta/2\pi}$, β_2, β', and γ, we find that the required intra-cavity power of 15 W is in a good agreement with the experiment.

7.2.3. Globally Stable Turing Pattern Formation

We focus the analysis on the results generated from the 160 μm radius ring because of its energy concentration in the wavelength range shorter than 1570 nm, overlapping better with the spectral response of our plasmonic photomixer discussed later. Figure 7-9b and c shows the pump and total transmitted intensities, measured simultaneously for different detunings. The pump transmission shows a triangular tuning curve with a strong dip from normalized unity into ≈ 10% of the original transmission, while total transmission shows only a small drop from 48% to 41% – this provides the evidence of the efficient total energy transfer from the pump into the complete Turing pattern sidebands. To examine this further, Figure 7-9d plots the corresponding Turing roll spectra at different detuning stages: stable spontaneous Turing pattern are observed without any sign of destabilization at all detunings.

The power conversion efficiency, defined as the integrated power of the output Turing roll divided by the on-chip pump power, reaches as high as 45% at the stage III. Closer to resonance at the stage V, an even stronger pump depletion is achieved, with the pump intensity 2-dB lower than even the first modulation sidebands.

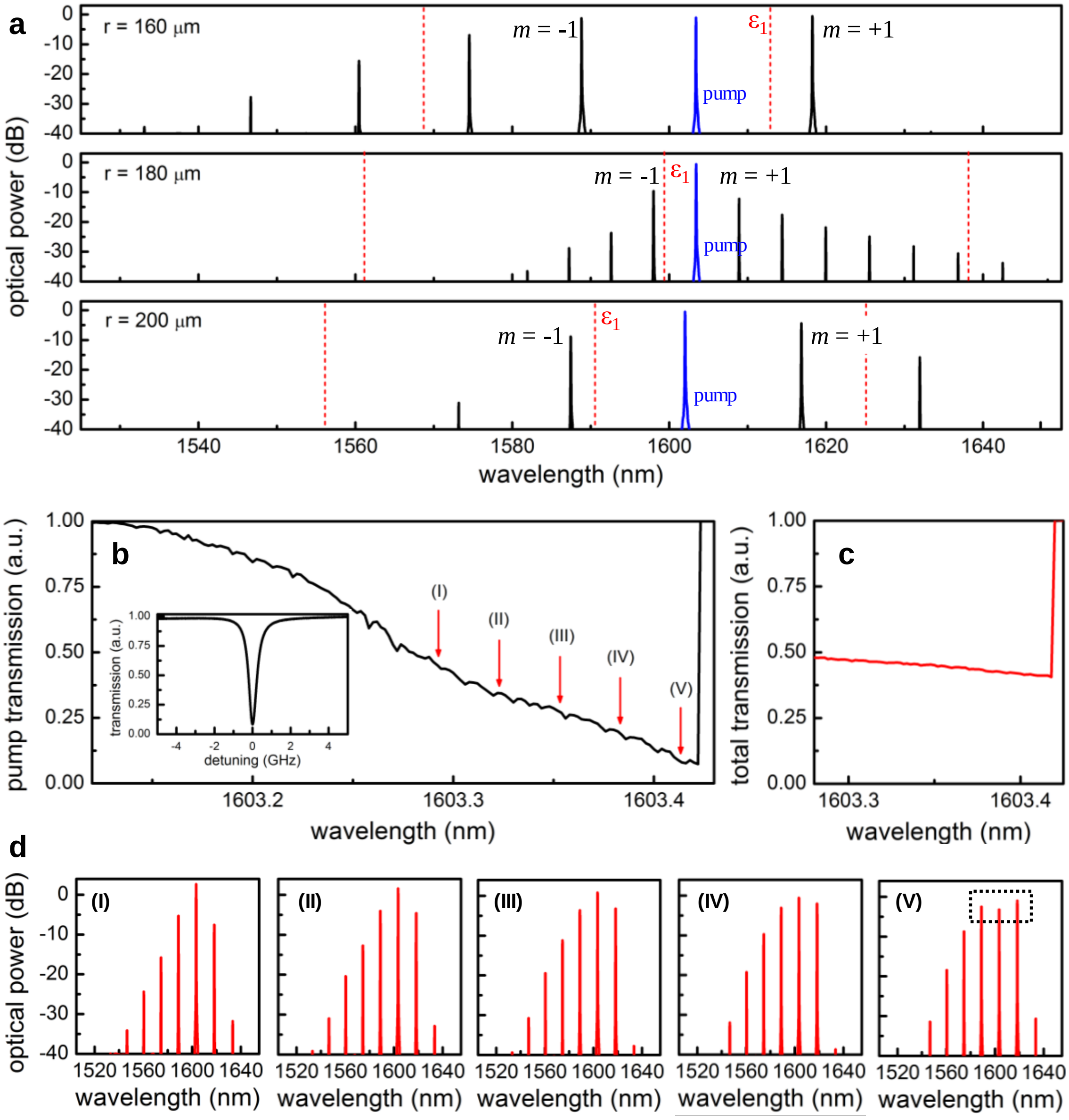

Figure 7-9. Turing rolls generated in microring resonators.

(a) Turing rolls generated from ring resonators with different radii. Even though the GVD of the ring resonators differ by less than 2 fs^2/mm, the TM_{11}-TM_{21} mode hybridization positions (red dashed lines) with respect to the pump (blue lines) shift due to the change in the ring radii, resulting in abrupt dispersion variations locally and very different spontaneous Turing patterns. The Turing roll repetition rates are 1.72 THz (12×FSR) for the 160 μm radius ring, 0.64 THz (5×FSR) for the 180 μm radius ring, and 1.72 THz (15×FSR) for the 200 μm radius ring. (b) Pump-cavity transmission as a function of the pump wavelength, labeling the detunings where different Turing roll stages are generated. Inset: The cold resonance of the pump mode, measuring a loaded Lorentzian linewidth of 500 MHz and a loaded quality factor of 3.7×10^5. (c) Total cavity transmission as a function of the pump wavelength in the range where Turing roll is generated. Compared to the pump-cavity transmission, the total cavity transmission shows a less apparent decrease as the pump is tuned into the resonance, confirming an efficient power conversion from the pump to the generated Turing lines. (d) Example Turing roll spectra at different stages. At stage V, even a highly depleted pump close to the resonance is observed in the measurement, illustrated in the dashed box.

Note that, here the pump-to-comb power conversion efficiency is defined as:

$$\eta = \frac{\int_0^T (I_{out} - I_{bkg})dt}{T}$$

as illustrated in Figure 7-10. In the calculation, we only consider the optical power of the Turing pattern carried by the output bus waveguide. This definition of power conversion efficiency, rather than slope efficiency or internal efficiency, is adopted in this manuscript because it provides a more transparent measure to calculate the total available power for real-world applications.

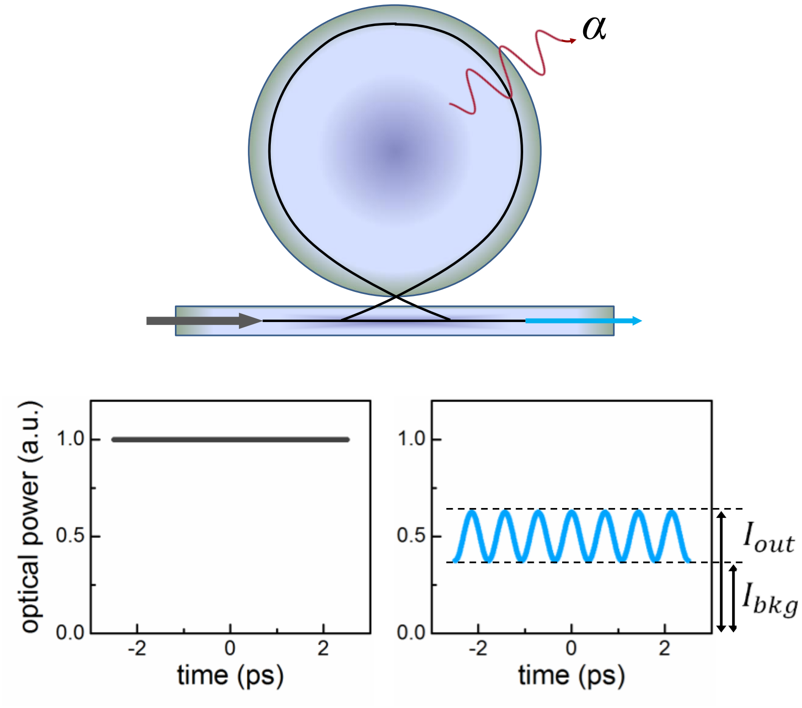

Figure 7-10. Illustration of external pump-to-comb conversion efficiency.

7.3. Terahertz Frequency Coherence Characterization

To investigate the temporal structure of the Turing patterns at different evolving stages, we conduct a series of ultrafast optical intensity autocorrelation (IAC) measurements, as shown in Figure 7-11a. At all the stages, stable and strong quasi-sinusoidal oscillations are each observed. While pumping closer to resonance results in monotonic increase in the pump depletion (Figure 7-9d), counterintuitively the IAC traces show a discernible minimum background between stage II and stage III. As elaborated later, it is a direct consequence of strong pump depletion. At stage III, a peak-to-valley intensity contrast ratio of more than 100 is achieved, as shown in Figure 7-12. We perform extensive measurements to examine the coherence of the spontaneous Turing formation, illustrated in Figure 7-11b to e. The RF amplitude noise spectra of the Turing pattern up to 3 GHz, six times the cavity linewidth, shows an absence of RF peaks and a noise level at the instrumentation detection background limit, indicative of the existence of a single Turing roll family with commensurate repetition rates (Figure 7-11b).

We further heterodyne beat the Turing sidebands (m = ± 1 and pump) against a benchmark fiber frequency comb (see Appendix II) and perform ratio counting of the sidebands to interrogate the frequency uniformity, which sets the fundamental limit on the coherence transfer from the Turing pattern (Figure 7-11c). When the Turing roll repetition rate is made non-divisible by the fiber frequency comb spacing, the beat frequencies of consecutive sidebands will be an arithmetic sequence. Namely, $\delta_2 = \delta_1 + \Delta = \delta_0 + 2\Delta$. Here we make the common difference, Δ, to be 1 MHz. Ideally, the ratio between $\delta_2 - \delta_0$ and $\delta_1 - \delta_0$, R, should be 2 and deviation from this ratio, ε_R, is a measure of the sideband frequency non-uniformity, $\varepsilon = \varepsilon_R \cdot \Delta$. Excellent sideband uniformity of the Turing pattern is observed at all evolving stages with the average non-uniformity measured at 125 mHz, 7.3×10^{-14} when referenced to the Turing pattern repetition rate at 1.72 THz (Figure 7-11c). Figure 7-11d next shows the self-heterodyne beat note of the first sideband (see Appendix III), demonstrating the Turing lines down to a pump-coherence-limited linewidth of 500 kHz. The linewidth measurements independently confirm the good coherence of the Turing rolls at all detunings. Figure 7-11e also shows the real-time power monitoring of the four strongest sidebands. All sidebands present similar intensity noise of less than 1% (integrated from 100 Hz to 100 MHz) and no cyclic energy exchange between sidebands is observed, excluding the possibility of breathing dynamics with conserved total power and supporting the evidence of stationary Turing pattern formation with extensive stability zone.

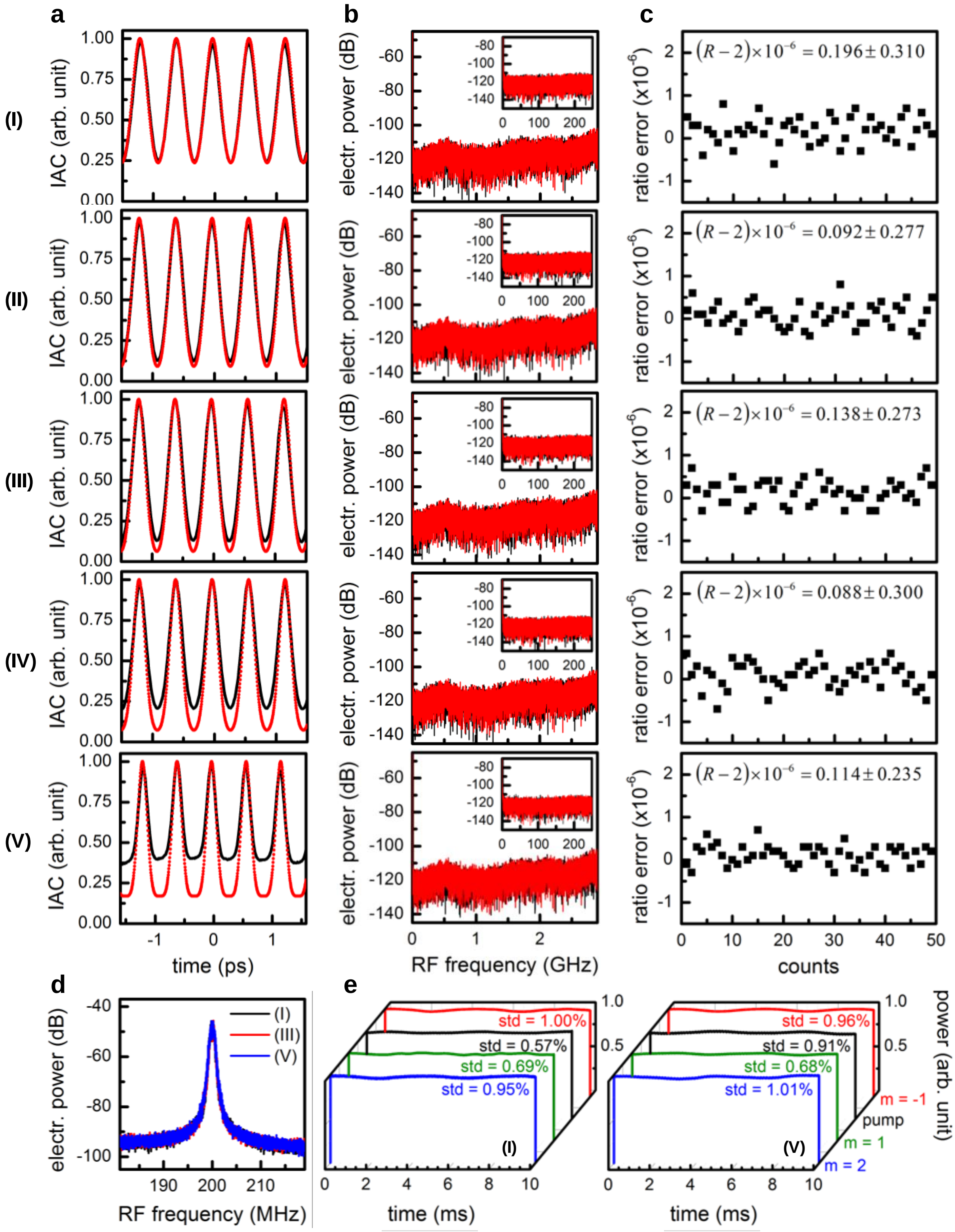

Figure 7-11. Turing pattern coherence characterization.

(a) IAC traces of the Turing rolls at different stages. The red dashed lines are the ideal traces calculated from the spectra, while the black curves are the measured traces. As the sidebands grow, the deviations between the measured and calculated IAC traces also increase. (b) To examine the emergence of incommensurate sub-combs, RF amplitude noise spectra of the Turing rolls (black curve) along with the detector background (red curve) are measured up to 3 GHz, six times the cavity linewidth. No apparent amplitude noise is observed, verifying the existence of the commensurate sub-combs. Inset: zoom-in RF amplitude noise spectra up to 250 MHz, at the instrumentation detection noise floor. (c) To probe the equidistance of the Turing rolls, the beat notes between the three Turing roll sidebands (pump, $m = 1$, and $m = 2$) and the adjacent fiber laser frequency comb lines are measured and the ratio errors are presented. The small deviation from the ideal ratio R of 2 [R defined in the main text as $(\delta_2 - \delta_0)/(\delta_1 - \delta_0)$] verifies Turing pattern's excellent uniformity. The average non-uniformity is measured at 125 mHz, or 7.3×10^{-14} when referenced to the Turing pattern repetition rate at 1.72 THz. (d) The linewidth of the 1st sideband is measured at 500 kHz, limited by the coherence of the pump laser, by the self-heterodyne technique at different stages. No linewidth broadening is observed, independently confirming that the coherence of the Turing roll is maintained at all evolving stages. (e) Power fluctuation of individual sidebands at the stages I (left) and V (right) with a sampling rate of 250 MHz, ruling out the possibility of breathing solutions.

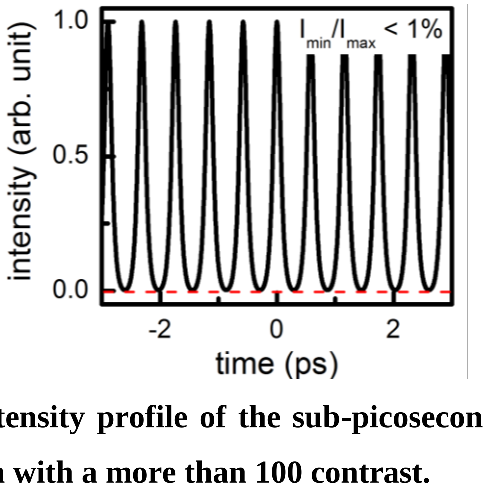

Figure 7-12. Measured intensity profile of the sub-picosecond Turing roll, showing a quasi-sinusoidal oscillation with a more than 100 contrast.

Measured intensity autocorrelation (IAC) profile of the Turing roll at the stage III. Due to the efficient energy conversion from the pump to the first sideband pair, the Turing roll features a quasi-sinusoidal intensity profile with a negligible background of less than 1% of the peak intensity. Nearly background-free operation is important for efficient on-chip THz generation as it reduces the risk of thermal breakdown at high optical pump powers.

To examine whether the temporal shape of the spontaneous Turing pattern is subjected to the perturbation in the initial condition and the pump detuning scan, we performed the IAC measurements at three different tuning speeds and two independent starts. Each of the Turing IAC dynamics remains identical to each other as shown in Figure 7-13, illustrating the good robustness of the Turing patterns. Unlike the microresonator soliton generation where the initial condition and the tuning speed play key roles in determination of the soliton states, here the Turing roll always evolves in the identical route and is robust against perturbations in initial conditions and pump wavelength tuning speeds. To understand the dynamics better, ideal IAC traces from transform-limited Turing patterns are superimposed onto the measured IAC traces (Figure 7-11a; in red). As the Turing pattern is driven closer to resonance, there is increasing discrepancy of the measured pattern from the transform-limit. The change of temporal shapes without the coherence loss implies that the spectral phase of the Turing pattern varies at the different evolving stages and thus different external phase compensation strategies are necessary if the temporal properties of the Turing pattern are to be fully utilized. The spectral phase variation can be understood as the consequence of the pump phase slip around the resonance. The relationship between the output and the intracavity pump power can be written as:

$$A_{p,out} = -\frac{\gamma_c - \gamma_\alpha - i\delta}{\sqrt{2\gamma_c}}\sqrt{T_R}A_{p,cav} \ ,$$

where γ_c and γ_α are the half-width half-maximum linewidths associated with the coupling losses and the intrinsic cavity losses respectively. In our microresonator, γ_c = 160 MHz and γ_α = 90 MHz. The output pump will experience a π phase shift as it traverses through the resonance (Figure 7-15a). Such phase slip is due to the interference between the intracavity and the input pump and thus the other sidebands of the Turing roll will not experience such a phase shift. This additional pump phase slip results in the observed change of temporal structure. The distinct responses to dispersion (illustrated in Figure 7-14; aiding between different Turing states) are well captured by considering the pump phase offset (Figure 7-15b). Note that, most of the phase slip happens very close to cavity resonance and thus the observation of its effect is attributed to the unique design of our microresonator, which utilizes the local mode hybridization to fulfill the phase matching of spontaneous Turing pattern formation and greatly suppresses the Turing pattern destabilization even when the pump is deep into the resonance.

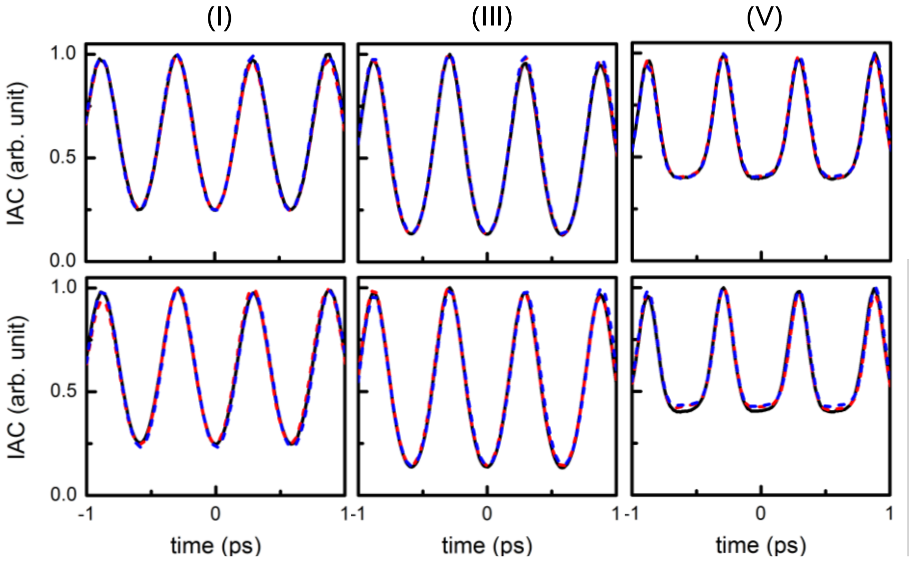

Figure 7-13. Identical intensity autocorrelation (IAC) measured at different scanning speeds and different starts.

At three different scanning speeds (black curve: 1 nm/s; red dashed curve: 0.3 nm/s; blue dashed curve: 0.1 nm/s) and two independent starts (top and bottom), the Turing roll shows the identical generation route.

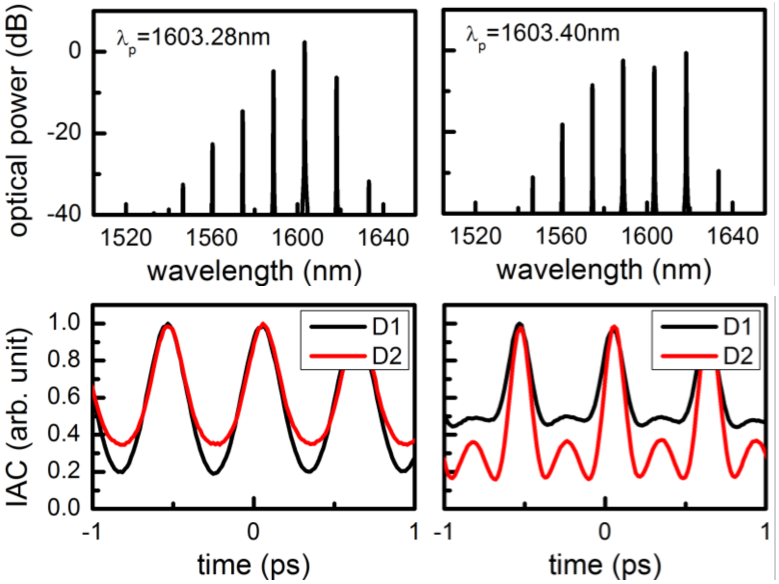

Figure 7-14. The effect of the added dispersion on temporal structure of the Turing pattern at different stages.

IAC traces of the Turing rolls at two different pump detunings (λ_p = 1603.28 nm and λ_p = 1603.40 nm) with two external dispersion compensation. Here D1 and D2 use 60 cm and 90 cm SMF-28 fibers as the external dispersion elements, respectively.

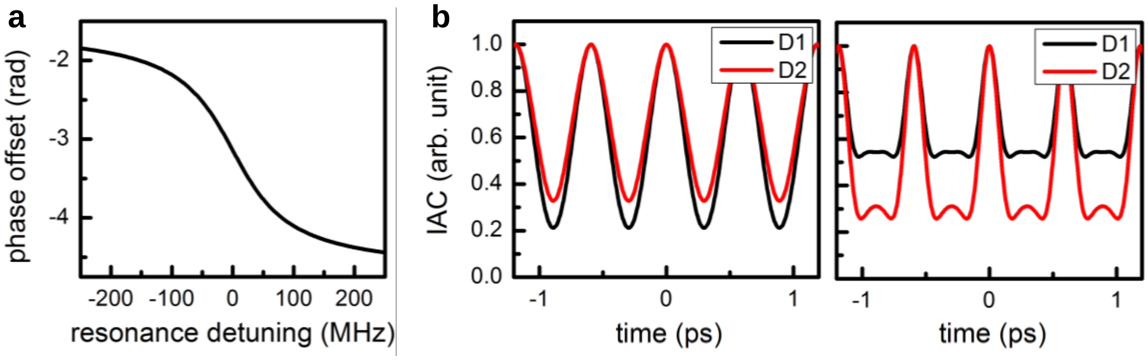

Figure 7-15. Pump-cavity phase slip and its effect on temporal structure of the Turing pattern.

(**a**) Phase offset between the intracavity and output pump light, showing a π phase slip around the resonance. (**b**) IAC traces calculated by adding π/2 to the pump wavelength for λ_p = 1603.40 nm, showing a good agreement with the measurements shown in Figure 7-14.

To characterize the stability of the free-running Turing roll repetition rate, which determines the linewidth and fluctuation of the THz radiation, we beat the pump and one of the sideband with the adjacent fiber laser frequency comb lines and electrically mix the two signals to get the beat note at the frequency difference as shown in Appendix II. Figure 7-16 shows the long-term frequency fluctuation, measuring a root-mean-square frequency fluctuation of 160 kHz over 20 minutes. The left inset shows the linewidth of the beat note with a sweep time of 200 ms, measuring a narrow FWHM linewidth of 9 kHz; the right inset shows the frequency stability of the beat note, measuring an Allan deviation of $1.15\times10^{-8}\cdot\sqrt{\tau}$ when referenced to the THz carrier.

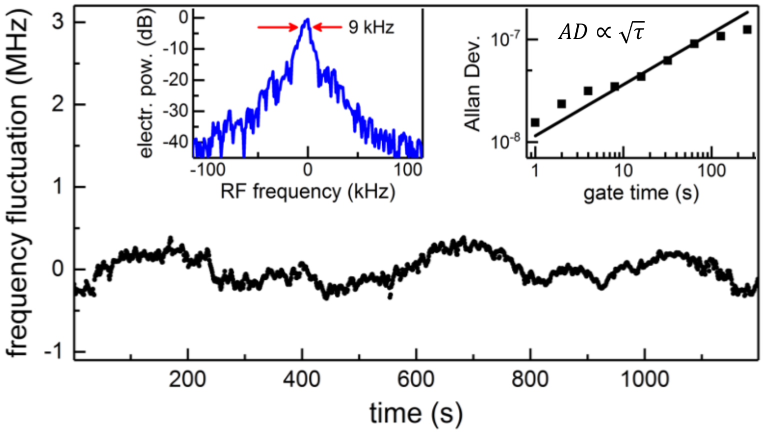

Figure 7-16. Long term frequency fluctuation of the 1st sideband with respect to the pump in the free-running mode, showing the repetition rate fluctuation of 160 kHz over 20 minutes.

The left inset shows the linewidth of the beat note with a sweep time of 200 ms, measuring a narrow FWHM linewidth of 9 kHz; the right inset shows the frequency stability of the beat note, measuring an Allan deviation of $1.15 \times 10^{-8} \cdot \sqrt{\tau}$ when referenced to the THz carrier.

7.4. Long-Term Stability Improvement

The long-term stability of the Turing frequency comb can be further improved by a cost-effective computer-aided slow feedback control of the Turing sideband power. The feedback bandwidth is about 1 Hz. As the microresonator is housed in a temperature-controlled enclosure, we attribute the instability of the Turing roll repetition rate mainly to the effects associated with the fluctuation of intra-cavity power, which at the same time has major impact on the Turing sideband power. Therefore, by stabilizing the Turing sideband power, the fluctuation of intra-cavity power is reduced and consequently the long-term stability of Turing roll repetition rate is improved. The setup is schematically show in Figure 7-17. When the feedback loop is engaged, the frequency stability is significantly improved as shown in Figure 7-18a. Figure 7-18b shows the Allan deviation after stabilization, measuring an improvement of more than two orders of magnitude and reaching 6×10^{-10} at 100 s with an inverse linear dependence on the gate time.

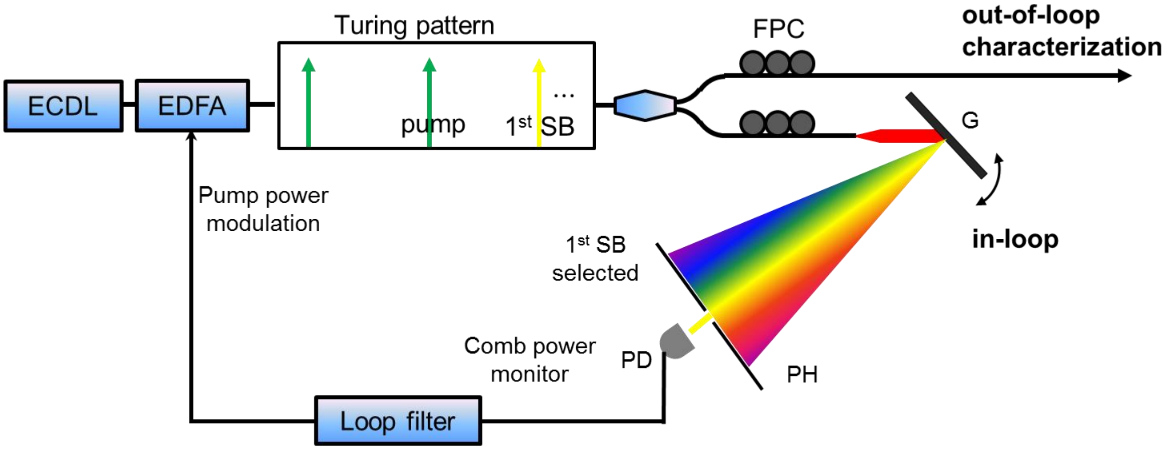

Figure 7-17. Turing pattern frequency stabilization setup.

The first Turing sideband is filtered out and sent to a photodetector to monitor the power fluctuation. A computer program is used as the loop filter that takes in the Turing sideband power fluctuation as the error signal and outputs the control signal to modulate the pump power. The computer-aided slow feedback loop has a bandwidth of 1 Hz.

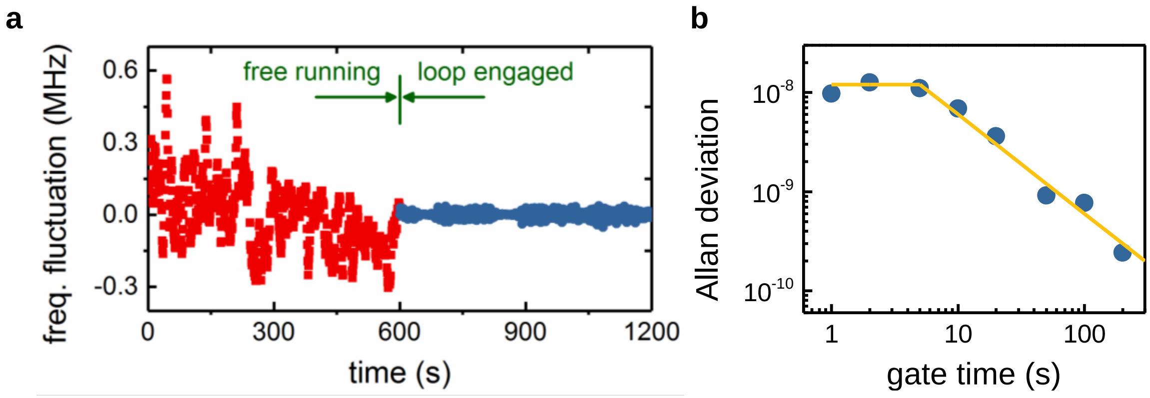

Figure 7-18. Long-term stability improvement with slow-feedback engaged.
(**a**) Long term frequency fluctuation of the 1st sideband with respect to the pump without (red) and with (blue) engaging the computer-aided slow feedback control, counted with a gate time of 1 second. (**b**) Allan deviation of the stabilized THz frequency, measuring a plateau of 1.2×10^{-8} for gate times shorter than 5 second and a roll-off of $6 \times 10^{-8}/\tau$ for longer gate times.

Alternatively, the fluctuation of intra-cavity power can be retrieved by coupled light from a drop port [108] or intra-cavity field that is counter-propagating inside the resonator. The counter-propagating field, i.e. the back-scattered field seen from the input, can be retrieved by placing a circulator before the input collimation. Note that, the power ratio between forward and back-scattered comb depends on mode coupling effect [155], which varies across different comb modes and may also lead to mode splitting at some modes. The latter isn't observed in this comb structure. An example comparison of forward and backward propagating frequency comb is shown in Figure 7-19, where the backward scattered total comb power is around 13 dB lower than the forward comb. By continuously tuning the laser frequency and simultaneously monitoring the change of THz comb spacing and the back scattered power, a linear relation of $7.170 \times 10^{10} MHz/\mu W$, i.e. 71.7 kHz/W, is found with 1% standard deviation. This should give similar performance as the method above.

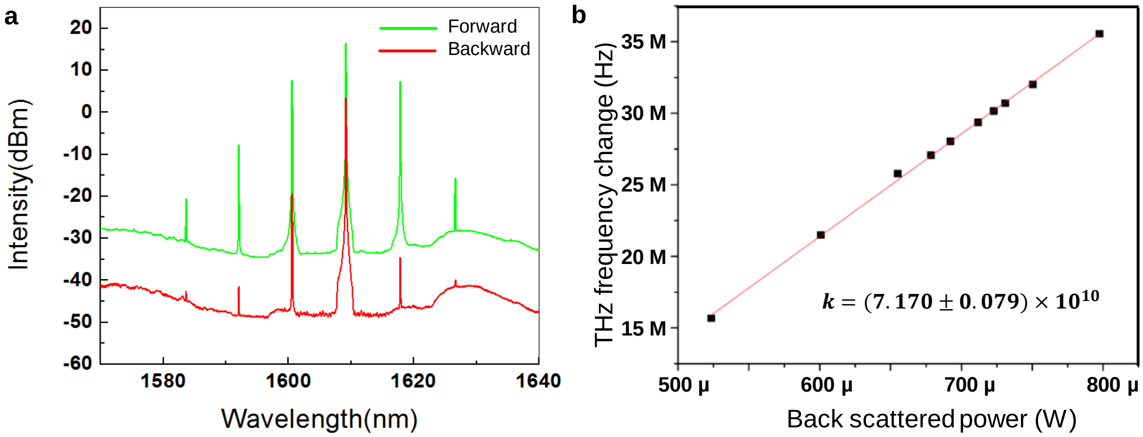

Figure 7-19. Terahertz frequency change as a function of back scattered comb power. (a) Simultaneously measured spectra of forward Turing comb and backward scattered comb. (b) Relation between THz comb spacing and the back scattered comb power, with a fitted slope of 71.7 kHz/W.

7.5. Efficient Terahertz Radiation by Plasmonic Enhanced Photomixers

The robustness, tunability, good coherence, and high efficiency of the demonstrated Turing roll make it an excellent photomixer pump for narrow linewidth tunable THz radiation. Different from deriving the pump from a mode-locked laser [150], the Turing pattern offers the advantage of efficient power use and reduced system complexity as its quasi-sinusoidal intensity profile (Figure 7-12) is directly applicable as a photomixer pump. Other demonstrated photomixer pump source until now [156] include independent lasers with frequency stabilization [157,158], single laser with active high-speed phase modulation [151] and tunable dual-mode lasers [159–163]. While phase-locking two independent lasers to external frequency references can potentially provide the ultimate coherence, it suffers from greatly increased system complexity. Using a single laser with active phase modulation simplifies the system, but high-speed phase modulation with a bandwidth higher than 1 THz is technologically challenging. Tunable dual-mode laser is attractive in its compact footprint and broadband tunability, but it has a large long-term frequency drift due to the uncommon paths taken by the two modes and solving it again requires a sophisticated phase-locking technique. The demonstrated Turing roll provides an alternative platform as it not only is intrinsically compatible with high power operation but also offers a balance between highest coherence and lowest system complexity.

To convert the Turing pattern into the THz radiation, we fabricate an ErAs:InGaAs plasmonic photomixer (Figure 7-21a) which features a good spectral response from 0.8 to 1.6 THz due to the logarithmic spiral antenna design [164]. The plasmonic contact electrode gratings are designed to have 200 nm pitch, 100 nm metal width, 5/45 nm Ti/Au height, and 250 nm thick silicon nitride anti-reflective (AR) coating. They are patterned with electron-beam lithography followed by deposition of Ti/Au and liftoff. A 250 nm silicon nitride anti-reflective coating is then deposited with PECVD. Contact vias are patterned with optical lithography and etched via dry plasma etching. Finally, the logarithmic spiral antennas and bias lines are patterned again with optical lithography, followed by deposition of Ti/Au and liftoff. The fabricated plasmonic photomixers are then mounted on a hyper-hemispherical silicon lens to improve the THz radiation collection.

The setup for THz radiation generation is schematically show in Figure 7-20. A C/L WDM filter, followed by an erbium doped fiber amplifier (EDFA), is used to selectively amplify the Turing pattern sidebands in the 1530 to 1565 nm C-band range. Of note, the EDFA is necessary only because our current Si_3N_4 microresonator has a strong *Q*-factor roll-off in C-band and thus we are limited to pump it in the L-band. Figure 7-21b shows four examples illustrating the tunability of the Turing roll repetition rate (1.14 to 1.57 THz) by adjusting pump wavelength and device temperature, which in turn determines the THz frequency, by tuning the chip temperature or the pump wavelength. Efficient photomixing [165] is achieved based on a logarithmic spiral plasmonic antenna design [164] for efficient THz radiation generation. To achieve the highest photomixing efficiency, both the focus spot size and the position of the optical pump were adjusted to maximize the induced photocurrent level. The generated THz radiation was then measured with a liquid helium-cooled silicon bolometer. Lock-in detection technique was implemented to reduce the noise level and obtain a more reliable reading of the THz radiation power.

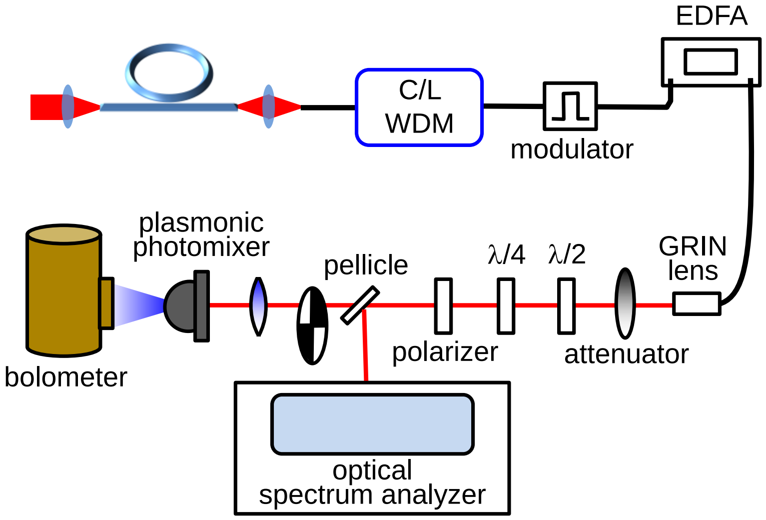

Figure 7-20. THz radiation generation setup.

Figure 7-21c plots the room-temperature radiated THz power as a function of the optical pump power, showing a nearly quadratic dependence even at the maximum available pump power of 54 mW, without much saturation roll-off in the THz generation. Up to 600 μW THz radiation power is generated with an optical-to-THz power conversion efficiency of 1.1%.

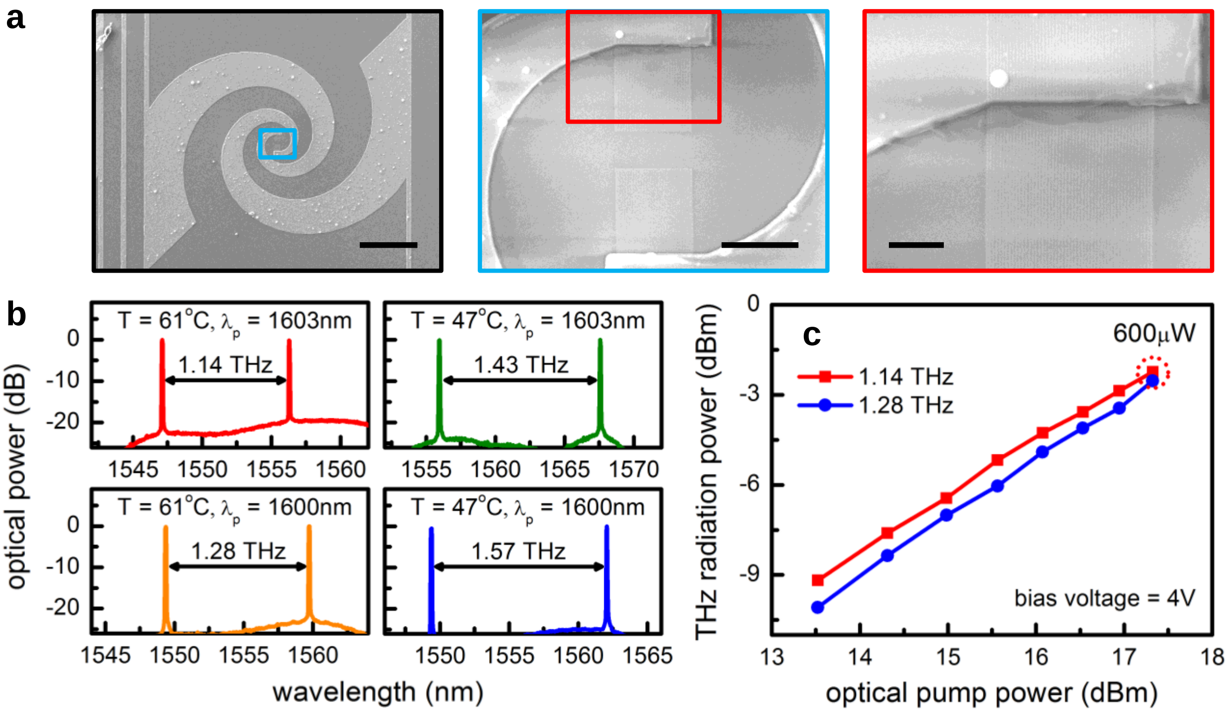

Figure 7-21. Efficient terahertz radiation by plasmonic enhanced photomixer.
(**a**) Scanning electron micrographs of the fabricated plasmonic photomixer with a logarithmic spiral antenna integrated with plasmonic contact electrodes on an ErAs:InGaAs substrate. Scale bars from left to right: 100 μm, 10 μm, and 3 μm. (**b**) Turing roll repetition rate, and hence the generated THz frequency, can be tuned by changing the pump wavelength and the resonator temperature. (**c**) THz radiation power as a function of optical pump power. Power conversion efficiency of 1.1 % can be obtained with an optical pump power of 54 mW.

7.6. Summary

The chapter begins with reviewing evolution dynamics of Kerr frequency comb formation and the uniquely high stability and high robustness of Turing pattern, discusses the scheme and measurement results to effectively circumvent Turing pattern destabilization and enhance energy conversion towards real world applications, and demonstrates the high efficiency optical-to-THz conversion by plasmonic photomixer.

We incorporate mode hybridization mediated phase matching techniques to attain globally stable microresonator Turing patterns in chip-scale silicon nitride microcavities with significantly enlarged parameter spaces, achieving an unprecedented pump depletion and a record high power conversion efficiency of 45% with an elevated peak-to-valley contrast of 100. The techniques also lead to controllable asymmetry in the Turing roll spectrum. The fractional frequency sideband non-uniformity of the Turing pattern is measured down to 7.3×10^{-14}, with a short-term (200 ms sweep time) linewidth of 9 kHz and a long-term (over 20 minutes) fluctuation of 160 kHz in the free-running mode. The long-term stability can be further improved to sub-kHz with a simple computer-aided slow feedback control. We observe the temporal shapes of the Turing patterns change with respect to pump detuning, not because of the coherence loss but the pump phase slip near the cavity resonance. The robustness, tunability, good coherence, and high efficiency of the demonstrated Turing pattern make it an excellent photomixer pump for narrow linewidth tunable THz radiation. Pumping a novel ErAs:InGaAs plasmonic photomixer, we then transfer the Turing pattern optical coherence to the THz carrier and generate up to 600 μW THz radiation power at room temperature. The carrier frequency is discretely tunable over a broadband from 1.14 THz to 1.57 THz. The demonstrated coherent high-power Turing-THz system offers the potential to be the room temperature on-chip THz local oscillator for astrophysics, medical imaging, and wireless communication.

Chapter 8.

Type-1 and Type-2 Satellites in Kerr Frequency Combs

This chapter discusses a new type of frequency comb by multiple phase matching, which is achieved in parametric oscillation process in the nonlinear Kerr medium through cavity dispersion control. Such concept can lead to spectrally-wide optical frequency combs with high conversion efficiency in silicon nitride microresonators driven with a continuous-wave pump. Particularly two satellite comb clusters at ≈ 1.3 μm and 2.0 μm regimes are generated simultaneously together with the central comb. The intensities of the satellite combs are comparable with the first generated parametric sideband near the pump, with a demonstrated record high conversion efficiency more than -30 dB. Under different pumping conditions we report the spectral positions, RF amplitude noise, and evolution dynamics of the satellite combs. The demonstrated satellite comb structures and their formation with multiple phase matching serve as a unique platform for carrier envelope phase stabilization as well as coherent light sources covering extended spectral regimes.

8.1. Introduction

Parametric frequency conversion serves as the fundamental mechanism for a wide range of nonlinear optics phenomena and has triggered tremendous studies [166]. Of great importance among these studies, frequency comb generated in high quality factor (Q) optical microresonators have attracted increasing interests in the recent decade in both theories and experiments [16,120,139,141,167–169]. Microresonator-based frequency combs hold indispensable advantages over conventional mode-locked laser frequency combs in the achievable high repetition rate, low power consumption, and compact platform with high repeatability and scalability. With these, the microresonator frequency combs are promising candidates for numerous applications including optical frequency synthesis, coherent spectroscopy, high-speed communication, high-power terahertz radiation, and multiphoton quantum communication and computation [33,89,141,170–175].

In many of these aspects, achieving a broadband frequency comb is demanding as well as challenging. Of exceptional importance, realizing a self-referenced frequency comb, enabled by *f-to-2f* or *2f-to-3f* carrier-envelop-offset (f_{CEO}) detection and stabilization, can achieve precise measurement of the frequencies of each comb mode, offering the clockwork to count optical frequencies and the synthesis from RF frequencies to optical domain. Realizing a frequency comb with an octave of two-third of octave spanning is comparatively not easy in microresonator combs [71,176], due to the limited degrees of freedom to control the cavity parameters after the devices are patterned. Spectral broadening by nonlinear waveguides can overcome this issue [177]. Recently studied temporal dissipative Kerr solitons (DKSs) achieves a full octave assisted by Cherenkov radiation [167,178], which lead to the successful *2f-3f* self-referencing [168]. these methods, however, suffer from low power conversion efficiency in at least at one spectral edge. Consequently, this often requires post-amplification for sufficient nonlinear frequency conversion, introducing additional noise and power budget to the frequency metrology and referencing system. Cherenkov radiations in both red and blue side of the pump can be generated with higher order dispersion engineered, while the spectral-shift are not necessarily the same depending on the achievable dispersion [179,180].

In terms of comb evolution, conventional microresonator frequency combs usually start with the modulation instability (MI) and four-wave mixing (FWM) leading to phase-correlated comb modes, then generate the sub-comb families [181,115,182,111,31]. The positions of these primarily phase-matched modes are determined by local anomalous dispersion, nonlinear frequency shift and pump-resonance detuning. The total bandwidth of primary modes and the overall comb spectrum are bounded by the second-order dispersion. Multispectral coherent synthesis provides a solution to overcome the bandwidth-power paradox [183,184], which will therefore require multiple stages of laser combs and synthesis effort.

This work aims to circumvent this limitation. Here we report the observation and comprehensive analysis of multi-phase-matched parametric oscillation by cavity dispersion control, where two or more pairs of phase matching can be achieved simultaneously with spectral regimes exceeding MI gain bandwidth. The concept is realized in the spectrally broadened frequency comb generations in silicon nitride microrings spanning up to 100 THz with two types of satellite comb families at ≈ 1.3 μm (O-band) and ≈ 2 μm generated directly from pump with high conversion efficiencies up to -30 dB. The intensity of the satellite combs is comparable with that of strongest primary comb modes near the pump, and each comb family has a 15 THz bandwidth at the 30-dB falloff threshold. The evolution of the satellite combs is rigorously examined, showing rich dynamics. Particularly, type-1 satellite refers to the case where signal and idler lie in the same azimuthal cavity mode, whereas type-2 refers to the case where signal and idler lie in different mode numbers. These two are separated discussed in magnesium fluoride resonators [185] and dispersion-modulated silicon nitride rings [186]. Here we provide a comprehensive study for both the two cases.

Besides the affordable direct comb synthesis, these satellite combs provide rich nonlinear dynamics, for light sources with enlarged wavelength regimes with relaxed pumping conditions. The available spectrum covering from telecom bands (O, S, C and L bands) to 2 µm may also provide demanding frequency channels for coherent communication purpose.

8.2. Satellite Comb Formation from Multiple Phase Matching

Figure 8-1 show a series of measured combs under coupled pump powers of 30.5 dBm and 28.5 dBm with different pump laser-cavity detunings**.** On the blue- and red-sides of the central comb (≈ 1425 nm to 1800 nm), strong intensity satellite clusters – highlighted in the dashed boxes – are simultaneously observed, even with intensities as high as the central comb. The inset of Figure 8-1a shows a scanning electron micrograph of the involved microring cavity, with measured loaded quality factor (Q) of ≈ 950,000. In this 400 µm diameter ring cavity, the waveguide-cavity coupling is tuned to near critical coupling, with nearly one single-mode transverse magnetic polarization (TM_{11}) across pumping wavelength range with measured free spectral range (FSR) of ≈ 113.9 GHz. We denote the pump frequency as ω_0, with the red- and blue-sideband satellites as ω_{-m} and ω_m respectively, where m is the azimuthal mode number of TM_{11} mode.

We define the pump frequency and the center frequencies of the two satellite combs as ω_0, ω_m and ω_{-m}, with corresponding small perturbation values as $\delta\omega_0$, $\delta\omega_m$ and $\delta\omega_{-m}$ respectively. As shown in Figure 8-2b for pumping conditions in Figure 8-1a to c. The cavity phase mismatch between the pump and signal/idler as a function of azimuthal mode number m ($\Delta\omega_m = \omega_m + \omega_{-m} - 2\omega_0$) is twice equal to zero (type-1) and twice equal to the cavity FSR (type-2). Both lead to the cavity phase matching far exceeding modulation instability

(MI) gain bandwidth. In type-1 (orange box), the signal and idler are symmetric in mode number; while in type-2 (yellow box), mode numbers of signal and idler has a difference of one (*M+1*) or even two (*M+2*). As a comparison, conventionally phase matched modes are called type-0 (grey box) here. Figure 8-2(c) shows the zoom-in of the theoretically calculated phase matching curves for type-1 satellites, with experimentally measured phase matching positions labeled as stars with the same color, corresponding to pumping conditions in Fig. 1(a) to (c). Figure 8-2(d) shows the zoom-in of the theoretically calculated phase matching curves for type-2 (*M+1*) satellites, together with the measured phase matching positions. The type-2 (*M+2*) satellite, while hard to observe due to the large separation with the pump, is predicted under the same theory as shown in Figure 8-2(e).

Furthermore, we consider the energy conservation condition and momentum conservation condition respectively,

$$\delta\omega_m + \delta\omega_{-m} = 2\delta\omega_0 \qquad (1)$$

$$\delta\omega_m \cdot GV_m + \delta\omega_{-m} \cdot GV_{-m} = 2\delta\omega_0 \cdot GV_0 \qquad (2)$$

where *GV* is the group velocity. The change of the center frequency of the comb cluster with respect to pump can therefore be expressed as:

$$\frac{\delta\omega_m - \delta\omega_0}{\delta\omega_0} = \frac{2GV_0 - GV_m - GV_{-m}}{GV_m - GV_{-m}} \qquad (3)$$

$$\frac{\delta\omega_{-m} - \delta\omega_0}{\delta\omega_0} = \frac{-2GV_0 + GV_m + GV_{-m}}{GV_m - GV_{-m}} \qquad (4)$$

The left hand sides of equations (3) and (4) represent the tunability of the comb span through adjusting the pump mode. Given the dispersion profile in Figure 8-2a and the phase matching calculation at different pump modes, the tunability is estimated to be 3~4 modes per pump mode at around 1580 nm. A dedicated satellite map is shown in later context.

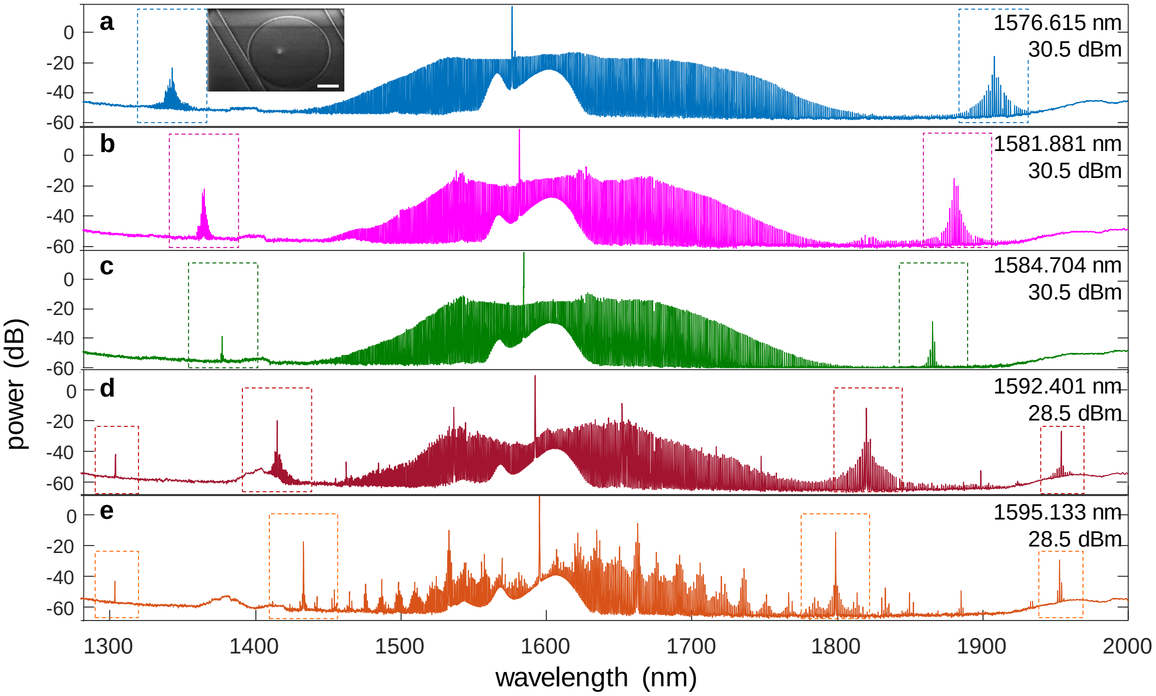

Figure 8-1. Observations of multi-phase-matched satellite frequency combs.

Example spectra of multi-phase-matched frequency comb with two satellite comb families together with the central comb, pumped at (a) 1576.615 nm (b) 1581.881 nm, and (c) 1584.704 nm under on-chip power of 30.5 dBm; (d) 1592.401nm and (e) 1595.133 nm under on-chip power of 28.5 dBm. Inset of (a): scanning electron micrograph of the microcavity frequency comb, with 400 µm silicon nitride ring diameter and 1600 × 800 nm^2 cross-section. Scale bar: 100 µm.

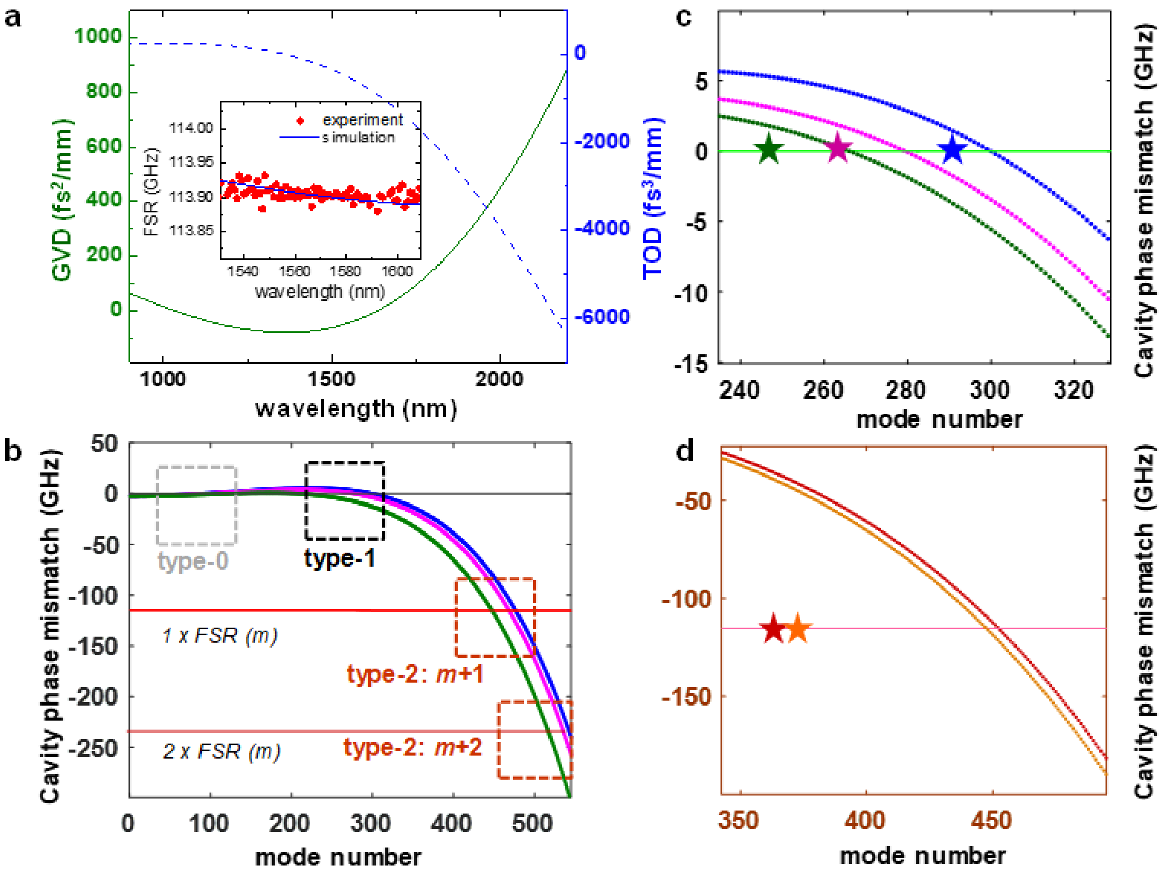

Figure 8-2. Type-1 and type-2 satellite comb cavity phase matching: comparison between modeling and measurements.

a, Simulated GVD (green solid curve) and TOD (blue dashed curve); inset: measured GVD by swept wavelength interferometer method (red dot) compared with simulation (blue solid curve). **b,** Analytical cavity phase mismatch as a function of azimuthal mode number *m*, $\Delta\omega_m = \omega_m + \omega_{-m} - 2\omega_0$, under the different pumping conditions of Figure 8-1a (blue), b (magenta), and c (green). Due to the large TOD, phase matching occurs simultaneously at multiple spectral ranges, leading to the satellite comb families at O-band and ≈ 2 μm as shown in Figure 8-1a to c. If the residual dispersion equals one cavity FSR, parametric oscillation generates the *m*th comb mode at (*m*+1) th or (*m*-1)th cavity mode, and even (*m*+2)th or (*m*-2)th cavity mode. We term the former as *type-1* (black box) and the latter *type-2* (brown boxes). **c,** Theoretically calculated phase matching curves for type-1 satellites: blue, magenta and green correspond to the satellites in Figure 1a to 1c, along with the experimental results (stars with the same colors). **d,** Theoretically calculated phase matching curves for type-2 (*m*+*1*) satellites: red and orange correspond to the satellites in Figure 8-1d (red) and e (orange), along with the experimental results (stars with the same colors).

8.3. Satellites Tunability and Distribution Maps

We next performed a series of measurements to understand the satellite comb formation. The high-*Q* microcavity is pumped by a continuous-wave tunable laser followed by an optical amplifier (BkTel THPOA-SL, L-band; IPG EAD-3K-C, C-band), and a polarizer is employed to guarantee the input beam is TM polarized. In our microcavities, the coupling gap is designed to have nearly critical coupling for fundamental TM mode (TM_{11}) and weak coupling for the second order mode (TM_{21}) across pump wavelength at 1550 nm to 1620 nm. This ensures the waveguide can be treated as single-mode operation for TM comb generation. The output comb spectrum is analyzed in both optical domain by optical spectrum analyzers (Yokogawa AQ6375) and RF domain by an electronic spectrum analyzer (Agilent E4402B). Free-spaced filters and WDM filters are used to filter out the focused O-band, C-band and 2-μm spectral ranges for analysis. An InGaAs photodetector (Thorlabs DET01CFC) is used to measure the amplitude noise of the comb satellites.

Figure 8-3(a) and (b) show an example of satellite comb evolution, pumped at the same mode with slightly different detunings. Note that the satellites grow simultaneously with the primary lines of the central comb, and these primary modes in Figure 8-3(a) shape the basic structure of the fully evolved comb as in Figure 8-3(b). Another example set is shown in Figure 8-4(a) and (b). The satellite centers may shift within ±1 modes due to the changes of the intra-cavity power from detunings, in a similar manner with the primary modes of the central comb. In fact, we emphasize that the intensity of the two satellite combs are comparable with that of the first primary sideband near the pump (with difference less than 2 dB), illustrating as efficient satellite comb formation as the primary comb lines. The ≈ 10 dB power difference visually shown in Figure 8-3(a) is due to the dispersion of collection setup.

Figure 8-3(c) and (d) summarize a series of the satellite combs under different pump wavelength modes. At a constant on-chip pump power of 30 dBm, we tune the pump from 1570 nm to 1590 nm (exciting different pump modes) with the satellite combs. We observe a symmetric spectral-shift of the signal and idler satellite combs, with respect to different pump modes. This illustrates their co-dependence and verifies their physical basis from signal-idler energy conservation instead of other nonlinear processes. As a side note, the spectral-shift of the signal and idler satellite combs differ with respect to pump wavelength, different from Raman-induced comb or lasing observed in WGM resonators [187–189].

The satellite comb span can be tuned from 57 THz to 80 THz. In Figure 8-3(c) and (d), spectra pumped below 1586 nm belong to type-1, the spectral-shift of the satellites is observed with a scaling of 3~5 satellite azimuthal modes per pump modes, agreeing with theoretical estimation. At pump wavelengths larger than 1587 nm, where the dispersion is even closer to zero, the type-1 and type-2 satellites compete more intensively or occur simultaneously (after 1587 nm in Figure 8-3(c) and (d)), also shown in Figure 8-1(d) and (e). In general, given the dispersion of our resonator being examined, type-2 requires a larger phase matching bandwidth compared to type-2, and therefore the phase matching condition considering the sufficient detuning is comparatively harder to satisfy. We believe this effect is atttibuted to the different observation between pumping below 1586 nm and above 1587 nm.

As shown in Figure 8-3b, we note that the asymmetric envelop of central comb is attributed to Cherenkov radiation due to the large third-order dispersion in our microcavities.

It has however limited effect on spectral broadening here. When the ratio of second- and third-order dispersion is larger, a more prominent Cherenkov radiation peak and shift is observed in the main cluster (such as Figure 8-4(c) and (d)).

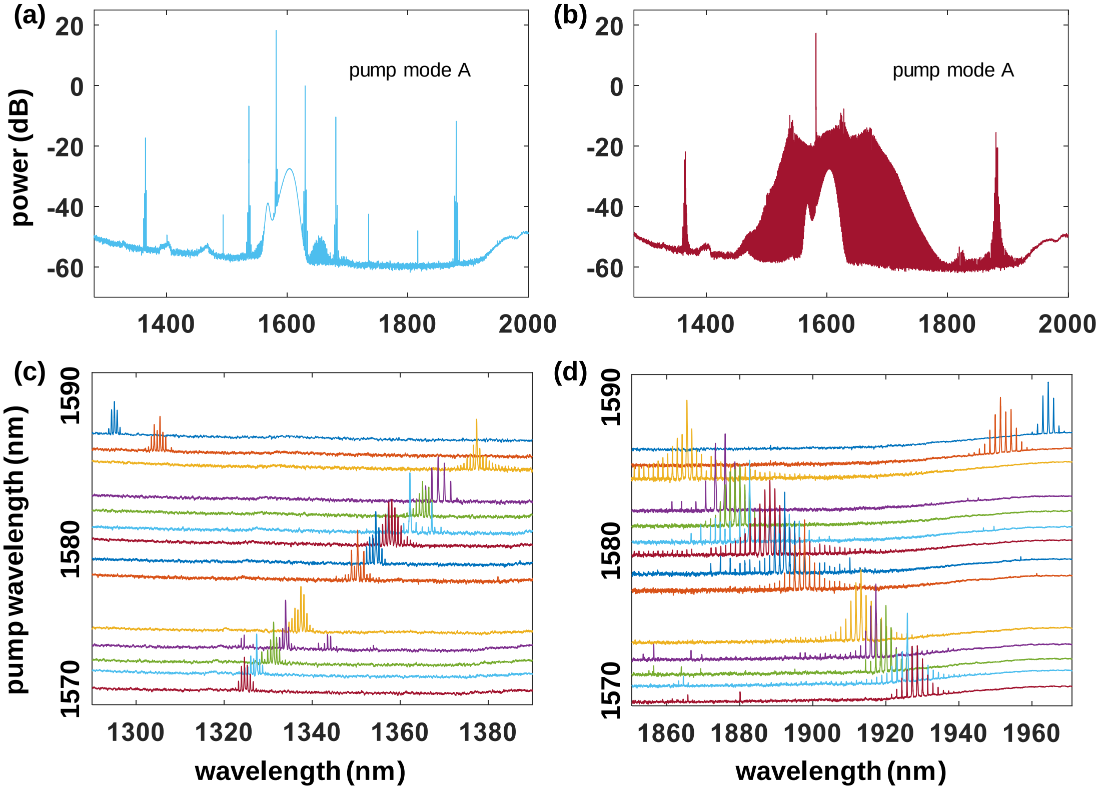

Figure 8-3. Observed satellite comb spectra under different pumping conditions.
a and **b,** Frequency comb spectra pumped at the same resonance mode with different detunings (1981.70 nm and 1981.88 nm, on-chip power of 30dBm). The primarily generated comb lines including the satellite centers hold during the comb growth, occasionally shifted within 3 modes due to the changes of intra-cavity power from detunins. **c** and **d,** Satellite combs generated at different pump wavelength at L-band. The vertical axis is the pump wavelength and the horizontal axis is the comb spectra. The blue-side and red-side clusters show accurate energy conservation with respect to the pump after careful calculation on the frequencies. For each satellite, a clear relationship is observed between the pump wavelength and satellite comb peaks.

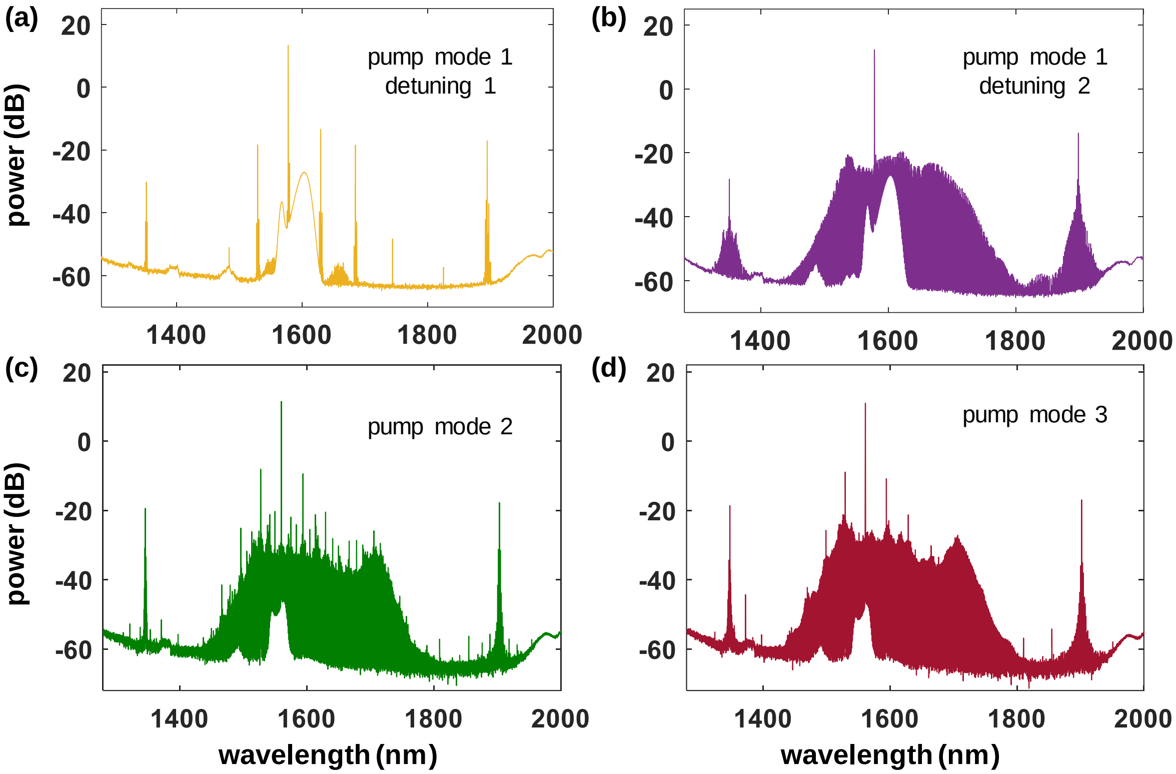

Figure 8-4. Examples of satellite combs pumped at different modes and detunings. **a** and **b,** the evolution of the comb pumped at the same mode (1577.78 nm and 1578.20 nm), where the satellite centers maintain with comb grows. **c** and **d,** **S**atellite combs pumped at 1560.43 nm and 1561.40 nm respectively.

We plot the observed azimuthal mode numbers of the satellite combs under different on-chip powers (squares), along with the theoretical analysis (lines), as shown in Figure 8-5. Satellite maps under different on-chip powers are plotted. Under different pump power and detunings, competition between type-1 and type-2 are observed. The theoretical analysis for type-1 satellites almost matches with experiments. For type-2 satellites, the dispersion and refractive index profile is too far from the pump and isn't calibrated, which should lead to larger discrepancy in theory compared to experiments.

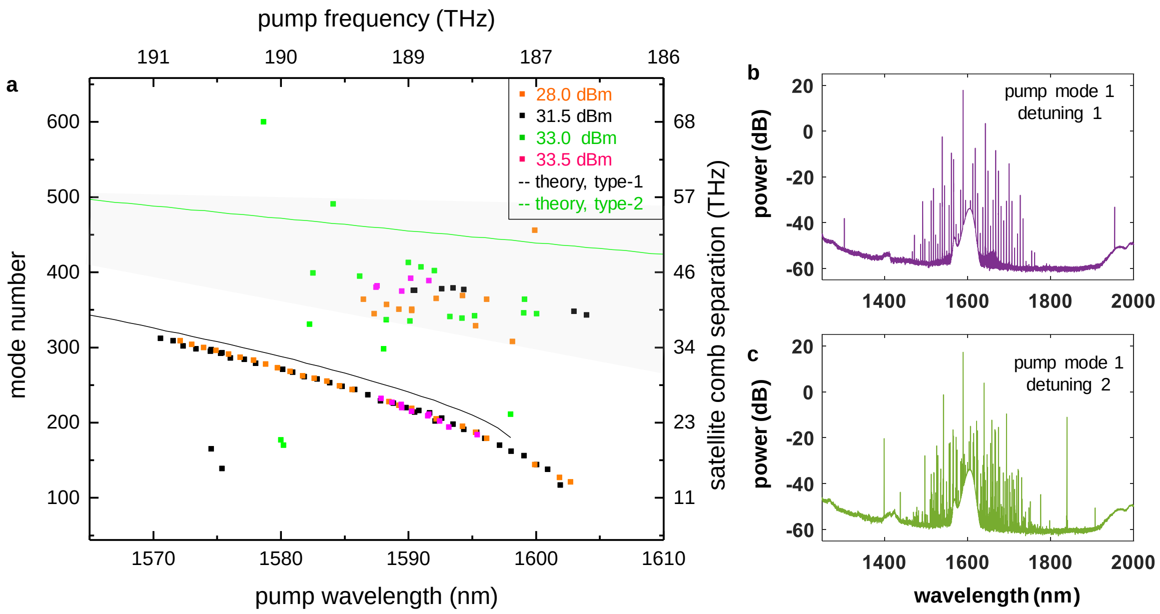

Figure 8-5. Summary of observed satellite map versus theoretical analysis.

a, Satellite maps under different on-chip powers are plotted. Under different pump power and detunings, competition between type-1 and type-2 are observed. The theoretical analysis for type-1 satellites almost matches with experiments. For type-2 satellites, the dispersion and refractive index profile is too far from the pump and isn't calibrated, which should lead to larger discrepancy in theory compared to experiments. **b** and **c**, Example comb formations under the same pump resonance while with slightly different detunings, indicating competing effect between the type-1 and type-2 phase matching.

8.4. Evolution of Satellite Combs and Coherence States Examinations

Figure 8-6 next shows the evolution of the signal satellite cluster and their corresponding RF amplitude noise. We examine the amplitude noise of a type-1 satellite, with laser-cavity detunings up to 103 pm and for the same pump mode. We find the signal satellite cluster has similar evolving dynamics with the central comb. With pump detuned into resonance, the signal satellite cluster starts with low-noise primary comb lines [from (i) to (ii)] when the central comb is also with low-noise as shown in inset of the right panel of Figure

8-6(i). When sub-comb lines begin to evolve [stage (iii)], a clean beat note of 45 MHz with its harmonic are observed; simultaneously the central comb also shows a beat note of 45 MHz. The underlying mechanism for this relationship needs to be investigated further. Note that in previous work [76], the beat notes between the sub-comb families come from the mismatch between the MI-induced phase matching and local cavity FSR. The coherence transition considering the satellite coombs may follow similar rules. By detuning the pump deeper into resonance, a self-injection locking state is observed, resulting a low-noise coherent state comb as shown in (iv). As the detuning is increased further, the comb becomes broader and transits to high noise states, as shown in (v).

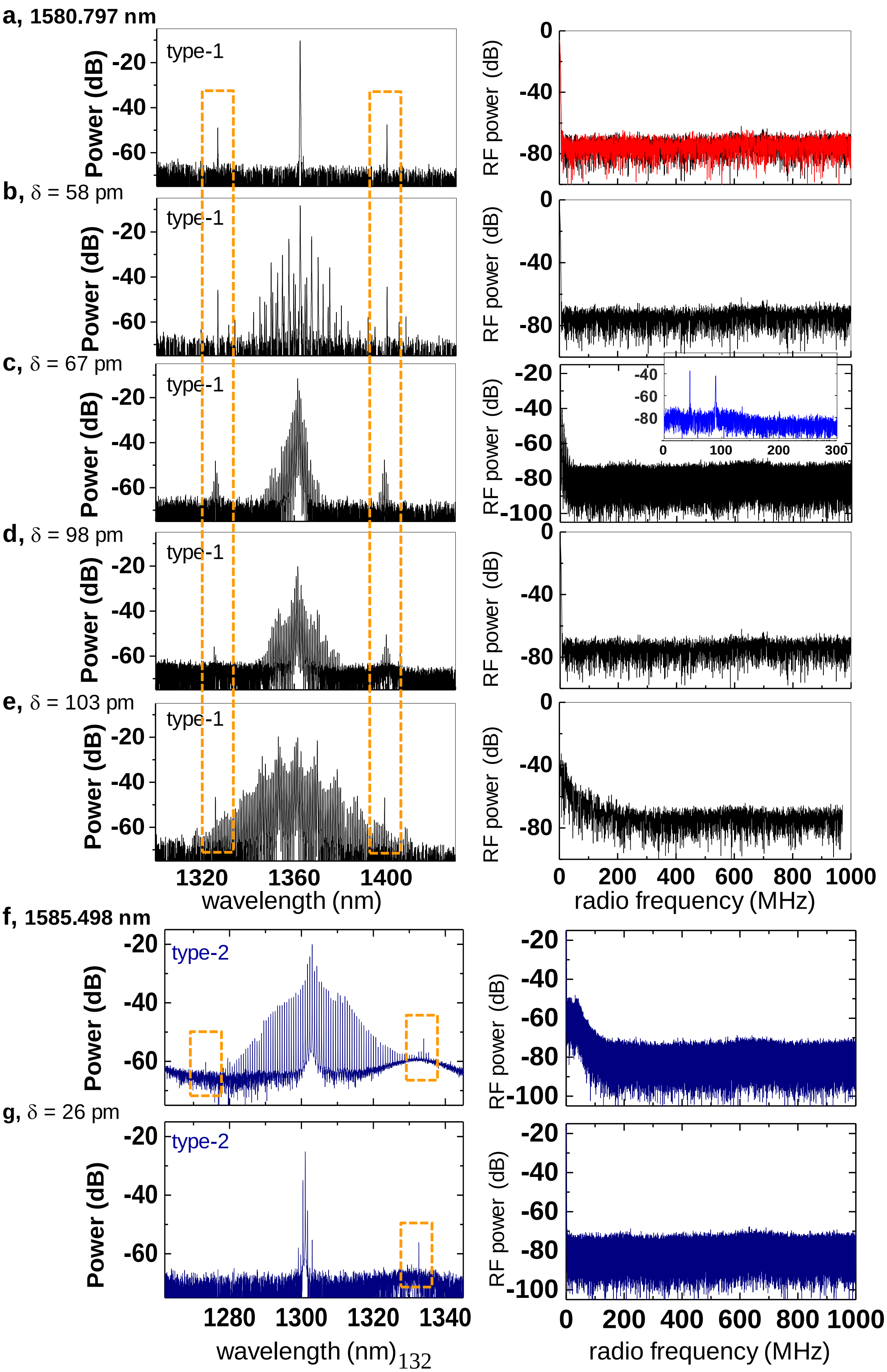

a, 1580.797 nm
b, δ = 58 pm
c, δ = 67 pm
d, δ = 98 pm
e, δ = 103 pm
type-1
Power (dB)
-20
-40
-60
1320
1360
1400
wavelength (nm)
RF power (dB)
0
-20
-40
-60
-80
-100
100
200
300
400
600
800
1000
radio frequency (MHz)
f, 1585.498 nm
g, δ = 26 pm
type-2
1280
1300
1320
1340

Figure 8-6. Coherence evolution of the type-1 and type-2 satellite combs.
Left column: series of satellite comb spectra on the blue side with step-wise detuning of the pump frequency from blue to red over 103 pm (legend label). **Right column:** corresponding RF amplitude noise measurement. **a,** to **e,** for type-1; **f** and **g** for (M+1) type-2. Inset of **c** shows the RF amplitude noise for the central comb, filtered with ≈ 50 nm bandwidth around 1550 nm. Red curve in **a** right panel plots the detector background noise, indicating the low phase noise operation and coherent states of **a**, **b** and **d**. For these three states the central comb is also in a coherent state, as shown in the green line. As detuning increases, sub-comb mode starts to evolve [from **c** onwards]. A synchronized breathing oscillation can be found between the satellite and central combs: as shown in **c** right panel, the RF noise spectrum of the main comb and satellite comb shows the identical breathing frequency at ≈ 45. By further detuning the pump frequency, a self-injection locking state is achieved with again an overall low-noise comb as shown in **d**. With the comb spectra further broadened, the comb turns to a high noise state as shown in **e**. **f** and **g**, Example (*m*+1) type-2 satellites. Once generated, the type-2 satellites evolve in a similar manner as the type-1 satellites.

8.5. Summary

In conclusion, we apply multi-phase-matching concept in microresonator-based comb generations. The comb has two satellite families together with the central comb spanning up to two-thirds of an octave with high conversion efficiency from the pump. We experimentally study in detail its formation, mapping the spanning with respect to pump wavelength and pump power. At certain parameter setting, a global coherence can be achieved, while in other cases a breathing state is found. Theoretical analysis and prediction is detailed for *type-1*and *type-2* satellite combs, both finding good agreement with experimental results. Multiple phase matching may encompass several applications, such as on-chip coherent light sources with extended wavelength ranges, self-referencing frequency comb synthesis, efficient broad-band communication sources for multiple telecom bands mid-infrared soliton generation.

Chapter 9.

Conclusions and Prospects

In the dissertation, various types of frequency sources focusing on the theme of precise optical frequency synthesis are examined. On the platform of silicon photonic crystal nanocavities, the self-pulsation is firstly observed due to competing effects of thermal and free carrier dispersions in an optical resonator, with RF tones controllable by laser input parameters. In the subjects of CMOS-compatible microresonator frequency combs, the fundamental mechanism of mode-locking in a high-quality factor microresonator is firstly examined, supported by ultrafast optical characterizations, analytical closed-form solutions and numerical modeling. In the evolution of these frequency microcombs, the key nonlinear dynamical effect governing the comb state coherence is rigorously analyzed. Secondly, a prototype of chip-scale optical frequency synthesizer is demonstrated, with the laser frequency comb stabilized down to instrument-limited 50-mHz RF frequency inaccuracies and 10^{-16} fractional frequency inaccuracies, near the fundamental limits. Thirdly, a globally stable Turing pattern is achieved and characterized in these nonlinear resonators with high-efficiency conversion, subsequently generating coherent high-power terahertz radiation via plasmonic photomixers. Finally, a new universal modality of frequency combs is discussed, including satellite states, dynamical tunability, and high efficiency conversion towards direct chip-scale optical frequency synthesis at the precision metrology frontiers.

In the widely investigated yet continuously intriguing field of microresonator frequency combs, there are still rich physics to uncover and practical challenges to address. One of the topics following the dissertation, is the direct measurement and control of carrier-envelop-phase (CEP) and timing jitter. These observations in the different evolved stages of the microresonator combs allows deeper examination of the rich physics to the fundamental limits. The configuration out of this will lead to a modular metrological tool for various applications in the future. Secondly, delivering a self-referenced frequency comb synthesizer without external optical reference based on nonlinear interferometry has been challenging while witnessed promising progress in terms of the comb platform itself as discussed in former chapter. Further implementation of the scheme is realistic. Thirdly, frequency comb sources in other spectral regimes are under examined by pioneers yet need more investigation, especially those covering molecular fingerprint region and atmospheric transmission window and those interesting for bio-medical imaging and astronomical calibration. Their applications such as coherent spectroscopy, precision timing, high-efficiency communications and navigation are promising to create mass markets and trigger new findings.

Appendices

A. I. Microresonator dispersion measurement setup and scheme

Figure A1 shows the schematic diagram of the dispersion measurement setup [20]. The microresonator transmission was recorded when the laser was swept from 1550 nm to 1630 nm at a tuning speed of 40 nm/s. The sampling clock of the data acquisition is derived from the photodetector monitoring the laser transmission through a fiber Mach-Zehnder interferometer with 40 m unbalanced path lengths, which translates to a 5 MHz optical frequency sampling resolution. Transmission of the hydrogen cyanide gas cell was simultaneously measured and the absorption features were used for absolute wavelength calibrations. Each resonance was fitted with a Lorentzian lineshape to determine the resonance frequency and the quality factor. The microresonator dispersion was then calculated by analyzing the wavelength dependence of the free spectral range. Example measurements and their comparisons with simulations are discussed in 3.1.2.

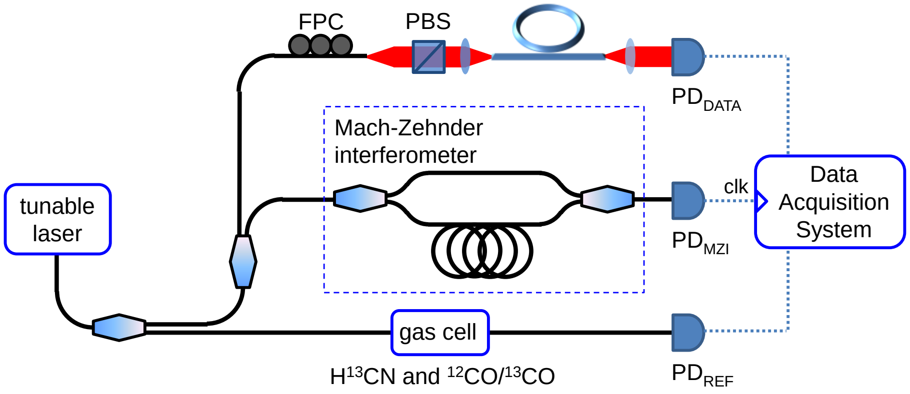

Figure A1. Microresonator dispersion measurement setup.

A. II. Microresonator frequency comb frequency stability and equidistance measurement setup

To probe the equidistance of the frequency combs, a uniformity measurement setup is employed as shown in Figure A2. The generated comb spectrum was split and sent to 3 beat detection units (BDUs) individually optimized for the wavelength of the pump, along with the two comb modes. Heterodyne beat notes were generated between the Turing roll (green arrows) and a reference fiber laser frequency comb (red arrows). The gratings in the BDUs critically suppress the unwanted reference fiber laser frequency comb teeth such that clean heterodyne beat notes with more than 40 dB signal to noise ratio (measured with a 100 kHz resolution bandwidth), sufficient for reliable measurements, can be routinely obtained. The beat notes from the sidebands (δ_1 and δ_2) were mixed with the beat note from the pump (δ_0) to cancel the residual pump wavelength instability before being measured by a high-resolution frequency counter (10 mHz frequency error at 1 second). The frequency counter was operated in the ratio counting mode, to circumvent the synchronization challenge of simultaneous beat note measurements and achieve a more accurate measurement.

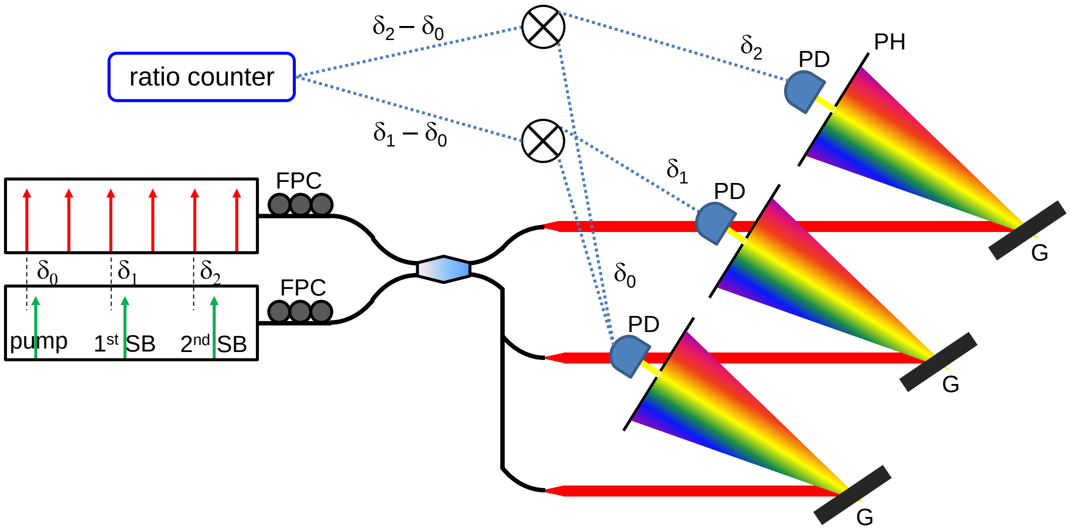

Figure A2. Microresonator frequency comb uniformity measurement setup.

A. III. Microresonator frequency comb uniformity measurement setup

Figure A3 shows the schematic diagram of the self-heterodyne linewidth measurement setup [190]. The input was split into two parts with 70% of it being sent through an acousto-optic modulator which shifts the optical frequencies by 200 MHz. The other portion was sent through a 5 km single mode optical fiber, providing a time delay of 24.5 μs. Both lights were then recombined, and the resulting beat note was recorded and analyzed with a high-speed photodetector and an electrical spectrum analyzer. The RF spectrum becomes a self-convolution of the laser spectrum, from which the linewidth can be retrieved, as long as the coherence length is shorter than the introduced delay. Thus our self-heterodyne measurement setup can measure a minimum linewidth at 13 kHz, about 40 times smaller than the measured laser linewidth.

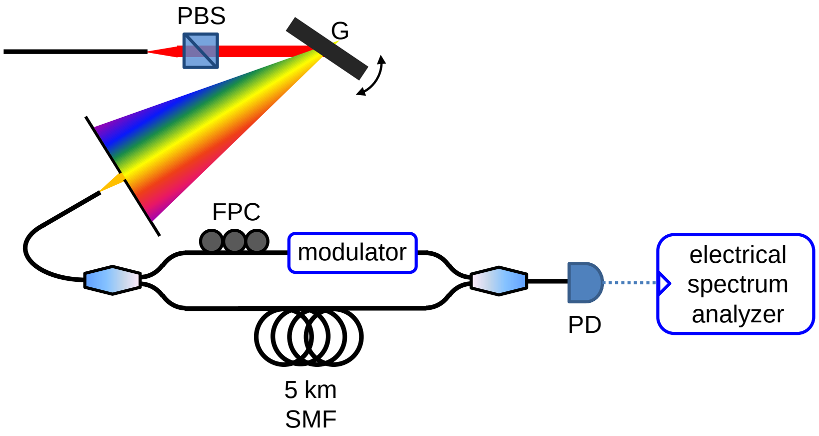

Figure A3. Self-heterodyne measurement setup.

Bibliography

1. J. Reichert, R. Holzwarth, T. Udem, and T. W. Hänsch, "Measuring the frequency of light with mode-locked lasers," Opt. Commun. **172**, 59–68 (1999).

2. J. L. Hall, "Nobel Lecture: Defining and measuring optical frequencies," Rev. Mod. Phys. **78**, 1279–1295 (2006).

3. T. W. Hänsch, "Nobel Lecture: Passion for precision," Rev. Mod. Phys. **78**, 1297–1309 (2006).

4. R. Holzwarth, T. Udem, T. W. Hänsch, J. C. Knight, W. J. Wadsworth, and P. S. J. Russell, "Optical Frequency Synthesizer for Precision Spectroscopy," Phys. Rev. Lett. **85**, 2264 (2000).

5. A. Cingöz, D. C. Yost, T. K. Allison, A. Ruehl, M. E. Fermann, I. Hartl, and J. Ye, "Direct frequency comb spectroscopy in the extreme ultraviolet," Nature **482**, 68–71 (2012).

6. I. Coddington, N. Newbury, and W. Swann, "Dual-comb spectroscopy," Optica **3**, 414–426 (2016).

7. T. Udem, R. Holzwarth, and T. W. Hänsch, "Optical frequency metrology," Nature **416**, 233–237 (2002).

8. L.-S. Ma, Z. Bi, A. Bartels, L. Robertsson, M. Zucco, R. S. Windeler, G. Wilpers, C. Oates, L. Hollberg, and S. A. Diddams, "Optical Frequency Synthesis and Comparison with Uncertainty at the 10-19 Level," Science **303**, 1843–1845 (2004).

9. C.-H. Li, A. J. Benedick, P. Fendel, A. G. Glenday, F. X. Kartner, D. F. Phillips, D. Sasselov, A. Szentgyorgyi, and R. L. Walsworth, "A laser frequency comb that enables radial velocity measurements with a precision of 1[thinsp]cm[thinsp]s-1," Nature **452**, 610–612 (2008).

10. T. Wilken, G. L. Curto, R. A. Probst, T. Steinmetz, A. Manescau, L. Pasquini, J. I. G. Hernández, R. Rebolo, T. W. Hänsch, T. Udem, and R. Holzwarth, "A spectrograph for exoplanet observations calibrated at the centimetre-per-second level," Nature **485**, 611–614 (2012).

11. J. S. Levy, A. Gondarenko, M. A. Foster, A. C. Turner-Foster, A. L. Gaeta, and M. Lipson, "CMOS-compatible multiple-wavelength oscillator for on-chip optical interconnects," Nat. Photonics **4**, 37–40 (2010).

12. J. Pfeifle, V. Brasch, M. Lauermann, Y. Yu, D. Wegner, T. Herr, K. Hartinger, P. Schindler, J. Li, D. Hillerkuss, R. Schmogrow, C. Weimann, R. Holzwarth, W. Freude, J. Leuthold, T. J. Kippenberg, and C. Koos, "Coherent terabit communications with microresonator Kerr frequency combs," Nat. Photonics **8**, 375–380 (2014).

13. T. M. Fortier, M. S. Kirchner, F. Quinlan, J. Taylor, J. C. Bergquist, T. Rosenband, N. Lemke, A. Ludlow, Y. Jiang, C. W. Oates, and S. A. Diddams, "Generation of ultrastable microwaves via optical frequency division," Nat. Photonics **5**, 425–429 (2011).

14. F. Ferdous, H. Miao, D. E. Leaird, K. Srinivasan, J. Wang, L. Chen, L. T. Varghese, and A. M. Weiner, "Spectral line-by-line pulse shaping of on-chip microresonator frequency combs," Nat. Photonics **5**, 770–776 (2011).

15. J. Ye and S. T. Cundiff, *Femtosecond Optical Frequency Comb: Principle, Operation and Applications*, 2005 edition (Springer, 2005).

16. P. Del'Haye, A. Schliesser, O. Arcizet, T. Wilken, R. Holzwarth, and T. J. Kippenberg, "Optical frequency comb generation from a monolithic microresonator," Nature **450**, 1214–1217 (2007).

17. T. J. Kippenberg, R. Holzwarth, and S. A. Diddams, "Microresonator-Based Optical Frequency Combs," Science **332**, 555–559 (2011).

18. F. Ferdous, H. Miao, D. E. Leaird, K. Srinivasan, J. Wang, L. Chen, L. T. Varghese, and A. M. Weiner, "Spectral line-by-line pulse shaping of on-chip microresonator frequency combs," Nat. Photonics **5**, 770–776 (2011).

19. A. A. Savchenkov, A. B. Matsko, V. S. Ilchenko, I. Solomatine, D. Seidel, and L. Maleki, "Tunable Optical Frequency Comb with a Crystalline Whispering Gallery Mode Resonator," Phys. Rev. Lett. **101**, 093902 (2008).

20. S.-W. Huang, H. Zhou, J. Yang, J. F. McMillan, A. Matsko, M. Yu, D.-L. Kwong, L. Maleki, and C. W. Wong, "Mode-Locked Ultrashort Pulse Generation from On-Chip Normal Dispersion Microresonators," Phys. Rev. Lett. **114**, 053901 (2015).

21. I. S. Grudinin, N. Yu, and L. Maleki, "Generation of optical frequency combs with a CaF2 resonator," Opt. Lett. **34**, 878–880 (2009).

22. Y. K. Chembo, D. V. Strekalov, and N. Yu, "Spectrum and Dynamics of Optical Frequency Combs Generated with Monolithic Whispering Gallery Mode Resonators," Phys. Rev. Lett. **104**, 103902 (2010).

23. W. Liang, A. A. Savchenkov, A. B. Matsko, V. S. Ilchenko, D. Seidel, and L. Maleki, "Generation of near-infrared frequency combs from a MgF2 whispering gallery mode resonator," Opt. Lett. **36**, 2290–2292 (2011).

24. T. Herr, K. Hartinger, J. Riemensberger, C. Y. Wang, E. Gavartin, R. Holzwarth, M. L. Gorodetsky, and T. J. Kippenberg, "Universal formation dynamics and noise of Kerr-frequency combs in microresonators," Nat. Photonics **6**, 480–487 (2012).

25. J. Li, H. Lee, T. Chen, and K. J. Vahala, "Low-Pump-Power, Low-Phase-Noise, and Microwave to Millimeter-Wave Repetition Rate Operation in Microcombs," Phys. Rev. Lett. **109**, 233901 (2012).

26. P. Del'Haye, K. Beha, S. B. Papp, and S. A. Diddams, "Self-Injection Locking and Phase-Locked States in Microresonator-Based Optical Frequency Combs," Phys. Rev. Lett. **112**, 043905 (2014).

27. A. R. Johnson, Y. Okawachi, J. S. Levy, J. Cardenas, K. Saha, M. Lipson, and A. L. Gaeta, "Chip-based frequency combs with sub-100 GHz repetition rates," Opt. Lett. **37**, 875–877 (2012).

28. J. Yang, T. Gu, J. Zheng, M. Yu, G.-Q. Lo, D.-L. Kwong, and C. W. Wong, "Radio frequency regenerative oscillations in monolithic high-Q/V heterostructured photonic crystal cavities," Appl. Phys. Lett. **104**, 061104 (2014).

29. Y. K. Chembo and N. Yu, "Modal expansion approach to optical-frequency-comb generation with monolithic whispering-gallery-mode resonators," Phys. Rev. A **82**, 033801 (2010).

30. S. Coen, H. G. Randle, T. Sylvestre, and M. Erkintalo, "Modeling of octave-spanning Kerr frequency combs using a generalized mean-field Lugiato–Lefever model," Opt. Lett. **38**, 37–39 (2013).

31. J. Yang, S.-W. Huang, B. H. McGuyer, M. Yu, M. P. McDonald, G. Lo, D.-L. Kwong, T. Zelevinsky, and C. W. Wong, "Bichromatically-pumped coherent Kerr frequency comb with controllable repetition rates," in *Conference on Lasers and Electro-Optics (2016), Paper FM1A.8* (Optical Society of America, 2016), p. FM1A.8.

32. S.-W. Huang, J. Yang, J. Lim, H. Zhou, M. Yu, D.-L. Kwong, and C. W. Wong, "A low-phase-noise 18 GHz Kerr frequency microcomb phase-locked over 65 THz," Sci. Rep. **5**, 13355 (2015).

33. S.-W. Huang, J. Yang, S.-H. Yang, M. Yu, D.-L. Kwong, T. Zelevinsky, M. Jarrahi, and C. W. Wong, "Globally Stable Microresonator Turing Pattern Formation for Coherent High-Power THz Radiation On-Chip," Phys. Rev. X **7**, 041002 (2017).

34. S. Noda, A. Chutinan, and M. Imada, "Trapping and emission of photons by a single defect in a photonic bandgap structure," Nature **407**, 608–610 (2000).

35. B.-S. Song, S. Noda, and T. Asano, "Photonic Devices Based on In-Plane Hetero Photonic Crystals," Science **300**, 1537–1537 (2003).

36. E. Yablonovitch, "Photonic crystals: semiconductors of light," Sci. Am. **285**, 47–51, 54–55 (2001).

37. J. D. Joannopoulos, S. G. Johnson, J. N. Winn, and R. D. Meade, *Photonic Crystals: Molding the Flow of Light, Second Edition* (Princeton University Press, 2011).

38. T. Baba, "Slow light in photonic crystals," Nat. Photonics **2**, 465 (2008).

39. Y. Takahashi, Y. Inui, M. Chihara, T. Asano, R. Terawaki, and S. Noda, "A micrometre-scale Raman silicon laser with a microwatt threshold," Nature **498**, 470–474 (2013).

40. X. Yang and C. W. Wong, "Design of photonic band gap nanocavities for stimulated Raman amplification and lasing in monolithic silicon," Opt. Express **13**, 4723–4730 (2005).

41. J. Vučković and Y. Yamamoto, "Photonic crystal microcavities for cavity quantum electrodynamics with a single quantum dot," Appl. Phys. Lett. **82**, 2374–2376 (2003).

42. S. W. Chen, L. B. Zhang, Y. H. Fei, and T. T. Cao, "Bistability and self-pulsation phenomena in silicon microring resonators based on nonlinear optical effects," Opt. Express **20**, 7454–7468 (2012).

43. M. Soltani, S. Yegnanarayanan, Q. Li, A. A. Eftekhar, and A. Adibi, "Self-sustained gigahertz electronic oscillations in ultrahigh-Q photonic microresonators," Phys. Rev. A **85**, (2012).

44. C. Baker, S. Stapfner, D. Parrain, S. Ducci, G. Leo, E. M. Weig, and I. Favero, "Optical instability and self-pulsing in silicon nitride whispering gallery resonators," Opt. Express **20**, 29076–29089 (2012).

45. T. J. Johnson, M. Borselli, and O. Painter, "Self-induced optical modulation of the transmission through a high-Q silicon microdisk resonator," Opt. Express **14**, 817–831 (2006).

46. W. H. P. Pernice, M. Li, and H. X. Tang, "Time-domain measurement of optical transport in silicon micro-ring resonators," Opt. Express **18**, 18438–18452 (2010).

47. T. V. Vaerenbergh, M. Fiers, J. Dambre, and P. Bienstman, "An optical delayline based on excitable microrings," in *2014 IEEE Photonics Conference (IPC)* (2014), pp. 118–119.

48. L. B. Zhang, Y. H. Fei, T. T. Cao, Y. M. Cao, Q. Y. Xu, and S. W. Chen, "Multibistability and self-pulsation in nonlinear high-Q silicon microring resonators considering thermo-optical effect," Phys. Rev. A **87**, (2013).

49. T. Carmon, L. Yang, and K. J. Vahala, "Dynamical thermal behavior and thermal self-stability of microcavities," Opt. Express **12**, 4742–4750 (2004).

50. Y. S. Park and H. L. Wang, "Regenerative pulsation in silica microspheres," Opt. Lett. **32**, 3104–3106 (2007).

51. A. E. Fomin, M. L. Gorodetsky, I. S. Grudinin, and V. S. Ilchenko, "Nonstationary nonlinear effects in optical microspheres," J. Opt. Soc. Am. B-Opt. Phys. **22**, 459–465 (2005).

52. A. Armaroli, S. Malaguti, G. Bellanca, S. Trillo, A. de Rossi, and S. Combrié, "Oscillatory dynamics in nanocavities with noninstantaneous Kerr response," Phys. Rev. A **84**, 053816 (2011).

53. S. Malaguti, G. Bellanca, A. de Rossi, S. Combrié, and S. Trillo, "Self-pulsing driven by two-photon absorption in semiconductor nanocavities," Phys. Rev. A **83**, 051802 (2011).

54. L. Zhang, Y. Fei, Y. Cao, X. Lei, and S. Chen, "Experimental observations of thermo-optical bistability and self-pulsation in silicon microring resonators," J. Opt. Soc. Am. B **31**, 201–206 (2014).

55. X. Yang, C. Husko, C. W. Wong, M. B. Yu, and D. L. Kwong, "Observation of femtojoule optical bistability involving Fano resonances in high-Q/V-m silicon photonic crystal nanocavities," Appl. Phys. Lett. **91**, (2007).

56. X. Yang, C. J. Chen, C. A. Husko, and C. W. Wong, "Digital resonance tuning of high-Q/Vm silicon photonic crystal nanocavities by atomic layer deposition," Appl. Phys. Lett. **91**, (2007).

57. J. Leuthold, C. Koos, and W. Freude, "Nonlinear silicon photonics," Nat. Photonics **4**, 535–544 (2010).

58. M. Notomi, A. Shinya, S. Mitsugi, G. Kira, E. Kuramochi, and T. Tanabe, "Optical bistable switching action of Si high-Q photonic-crystal nanocavities," Opt. Express **13**, 2678–2687 (2005).

59. C. Husko, A. De Rossi, S. Combrie, Q. V. Tran, F. Raineri, and C. W. Wong, "Ultrafast all-optical modulation in GaAs photonic crystal cavities," Appl. Phys. Lett. **94**, (2009).

60. M. Minkov, U. P. Dharanipathy, R. Houdré, and V. Savona, "Statistics of the disorder-induced losses of high-Q photonic crystal cavities," Opt. Express **21**, 28233–28245 (2013).

61. K. Ikeda and O. Akimoto, "Instability Leading to Periodic and Chaotic Self-Pulsations in a Bistable Optical Cavity," Phys. Rev. Lett. **48**, 617–620 (1982).

62. A. de Rossi, M. Lauritano, S. Combrié, Q. V. Tran, and C. Husko, "Interplay of plasma-induced and fast thermal nonlinearities in a GaAs-based photonic crystal nanocavity," Phys. Rev. A **79**, 043818 (2009).

63. B. E. Little, S. T. Chu, H. A. Haus, J. Foresi, and J. P. Laine, "Microring resonator channel dropping filters," J. Light. Technol. **15**, 998–1005 (1997).

64. C. Manolatou, M. J. Khan, S. Fan, P. R. Villeneuve, H. A. Haus, and J. D. Joannopoulos, "Coupling of modes analysis of resonant channel add-drop filters," Quantum Electron. IEEE J. Of **35**, 1322–1331 (1999).

65. T. Gu, N. Petrone, J. F. McMillan, A. van der Zande, M. Yu, G. Q. Lo, D. L. Kwong, J. Hone, and C. W. Wong, "Regenerative oscillation and four-wave mixing in graphene optoelectronics," Nat. Photonics **6**, 554–559 (2012).

66. N. Cazier, X. Checoury, L. D. Haret, and P. Boucaud, "High-frequency self-induced oscillations in a silicon nanocavity," Opt. Express **21**, 13626–13638 (2013).

67. P. E. Barclay, K. Srinivasan, and O. Painter, "Nonlinear response of silicon photonic crystal microresonators excited via an integrated waveguide and fiber taper," Opt. Express **13**, 801–820 (2005).

68. A. de Rossi, M. Lauritano, S. Combrie, Q. V. Tran, and C. Husko, "Interplay of plasma-induced and fast thermal nonlinearities in a GaAs-based photonic crystal nanocavity," Phys. Rev. A **79**, (2009).

69. P. Del'Haye, O. Arcizet, A. Schliesser, R. Holzwarth, and T. J. Kippenberg, "Full Stabilization of a Microresonator-Based Optical Frequency Comb," Phys. Rev. Lett. **101**, 053903 (2008).

70. L. Razzari, D. Duchesne, M. Ferrera, R. Morandotti, S. Chu, B. E. Little, and D. J. Moss, "CMOS-compatible integrated optical hyper-parametric oscillator," Nat. Photonics **4**, 41–45 (2010).

71. Y. Okawachi, K. Saha, J. S. Levy, Y. H. Wen, M. Lipson, and A. L. Gaeta, "Octave-spanning frequency comb generation in a silicon nitride chip," Opt. Lett. **36**, 3398 (2011).

72. T. J. Kippenberg, R. Holzwarth, and S. A. Diddams, "Microresonator-Based Optical Frequency Combs," Science **332**, 555–559 (2011).

73. M. A. Foster, J. S. Levy, O. Kuzucu, K. Saha, M. Lipson, and A. L. Gaeta, "Silicon-based monolithic optical frequency comb source," Opt. Express **19**, 14233–14239 (2011).

74. M. Peccianti, A. Pasquazi, Y. Park, B. E. Little, S. T. Chu, D. J. Moss, and R. Morandotti, "Ultrafast modelocked nonlinear micro-cavity laser," Nat. Commun. **3**, 765 (2012).

75. P.-H. Wang, F. Ferdous, H. Miao, J. Wang, D. E. Leaird, K. Srinivasan, L. Chen, V. Aksyuk, and A. M. Weiner, "Observation of correlation between route to formation, coherence, noise, and communication performance of Kerr combs," Opt. Express **20**, 29284–29295 (2012).

76. T. Herr, V. Brasch, J. D. Jost, C. Y. Wang, N. M. Kondratiev, M. L. Gorodetsky, and T. J. Kippenberg, "Temporal solitons in optical microresonators," Nat. Photonics **8**, 145–152 (2014).

77. K. Saha, Y. Okawachi, B. Shim, J. S. Levy, R. Salem, A. R. Johnson, M. A. Foster, M. R. E. Lamont, M. Lipson, and A. L. Gaeta, "Modelocking and femtosecond pulse generation in chip-based frequency combs," Opt. Express **21**, 1335 (2013).

78. D. J. Moss, R. Morandotti, A. L. Gaeta, and M. Lipson, "New CMOS-compatible platforms based on silicon nitride and Hydex for nonlinear optics," Nat. Photonics **7**, 597–607 (2013).

79. J. Riemensberger, K. Hartinger, T. Herr, V. Brasch, R. Holzwarth, and T. J. Kippenberg, "Dispersion engineering of thick high-Q silicon nitride ring-resonators via atomic layer deposition," Opt. Express **20**, 27661 (2012).

80. V. S. Ilchenko, A. A. Savchenkov, A. B. Matsko, and L. Maleki, "Dispersion compensation in whispering-gallery modes," JOSA A **20**, 157–162 (2003).

81. C. J. Chen, C. A. Husko, I. Meric, K. L. Shepard, C. W. Wong, W. M. J. Green, Y. A. Vlasov, and S. Assefa, "Deterministic tuning of slow-light in photonic-crystal waveguides through the C and L bands by atomic layer deposition," Appl. Phys. Lett. **96**, 081107 (2010).

82. L. Zhang, C. Bao, V. Singh, J. Mu, C. Yang, A. M. Agarwal, L. C. Kimerling, and J. Michel, "Generation of two-cycle pulses and octave-spanning frequency combs in a dispersion-flattened micro-resonator," Opt. Lett. **38**, 5122–5125 (2013).

83. A. B. Matsko, A. A. Savchenkov, and L. Maleki, "Normal group-velocity dispersion Kerr frequency comb," Opt. Lett. **37**, 43–45 (2012).

84. T. Hansson, D. Modotto, and S. Wabnitz, "Dynamics of the modulational instability in microresonator frequency combs," Phys. Rev. A **88**, 023819 (2013).

85. C. Godey, I. V. Balakireva, A. Coillet, and Y. K. Chembo, "Stability analysis of the spatiotemporal Lugiato-Lefever model for Kerr optical frequency combs in the anomalous and normal dispersion regimes," Phys. Rev. A **89**, 063814 (2014).

86. A. Coillet, I. Balakireva, R. Henriet, K. Saleh, L. Larger, J. M. Dudley, C. R. Menyuk, and Y. K. Chembo, "Azimuthal Turing Patterns, Bright and Dark Cavity Solitons in Kerr Combs Generated With Whispering-Gallery-Mode Resonators," IEEE Photonics J. **5**, 6100409–6100409 (2013).

87. I. S. Grudinin, L. Baumgartel, and N. Yu, "Impact of cavity spectrum on span in microresonator frequency combs," Opt. Express **21**, 26929–26935 (2013).

88. S. L. Gilbert, W. C. Swann, and C. M. Wang, "Hydrogen cyanide H13C14N absorption reference for 1530–1560 nm wavelength calibration – SRM 2519," Natl. Inst. Stnd. Technol. Spec. Publ. **260**, 137 (1998).

89. P. Del'Haye, O. Arcizet, M. L. Gorodetsky, R. Holzwarth, and T. J. Kippenberg, "Frequency comb assisted diode laser spectroscopy for measurement of microcavity dispersion," Nat. Photonics **3**, 529–533 (2009).

90. A. Arbabi and L. L. Goddard, "Measurements of the refractive indices and thermo-optic coefficients of Si3N4 and SiOx using microring resonances," Opt. Lett. **38**, 3878–3881 (2013).

91. C.-L. Tien and T.-W. Lin, "Thermal expansion coefficient and thermomechanical properties of SiNx thin films prepared by plasma-enhanced chemical vapor deposition," Appl. Opt. **51**, 7229–7235 (2012).

92. A. A. Savchenkov, A. B. Matsko, W. Liang, V. S. Ilchenko, D. Seidel, and L. Maleki, "Kerr frequency comb generation in overmoded resonators," Opt. Express **20**, 27290–27298 (2012).

93. T. Herr, V. Brasch, J. D. Jost, I. Mirgorodskiy, G. Lihachev, M. L. Gorodetsky, and T. J. Kippenberg, "Mode spectrum and temporal soliton formation in optical microresonators," (2013).

94. R. Germann, H. W. M. Salemink, R. Beyeler, G. L. Bona, F. Horst, I. Massarek, and B. J. Offrein, "Silicon Oxynitride Layers for Optical Waveguide Applications," J. Electrochem. Soc. **147**, 2237–2241 (2000).

95. C. Y. Wang, T. Herr, P. Del'Haye, A. Schliesser, J. Hofer, R. Holzwarth, T. W. Hänsch, N. Picqué, and T. J. Kippenberg, "Mid-infrared optical frequency combs at 2.5 μm based on crystalline microresonators," Nat. Commun. **4**, 1345 (2013).

96. A. B. Matsko, W. Liang, A. A. Savchenkov, and L. Maleki, "Chaotic dynamics of frequency combs generated with continuously pumped nonlinear microresonators," Opt. Lett. **38**, 525–527 (2013).

97. F. C. Cruz, J. D. Marconi, A. Cerqueira S. Jr., and H. L. Fragnito, "Broadband second harmonic generation of an optical frequency comb produced by four-wave mixing in highly nonlinear fibers," Opt. Commun. **283**, 1459–1462 (2010).

98. L. E. Nelson, S. B. Fleischer, G. Lenz, and E. P. Ippen, "Efficient frequency doubling of a femtosecond fiber laser," Opt. Lett. **21**, 1759–1761 (1996).

99. R. Trebino, *Frequency-Resolved Optical Gating: The Measurement of Ultrashort Laser Pulses* (Springer Science & Business Media, 2012).

100. C. A. Husko, S. Combrié, P. Colman, J. Zheng, A. D. Rossi, and C. W. Wong, "Soliton dynamics in the multiphoton plasma regime," Sci. Rep. **3**, 1100 (2013).

101. L. E. Nelson, S. B. Fleischer, G. Lenz, and E. P. Ippen, "Efficient frequency doubling of a femtosecond fiber laser," Opt. Lett. **21**, 1759–1761 (1996).

102. J. W. Nicholson, F. G. Omenetto, D. J. Funk, and A. J. Taylor, "Evolving FROGS: phase retrieval from frequency-resolved optical gating measurements by use of genetic algorithms," Opt. Lett. **24**, 490–492 (1999).

103. D. E. Goldberg and J. H. Holland, "Genetic Algorithms and Machine Learning," Mach. Learn. **3**, 95–99 (1988).

104. G. Stibenz and G. Steinmeyer, "Interferometric frequency-resolved optical gating," Opt. Express **13**, 2617–2626 (2005).

105. J. K. Jang, M. Erkintalo, S. G. Murdoch, and S. Coen, "Ultraweak long-range interactions of solitons observed over astronomical distances," Nat. Photonics **7**, 657 (2013).

106. M. Rhodes, G. Steinmeyer, J. Ratner, and R. Trebino, "Pulse-shape instabilities and their measurement," Laser Photonics Rev. **7**, 557–565 (2013).

107. A. A. Savchenkov, W. Liang, A. B. Matsko, V. S. Ilchenko, D. Seidel, and L. Maleki, "Narrowband tunable photonic notch filter," Opt. Lett. **34**, 1318–1320 (2009).

108. X. Xue, Y. Xuan, Y. Liu, P.-H. Wang, S. Chen, J. Wang, D. E. Leaird, M. Qi, and A. M. Weiner, "Mode-locked dark pulse Kerr combs in normal-dispersion microresonators," Nat. Photonics **9**, 594–600 (2015).

109. A. Chong, W. H. Renninger, and F. W. Wise, "Properties of normal-dispersion femtosecond fiber lasers," JOSA B **25**, 140–148 (2008).

110. H. A. Haus, J. G. Fujimoto, and E. P. Ippen, "Structures for additive pulse mode locking," JOSA B **8**, 2068–2076 (1991).

111. P. Del'Haye, K. Beha, S. B. Papp, and S. A. Diddams, "Self-Injection Locking and Phase-Locked States in Microresonator-Based Optical Frequency Combs," Phys. Rev. Lett. **112**, 043905 (2014).

112. A. Hasegawa, "Soliton-based optical communications: an overview," IEEE J. Sel. Top. Quantum Electron. **6**, 1161–1172 (2000).

113. P. Del'Haye, K. Beha, S. B. Papp, and S. A. Diddams, "Self-Injection Locking and Phase-Locked States in Microresonator-Based Optical Frequency Combs," Phys. Rev. Lett. **112**, 043905 (2014).

114. P. Del'Haye, "Optical Frequency Comb Generation in Monolithic Microresonators," Text.PhDThesis, Ludwig-Maximilians-Universität München (2011).

115. T. Herr, K. Hartinger, J. Riemensberger, C. Y. Wang, E. Gavartin, R. Holzwarth, M. L. Gorodetsky, and T. J. Kippenberg, "Universal formation dynamics and noise of Kerr-frequency combs in microresonators," Nat. Photonics **6**, 480–487 (2012).

116. L. Zhang, C. Bao, V. Singh, J. Mu, C. Yang, A. M. Agarwal, L. C. Kimerling, and J. Michel, "Generation of two-cycle pulses and octave-spanning frequency combs in a dispersion-flattened micro-resonator," Opt. Lett. **38**, 5122–5125 (2013).

117. I. S. Grudinin, L. Baumgartel, and N. Yu, "Impact of cavity spectrum on span in microresonator frequency combs," Opt. Express **21**, 26929–26935 (2013).

118. Y. Liu, Y. Xuan, X. Xue, P.-H. Wang, S. Chen, A. J. Metcalf, J. Wang, D. E. Leaird, M. Qi, and A. M. Weiner, "Investigation of mode coupling in normal-dispersion silicon nitride microresonators for Kerr frequency comb generation," Optica **1**, 137–144 (2014).

119. C. Y. Wang, T. Herr, P. Del'Haye, A. Schliesser, J. Hofer, R. Holzwarth, T. W. Hänsch, N. Picqué, and T. J. Kippenberg, "Mid-infrared optical frequency combs at 2.5 μm based on crystalline microresonators," Nat. Commun. **4**, 1345 (2013).

120. T. Herr, V. Brasch, J. D. Jost, C. Y. Wang, N. M. Kondratiev, M. L. Gorodetsky, and T. J. Kippenberg, "Temporal solitons in optical microresonators," Nat. Photonics **8**, 145–152 (2014).

121. T. Herr, V. Brasch, J. D. Jost, I. Mirgorodskiy, G. Lihachev, M. L. Gorodetsky, and T. J. Kippenberg, "Mode Spectrum and Temporal Soliton Formation in Optical Microresonators," Phys. Rev. Lett. **113**, 123901 (2014).

122. T. Ideguchi, S. Holzner, B. Bernhardt, G. Guelachvili, N. Picqué, and T. W. Hänsch, "Coherent Raman spectro-imaging with laser frequency combs," Nature **502**, 355–358 (2013).

123. D. Hillerkuss, R. Schmogrow, T. Schellinger, M. Jordan, M. Winter, G. Huber, T. Vallaitis, R. Bonk, P. Kleinow, F. Frey, M. Roeger, S. Koenig, A. Ludwig, A. Marculescu, J. Li, M. Hoh, M. Dreschmann, J. Meyer, S. B. Ezra, N. Narkiss, B. Nebendahl, F. Parmigiani, P. Petropoulos, B. Resan, A. Oehler, K. Weingarten, T. Ellermeyer, J. Lutz, M. Moeller, M. Huebner, J. Becker, C. Koos, W. Freude, and J. Leuthold, "26 Tbit s-1 line-rate super-channel transmission utilizing all-optical fast Fourier transform processing," Nat. Photonics **5**, 364–371 (2011).

124. S. T. Cundiff and A. M. Weiner, "Optical arbitrary waveform generation," Nat. Photonics **4**, 760 (2010).

125. A. G. Glenday, C.-H. Li, N. Langellier, G. Chang, L.-J. Chen, G. Furesz, A. A. Zibrov, F. Kärtner, D. F. Phillips, D. Sasselov, A. Szentgyorgyi, and R. L. Walsworth, "Operation of a broadband visible-wavelength astro-comb with a high-resolution astrophysical spectrograph," Optica **2**, 250–254 (2015).

126. S. B. Papp, P. Del?Haye, and S. A. Diddams, "Parametric seeding of a microresonator optical frequency comb," Opt. Express **21**, 17615–17624 (2013).

127. P. Del'Haye, K. Beha, S. B. Papp, and S. A. Diddams, "Self-Injection Locking and Phase-Locked States in Microresonator-Based Optical Frequency Combs," Phys. Rev. Lett. **112**, 043905 (2014).

128. A. B. Matsko and L. Maleki, "On timing jitter of mode locked Kerr frequency combs," Opt. Express **21**, 28862–28876 (2013).

129. A. A. Savchenkov, D. Eliyahu, W. Liang, V. S. Ilchenko, J. Byrd, A. B. Matsko, D. Seidel, and L. Maleki, "Stabilization of a Kerr frequency comb oscillator," Opt. Lett. **38**, 2636–2639 (2013).

130. A. Bruner, V. Mahal, I. Kiryuschev, A. Arie, M. A. Arbore, and M. M. Fejer, "Frequency stability at the kilohertz level of a rubidium-locked diode laser at 192.114 THz," Appl. Opt. **37**, 6410–6414 (1998).

131. S. B. Papp, K. Beha, P. Del'Haye, F. Quinlan, H. Lee, K. J. Vahala, and S. A. Diddams, "Microresonator frequency comb optical clock," Optica **1**, 10–14 (2014).

132. E. Rubiola, F. Vernotte, and V. Giordano, "On the measurement of frequency and of its sample variance with high-resolution counters," in *Proceedings of the 2005 IEEE International Frequency Control Symposium and Exposition, 2005.* (2005), p. 4 pp.-.

133. A. M. Turing, "The Chemical Basis of Morphogenesis," Philos. Trans. R. Soc. Lond. B Biol. Sci. **237**, 37–72 (1952).

134. S. Kondo and T. Miura, "Reaction-Diffusion Model as a Framework for Understanding Biological Pattern Formation," Science **329**, 1616–1620 (2010).

135. A. W. Liehr, *Dissipative Solitons in Reaction Diffusion Systems*, Springer Series in Synergetics (Springer Berlin Heidelberg, 2013), Vol. 70.

136. A. J. Scroggie, W. J. Firth, G. S. McDonald, M. Tlidi, R. Lefever, and L. A. Lugiato, "Pattern formation in a passive Kerr cavity," Chaos Solitons Fractals **4**, 1323–1354 (1994).

137. L. A. Lugiato and R. Lefever, "Spatial Dissipative Structures in Passive Optical Systems," Phys. Rev. Lett. **58**, 2209–2211 (1987).

138. A. Coillet and Y. K. Chembo, "Routes to spatiotemporal chaos in Kerr optical frequency combs," Chaos Interdiscip. J. Nonlinear Sci. **24**, 013113 (2014).

139. X. Yi, Q.-F. Yang, K. Y. Yang, M.-G. Suh, and K. Vahala, "Soliton frequency comb at microwave rates in a high-Q silica microresonator," Optica **2**, 1078–1085 (2015).

140. C. Joshi, J. K. Jang, K. Luke, X. Ji, S. A. Miller, A. Klenner, Y. Okawachi, M. Lipson, and A. L. Gaeta, "Thermally controlled comb generation and soliton modelocking in microresonators," Opt. Lett. **41**, 2565–2568 (2016).

141. S.-W. Huang, J. Yang, M. Yu, B. H. McGuyer, D.-L. Kwong, T. Zelevinsky, and C. W. Wong, "A broadband chip-scale optical frequency synthesizer at 2.7 × 10−16 relative uncertainty," Sci. Adv. **2**, e1501489 (2016).

142. P. Del'Haye, A. Coillet, T. Fortier, K. Beha, D. C. Cole, K. Y. Yang, H. Lee, K. J. Vahala, S. B. Papp, and S. A. Diddams, "Phase-coherent microwave-to-optical link with a self-referenced microcomb," Nat. Photonics **10**, 516–520 (2016).

143. J. Pfeifle, A. Coillet, R. Henriet, K. Saleh, P. Schindler, C. Weimann, W. Freude, I. V. Balakireva, L. Larger, C. Koos, and Y. K. Chembo, "Optimally Coherent Kerr Combs Generated with Crystalline Whispering Gallery Mode Resonators for Ultrahigh Capacity Fiber Communications," Phys. Rev. Lett. **114**, 093902 (2015).

144. S. A. Miller, Y. Okawachi, S. Ramelow, K. Luke, A. Dutt, A. Farsi, A. L. Gaeta, and M. Lipson, "Tunable frequency combs based on dual microring resonators," Opt. Express **23**, 21527–21540 (2015).

145. X. Xue, Y. Xuan, P.-H. Wang, Y. Liu, D. E. Leaird, M. Qi, and A. M. Weiner, "Normal-dispersion microcombs enabled by controllable mode interactions," Laser Photonics Rev. **9**, L23–L28 (2015).

146. K. Unterrainer, A. Benz, J. Darmo, C. Deutsch, G. Fasching, J. Kroll, D. P. Kelly, M. Martl, T. MÜller, W. Parz, S. S. Dhillon, C. Sirtori, A. M. Andrews, W. Schrenk, G. Strasser, X. Marcadet, M. Calligaro, H. E. Beere, and D. A. Ritchie, "Terahertz Quantum Cascade Devices: From Intersubband Transition to Microcavity Laser," IEEE J. Sel. Top. Quantum Electron. **14**, 307–314 (2008).

147. S. Jung, A. Jiang, Y. Jiang, K. Vijayraghavan, X. Wang, M. Troccoli, and M. A. Belkin, "Broadly tunable monolithic room-temperature terahertz quantum cascade laser sources," Nat. Commun. **5**, 4267 (2014).

148. C. Sirtori, S. Barbieri, and R. Colombelli, "Wave engineering with THz quantum cascade lasers," Nat. Photonics **7**, 691–701 (2013).

149. J. Darmo, V. Tamosiunas, G. Fasching, J. Kröll, K. Unterrainer, M. Beck, M. Giovannini, J. Faist, C. Kremser, and P. Debbage, "Imaging with a Terahertz quantum cascade laser," Opt. Express **12**, 1879–1884 (2004).

150. S. Koenig, D. Lopez-Diaz, J. Antes, F. Boes, R. Henneberger, A. Leuther, A. Tessmann, R. Schmogrow, D. Hillerkuss, R. Palmer, T. Zwick, C. Koos, W. Freude, O. Ambacher, J. Leuthold, and I. Kallfass, "Wireless sub-THz communication system with high data rate," Nat. Photonics **7**, 977–981 (2013).

151. Y. Yoshimizu, S. Hisatake, S. Kuwano, J. Terada, N. Yoshimoto, and T. Nagatsuma, "Wireless Transmission using Coherent Terahertz Wave with Phase Stabilization," IEICE Electron. Express **advpub**, (2013).

152. A. Rueda, F. Sedlmeir, M. C. Collodo, U. Vogl, B. Stiller, G. Schunk, D. V. Strekalov, C. Marquardt, J. M. Fink, O. Painter, G. Leuchs, and H. G. L. Schwefel, "Efficient microwave to optical photon conversion: an electro-optical realization," Optica **3**, 597–604 (2016).

153. L. Zhang, Y. Yue, R. G. Beausoleil, and A. E. Willner, "Analysis and engineering of chromatic dispersion in silicon waveguide bends and ring resonators," Opt. Express **19**, 8102–8107 (2011).

154. A. Arbabi and L. L. Goddard, "Measurements of the refractive indices and thermo-optic coefficients of Si_3N_4 and SiO_x using microring resonances," Opt. Lett. **38**, 3878–3881 (2013).

155. S. Fujii, A. Hori, T. Kato, R. Suzuki, Y. Okabe, W. Yoshiki, A.-C. Jinnai, and T. Tanabe, "Effect on Kerr comb generation in a clockwise and counter-clockwise mode coupled microcavity," Opt. Express **25**, 28969–28982 (2017).

156. T. Nagatsuma, G. Ducournau, and C. C. Renaud, "Advances in terahertz communications accelerated by photonics," Nat. Photonics **10**, 371–379 (2016).

157. Q. Quraishi, M. Griebel, T. Kleine-Ostmann, and R. Bratschitsch, "Generation of phase-locked and tunable continuous-wave radiation in the terahertz regime," Opt. Lett. **30**, 3231–3233 (2005).

158. J. F. Cliche, B. Shillue, M. Tetu, and M. Poulin, "A 100-GHz-tunable photonic millimeter wave synthesizer for the Atacama Large Millimeter Array radiotelescope," in *2007 IEEE/MTT-S International Microwave Symposium* (2007), pp. 349–352.

159. H.-J. Song, N. Shimizu, and T. Nagatsuma, "Generation of two-mode optical signals with broadband frequency tunability and low spurious signal level," Opt. Express **15**, 14901–14906 (2007).

160. A. Rolland, G. Loas, M. Brunel, L. Frein, M. Vallet, and M. Alouini, "Non-linear optoelectronic phase-locked loop for stabilization of opto-millimeter waves: towards a narrow linewidth tunable THz source," Opt. Express **19**, 17944–17950 (2011).

161. G. Pillet, L. Morvan, M. Brunel, F. Bretenaker, D. Dolfi, M. Vallet, J. P. Huignard, and A. L. Floch, "Dual-Frequency Laser at 1.5 m for Optical Distribution and Generation of High-Purity Microwave Signals," J. Light. Technol. **26**, 2764–2773 (2008).

162. G. Danion, C. Hamel, L. Frein, F. Bondu, G. Loas, and M. Alouini, "Dual frequency laser with two continuously and widely tunable frequencies for optical referencing of GHz to THz beatnotes," Opt. Express **22**, 17673–17678 (2014).

163. H. Shao, S. Keyvaninia, M. Vanwolleghem, G. Ducournau, X. Jiang, G. Morthier, J.-F. Lampin, and G. Roelkens, "Heterogeneously integrated III–V/silicon dual-mode distributed feedback laser array for terahertz generation," Opt. Lett. **39**, 6403–6406 (2014).

164. C. W. Berry, M. R. Hashemi, S. Preu, H. Lu, A. C. Gossard, and M. Jarrahi, "High power terahertz generation using 1550 nm plasmonic photomixers," Appl. Phys. Lett. **105**, 011121 (2014).

165. H. Tanoto, J. H. Teng, Q. Y. Wu, M. Sun, Z. N. Chen, S. A. Maier, B. Wang, C. C. Chum, G. Y. Si, A. J. Danner, and S. J. Chua, "Nano-antenna in a photoconductive photomixer for highly efficient continuous wave terahertz emission," Sci. Rep. **3**, srep02824 (2013).

166. G. P. Agrawal, *Nonlinear Fiber Optics* (Academic Press, 2013).

167. V. Brasch, M. Geiselmann, T. Herr, G. Lihachev, M. H. P. Pfeiffer, M. L. Gorodetsky, and T. J. Kippenberg, "Photonic chip–based optical frequency comb using soliton Cherenkov radiation," Science **351**, 357–360 (2016).

168. V. Brasch, E. Lucas, J. D. Jost, M. Geiselmann, and T. J. Kippenberg, "Self-referenced photonic chip soliton Kerr frequency comb," Light Sci. Appl. **6**, e16202 (2017).

169. A. M. Weiner, "Frequency combs: Cavity solitons come of age," Nat. Photonics **11**, 533 (2017).

170. S. B. Papp, K. Beha, P. Del'Haye, F. Quinlan, H. Lee, K. J. Vahala, and S. A. Diddams, "Microresonator frequency comb optical clock," Optica **1**, 10 (2014).

171. J. Pfeifle, V. Brasch, M. Lauermann, Y. Yu, D. Wegner, T. Herr, K. Hartinger, P. Schindler, J. Li, D. Hillerkuss, R. Schmogrow, C. Weimann, R. Holzwarth, W. Freude, J. Leuthold, T. J. Kippenberg, and C. Koos, "Coherent terabit communications with microresonator Kerr frequency combs," Nat. Photonics **8**, 375–380 (2014).

172. C. Reimer, M. Kues, P. Roztocki, B. Wetzel, F. Grazioso, B. E. Little, S. T. Chu, T. Johnston, Y. Bromberg, L. Caspani, D. J. Moss, and R. Morandotti, "Generation of multiphoton entangled quantum states by means of integrated frequency combs," Science **351**, 1176–1180 (2016).

173. M.-G. Suh, Q.-F. Yang, K. Y. Yang, X. Yi, and K. J. Vahala, "Microresonator soliton dual-comb spectroscopy," Science aah6516 (2016).

174. Z. Xie, T. Zhong, S. Shrestha, X. Xu, J. Liang, Y.-X. Gong, J. C. Bienfang, A. Restelli, J. H. Shapiro, F. N. C. Wong, and C. Wei Wong, "Harnessing high-dimensional hyperentanglement through a biphoton frequency comb," Nat. Photonics **9**, 536–542 (2015).

175. J. A. Jaramillo-Villegas, P. Imany, O. D. Odele, D. E. Leaird, Z.-Y. Ou, M. Qi, and A. M. Weiner, "Persistent energy–time entanglement covering multiple resonances of an on-chip biphoton frequency comb," Optica **4**, 655–658 (2017).

176. P. Del'Haye, T. Herr, E. Gavartin, M. L. Gorodetsky, R. Holzwarth, and T. J. Kippenberg, "Octave Spanning Tunable Frequency Comb from a Microresonator," Phys. Rev. Lett. **107**, 063901 (2011).

177. J. Wang, Y. Guo, H. Liu, G. Li, and L. Zhang, "A Comparative Analysis on Fully Integrated Spectral Broadening of Kerr Frequency Combs," IEEE Photonics J. **9**, 1–9 (2017).

178. D. T. Spencer, T. Drake, T. C. Briles, J. Stone, L. C. Sinclair, C. Fredrick, Q. Li, D. Westly, B. R. Ilic, A. Bluestone, N. Volet, T. Komljenovic, L. Chang, S. H. Lee, D. Y. Oh, M.-G. Suh, K. Y. Yang, M. H. P. Pfeiffer, T. J. Kippenberg, E. Norberg, L. Theogarajan, K. Vahala, N. R. Newbury, K. Srinivasan, J. E. Bowers, S. A. Diddams, and S. B. Papp, "An Integrated-Photonics Optical-Frequency Synthesizer," ArXiv170805228 Phys. (2017).

179. C. Bao, H. Taheri, L. Zhang, A. Matsko, Y. Yan, P. Liao, L. Maleki, and A. E. Willner, "High-order dispersion in Kerr comb oscillators," JOSA B **34**, 715–725 (2017).

180. Q. Li, T. C. Briles, D. A. Westly, T. E. Drake, J. R. Stone, B. R. Ilic, S. A. Diddams, S. B. Papp, and K. Srinivasan, "Stably accessing octave-spanning microresonator frequency combs in the soliton regime," Optica **4**, 193–203 (2017).

181. Y. K. Chembo, D. V. Strekalov, and N. Yu, "Spectrum and Dynamics of Optical Frequency Combs Generated with Monolithic Whispering Gallery Mode Resonators," Phys. Rev. Lett. **104**, 103902 (2010).

182. S. Coen and M. Erkintalo, "Universal scaling laws of Kerr frequency combs," Opt. Lett. **38**, 1790–1792 (2013).

183. S.-W. Huang, G. Cirmi, J. Moses, K.-H. Hong, S. Bhardwaj, J. R. Birge, L.-J. Chen, E. Li, B. J. Eggleton, G. Cerullo, and F. X. Kärtner, "High-energy pulse synthesis with sub-cycle waveform control for strong-field physics," Nat. Photonics **5**, 475 (2011).

184. C. Manzoni, O. D. Mücke, G. Cirmi, S. Fang, J. Moses, S.-W. Huang, K.-H. Hong, G. Cerullo, and F. X. Kärtner, "Coherent pulse synthesis: towards sub-cycle optical waveforms," Laser Photonics Rev. **9**, 129–171 (2015).

185. A. B. Matsko, A. A. Savchenkov, S.-W. Huang, and L. Maleki, "Clustered frequency comb," Opt. Lett. **41**, 5102–5105 (2016).

186. S.-W. Huang, A. K. Vinod, J. Yang, M. Yu, D.-L. Kwong, and C. W. Wong, "Quasi-phase-matched multispectral Kerr frequency comb," Opt. Lett. **42**, 2110–2113 (2017).

187. T. Ideguchi, B. Bernhardt, G. Guelachvili, T. W. Hänsch, and N. Picqué, "Raman-induced Kerr-effect dual-comb spectroscopy," Opt. Lett. **37**, 4498–4500 (2012).

188. I. S. Grudinin and L. Maleki, "Ultralow-threshold Raman lasing with CaF_2 resonators," Opt. Lett. **32**, 166–168 (2007).

189. S. M. Spillane, T. J. Kippenberg, and K. J. Vahala, "Ultralow-threshold Raman laser using a spherical dielectric microcavity," Nature **415**, 621 (2002).

190. T. Okoshi, K. Kikuchi, and A. Nakayama, "Novel method for high resolution measurement of laser output spectrum," Electron. Lett. **16**, 630–631 (1980).